Magnetic Particle Characterization and Quantification of Endocytosis Mechanisms of Cultured Mammalian Cells by Magnetic Cytometry

by

Abhinav Sannidhi

A dissertation submitted to the Graduate Faculty of
Auburn University
in partial fulfillment of the
requirements for the Degree of
Doctor of Philosophy

Auburn, Alabama
December 12, 2020

Keywords: magnetophoretic mobility, magnetic nanoparticles, intrinsic magnetic properties, endocytosis mechanisms, magnetic cytometry, particle tracking velocimetry

Approved by

Thomas Hanley, Chair, Professor of Chemical Engineering
Allan David, Associate Professor of Chemical Engineering
Mario Eden, Professor of Chemical Engineering
Bart Prorok, Professor of Materials Engineering
Paul Todd, Chief Scientist Emeritus at Techshot, Inc.

Abstract

Magnetic characterization and quantification of individual magnetic particles and magnetically labeled cells of the sample is of much importance to assess the sample quality and better application in the fields of drug delivery, cell purification, endocytosis, cell separation, biomedical, pharmaceutical and cell therapeutics. A particle tracking velocimeter is utilized to measure magnetophoretic mobility, size, sedimentation rate, intensity and other morphological parameters of magnetic particles and magnetically labeled cells by magnetic cytometry. Magnetic cytometry by particle tracking velocimetry records the motion of labeled cells in an isodynamic magnetic field thereby estimating the key parameter, magnetophoretic mobility of labeled cells. The calibration capability of the instrument has been extended in order to estimate the actual particle size and thereby estimate the intrinsic magnetic properties of several commercial beads on a particle-by-particle basis. Different methods have been explored to estimate the magnetophoretic mobility of individual nanoparticles using the instrument. The chain velocity method is used to extrapolate mobility of the nanoparticles, which is in agreement with the theory. The receptor-independent uptake by cultured mammalian cells of magnetic nanoparticles with different surface coatings was studied to reveal the role of nanoparticle endocytosis mechanisms by using specific mechanism-based inhibitors, genistein and chlorpromazine hydrochloride. The cellular survival rate/ viability, toxicity and inhibition rate of the mechanism-based inhibitors, genistein and chlorpromazine hydrochloride is quantified by magnetophoretic mobility measurement of thousands of magnetically labeled CHO-K1 cells. Caveolae mediated and clathrin dependent endocytosis mechanisms were dominant for aminated starch and dextran-sulfate coated beads.

Magnetic cytometry analysis reveals that the magnetic nanoparticle surface charge, composition and inhibitor toxicity strongly affect the cellular uptake. The particle-cell system can be optimized using velocimetry by the estimation of intrinsic magnetic properties on a particle-by-particle basis and the determination of roles of different endocytosis mechanisms.

Acknowledgments

I wish to express my sincere gratitude to my advisor Dr. Thomas R. Hanley for the constant motivation, immense support and encouragement, and to Dr. Paul W. Todd for the boundless patience, constructive advice and invaluable guidance that brought my work to a higher level. Your ideas and profound feedback have helped me sharpen my thinking and grow into my potential.

I would like to thank Dr. Allan E. David and his group members, for providing biosafety lab facility to perform labeled cells experimentation. A special thanks to my dissertation committee members Dr. Allan E. David, Dr. Mario R. Eden, Dr. Bart C. Prorok, Dr. Paul W. Todd for their encouragement and visionary comments to improve the quality of my dissertation. I acknowledge Dr. Robert D. Arnold "Rusty" for serving as the University Reader for my dissertation.

I would like to express my thanks to Dr. Michael Miller (AURIF, Biological Sciences) and Dr. Michael Buettner (University of Alabama) for training me to operate the Transmission Electron Microscope and Vibrating Sample Magnetometer respectively. The results yielded by these techniques were vital in my research. I also wish to express my thanks to Elaine Manning, Mullins' family and my friends for making me feel at home in Auburn.

Lastly, I will always be grateful to my family for the selfless support and encouragement from my parents, Ramakrishna Sannidhi and Manjula Sannidhi, my sister, Akhila Sannidhi, my wife, Vyshnavi Bikumalla, my parents-in-law, Venugopala Swamy Bikumalla and Jhansi Laxmi Bai Mukthavaram, and my grandparents, Laxman Rao Sannidhi, Rukmini Sannidhi, late Sri. Sarangapani Sriperumbuduru and Lalitha Sriperumbuduru.

Table of Contents

List of Figures

List of Tables

List of Abbreviations

AFM - Atomic Force Microscopy

CHO - Chinese Hamster Ovary cells

DLS - Dynamic Light Scattering

DMSO - Dimethyl Sulfoxide

DXS - Dextran Sulfate

EC_{50} - Half maximal effective concentration

EDX - Energy Dispersive X-Ray Spectrometer

FACS - Fluorescence Activated Cell Sorters

FBS - Fetal Bovine Serum

FFF - Field-Flow Fractionation

FIB-SEM - Focused Ion Beam Scanning Electron Microscopy

FMR - Ferro-Magnetic Resonance

HBSS - Hanks' Balanced Salt Solution

IC_{50} - Half maximal Inhibitory concentration

ICP-MS - Inductively Coupled Plasma Mass Spectrometry

ICP-OES - Inductively Coupled Plasma- Optical Emission Spectrometry

MERS-CoV - Middle East Respiratory Syndrome-Coronavirus

MNP - Magnetic Nanoparticles

MRI - Magnetic Resonance Imaging

MRX - Magneto-Relaxometry

NMR - Nuclear Magnetic Resonance

PBS - Phosphate Buffered Saline

PPMS - Physical Property Measurement System

SARS-CoV - Severe Acute Respiratory Syndrome-coronavirus

SEM - Scanning Electron Microscope

SPION - Superparamagnetic Iron Oxide Nanoparticles

SQUID - Superconducting Quantum Interface Device

TEM - Transmission Electron Microscopy

VSM - Vibrating Sample Magnetometer

XRD - X-Ray Diffraction

ZP - Zeta Potential

Chapter 1 - Introduction

Magnetic particles are widely used in applications such as ferrofluids, cell purification, labeled cell separation, cell physiology, endocytosis, drug targeting, MRI, hyperthermia, and in vivo diagnostics. These applications require a high-quality magnetic particle sample which possesses specific properties such as uniform particle size, magnetic susceptibility, and saturation magnetization distributions.

Most producers provide only bulk average properties of the magnetic particles which are insufficient for quality assessment. Characterization of magnetic particles plays a key role in magnetic particle production and analysis. The Hyperflux™ velocimeter was used to characterize properties of magnetic particles such as magnetophoretic mobility, particle size, and other parameters. This instrument captures dark-field images of the particle trajectories in an isodynamic field and converts image data into parameters of interest by the image analysis software. The optimum threshold settings and size gating of the instrument, the characterization of magnetic particles and labeled cells, the quantification of nanoparticle phagocytosis, and an investigation of cellular uptake kinetics were accomplished by Zhou et al. 2017, by determining the magnetophoretic mobility using the velocimeter.

An objective of this research is to extend the size calibration capability of the velocimeter instrument and to estimate intrinsic magnetic properties of magnetic particles. The two-parameter distributions between diameter vs apparent magnetic susceptibility and saturation magnetization of different commercial magnetic bead samples are determined for better assessment of particle quality.

The estimation of magnetophoretic mobility of individual superparamagnetic nanoparticles is not feasible using dark-field microscopy but is achieved by exploring six different approaches for the estimation of mobility of single nanoparticles; that includes extrapolation of magnetophoretic mobility of individual nanoparticles from the mobility of detectable magnetic nanoparticle chains.

This work focuses on the study of endocytosis mechanisms of different surface-functionalized magnetic nanobeads using particle tracking velocimetry with the help of mechanism-based chemical inhibitors. The magnetophoretic mobility of labeled cells is measured to investigate the effect of inhibitors of two particle-uptake mechanisms by quantifying the cellular uptake, inhibition rate and inhibitor toxicity so as to infer how nanomaterials enter cells. This work provides a convenient and robust method to describe particle-cell interactions and quantify nanoparticle endocytosis mechanisms using magnetic cytometry.

Chapter 2 - Literature Review

2.1 Introduction

2.1.1 Magnetic Particles

Magnetic particles widely varying in composition, size and magnetization possess unique properties such as superparamagnetism, biocompatibility, monodispersity and stability (Chertok et al., 2008; J.-E. Kim et al., 2012; Lu et al., 2007; Moise et al., 2017; Pankhurst et al., 2003; Reiss & Hütten, 2016). These properties contribute to a wide variety of applications in different fields such as biochemical separations, cell purification, cell labeling, cell physiology, endocytosis, endosome research, drug targeting, analytical biochemistry, environmental analysis, magnetic resonance imaging, hyperthermia and in vivo diagnostics.

Magnetic particles are significant due to their reaction to the applied magnetic field based on their magnetization and the type of magnetic particle (Ito et al., 2005). Ferromagnetic particles are unstable and become paramagnetic and superparamagnetic particles when the particle size is reduced below critical size because of surface energy. Magnetic nanoparticles have a size range of 0.5 nm to 1000 nm. Superparamagnetic Iron Oxide Nanoparticles (SPIONs) are valuable in the fields of biotechnology and medicine as they exhibit nontoxicity (Ito et al., 2005), behave as a single magnetic domain having a constant magnetic moment and have negligible (very low) agglomerate formation (Lu et al., 2007).

Different types of magnetic particles are being used, which include metallic particles, ferrite particles and Iron nitride particles. The development of metallic oxide/ferrite nanoparticles in 1960's, consisting of γ- Fe_2O_3, Fe_3O_4 and MFe_2O_4 (where M= Co, Ni, Mn) particles attained utmost attention by the researchers (Fredrick, 1960; Wickham et al., 1967). The preparation of

Fe_4N magnetic particles in 1993(Tang et al., 1993), lead to the discovery of other iron nitride magnetic particles FeN, Fe_2N, Fe_3N, $Fe_{16}N_2$ (Jönsson et al., 2004; Masubuchi et al., 2011). The hybrid core-shell structure for the magnetic particles protect the core magnetic structure, stabilize and brings in new properties to the system (Deng et al., 2003; Jaeyun Kim et al., 2008; Meng et al., 2018; Sood et al., 2017; Z. Xu et al., 2007).

Magnetization in metallic magnetic nanoparticles is higher than the metal oxides MNPs. But due to their high reactivity and toxicity, metal MNPs need a layer or shell of stabilization around them (Lu et al., 2007). Superparamagnetic nanoparticles are usually stabilized with hydrophobic compounds such as oleic acid, but for biological applications, the particles need to be hydrophilic which is achieved by surface functionalization through surfactant addition or exchange (Frey et al., 2009). Besides surface modifications, matrix dispersed MNPs serve as the easiest way to protect them against oxidation. Other stabilization techniques include coating with silica, carbon, or precious metals such as gold (Au), surfactant passivation, polymer coating, ligand exchange technique (Lu et al., 2007).

2.1.2 Synthesis Methods of Magnetic Particles

Different synthesis methods of magnetic particles have been followed over the past decades, which mainly comprise co-precipitation, thermal decomposition, micro-emulsions, hydrothermal synthesis (Lu et al., 2007) and metal reduction method (Frey et al., 2009). Among these, co-precipitation is the simple and fast method that requires a reaction temperature ranging from 20ºC to 90ºC where iron oxides are synthesized from aqueous Fe^{+3} salt solutions by the addition of base at ambient or elevated temperature (Katepetch & Rujiravanit, 2011). Thermal decomposition method includes the decomposition of organometallic compounds in high-boiling organic solvents in the presence of surfactants (such as fatty acids, oleic acid) which helps in

stabilization (Frey et al., 2009; Lu et al., 2007). This method is long (reaction time in hours), requires an inert atmosphere and the reaction temperature ranging from 100ºC to 300ºC. Thermal decomposition and sol-gel methods were used by Gong et.al to produce Co-Ni nanoparticles (Jie et al., 2010). Microemulsion technique has been employed since 1982 which is the dispersion of two immiscible liquids by stabilizing microdomain with surfactants (Inouye et al., 1982). The synthesis of gold-coated cobalt/platinum (Au-Co/Pt) nanoparticles is done using microemulsion where the presence of gold nanoparticles (Au NPs) prevented oxidation of MNPs (Carpenter et al., 2000). This method requires a reaction temperature ranging from 20ºC to 50ºC at ambient environments. Thus, droplets formed by this technique act as a nanoreactor for the production of nanoparticles (Lu et al., 2007). Hydrothermal synthesis involves phase transfer separation at liquid (ethanol linoleic acid), solid (metal linoleate) and solution (ethanol-water) interfaces where Fe_3O_4 and Co-Fe_3O_4 nanoparticles are mostly synthesized under hydrothermal conditions. This method requires high pressure and temperature (about 220ºC) whose reaction time is long i.e., from hours to days (Lu et al., 2007). Metal reduction method is also used where metal salts are reduced in the presence of surfactants using reducing agents. Thermal decomposition and metal reduction methods are used together to synthesize alloy FePt nanoparticles (Frey et al., 2009). Reverse micro-emulsion method is also used to synthesize gold-coated magnetic nanoparticles (Au MNPs) (Lu et al., 2007). The other core-shell nanoparticle synthesis methods include co-deposition (Binns et al., 2012), emulsion polymerization (Huang et al., 2008), in-situ polymerization (Zhi et al., 2006), intercalation (H. Zhang et al., 2009), sol-gel method (Chen & He, 2001), self-assembly (Q. Liu & Xu, 1995).

2.1.3 Magnetic Susceptibility & Saturation Magnetization

Magnetic susceptibility (χ) is a dimensionless number, describes the degree to which a material can be magnetized in an external magnetic field. It is the ratio of induced magnetization (M) to the applied magnetic field (H).

$$\chi = \frac{M}{H} \tag{2-1}$$

Diamagnetic materials have negative susceptibility values ($\chi < 0$) as they produce negative magnetization in an applied magnetic field due to the absence of unpaired electrons. Paramagnetic materials have positive susceptibility values ($\chi > 0$) and produce a positive magnetization in an applied magnetic field due to the presence of unpaired electrons.

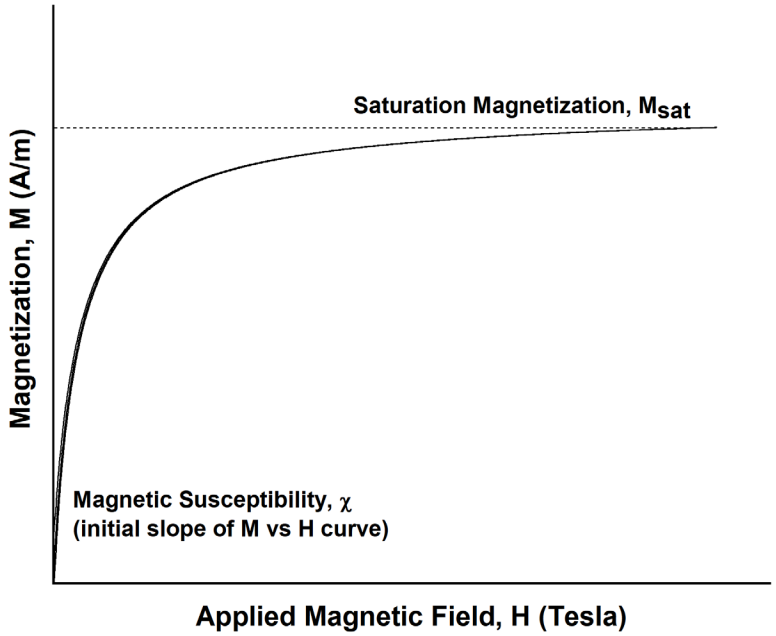

Figure 2.1 - Magnetization (M) vs Applied magnetic field (H) curve.

Saturation Magnetization is the maximum level of an induced magnetic field for a given sample, the induced magnetization (*M*) of the sample reaches the saturation region, beyond which it does not increase with an increase in the applied magnetic field (*H*) (Figure 2.1). Magnetic susceptibility and saturation magnetization are the intrinsic magnetic properties of a given material.

2.1.4 Isodynamic field

Isodynamic field is the area where the magnetic force on the particle is constant and could be generated by two pole pieces (Figure 2.2) where the path lines are parallel and are of same length (Figure 2.3) (Zborowski & Chalmers, 2011). The field-induced particle velocity could be measured as the particle velocity depends only on the particle properties in an isodynamic field.

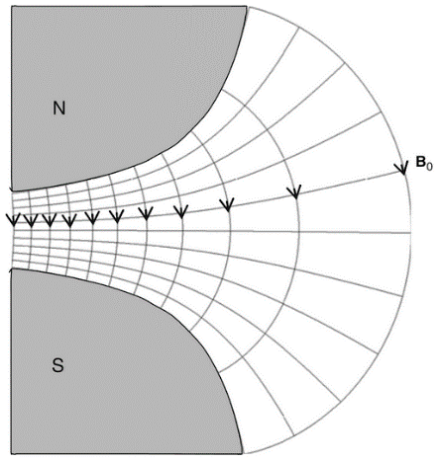

Figure 2.2 - Magnetic field lines between two poles (Zborowski & Chalmers, 2011).

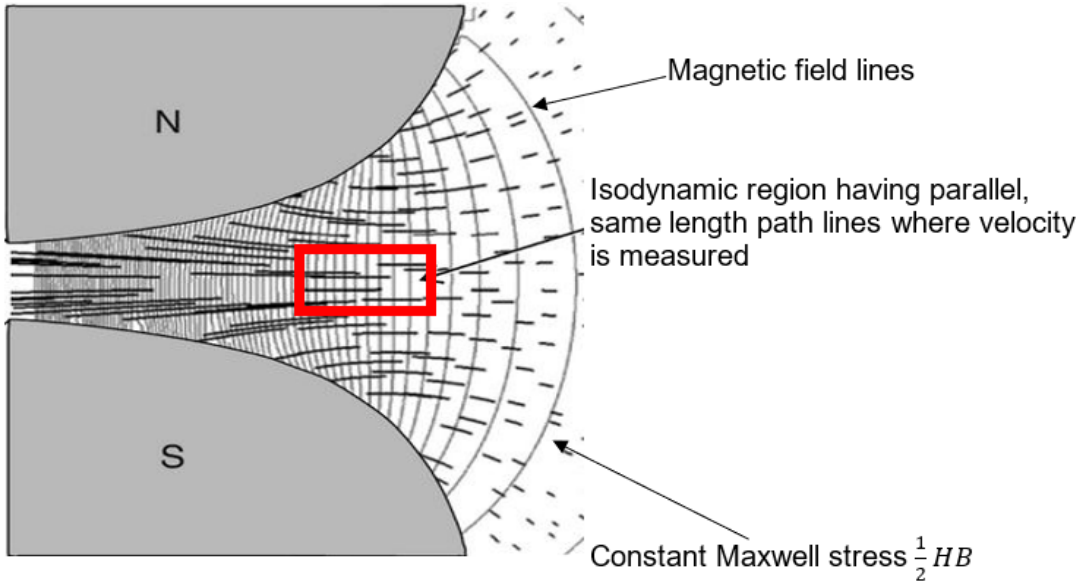

Figure 2.3 - Isodynamic region (in the box) between two pole pieces where the path lines are of same length and almost parallel (Zborowski & Chalmers, 2011).

2.1.5 Magnetophoretic Mobility

Magnetophoretic mobility is an important characteristic of the magnetic particles, which describes the movement of particles in the applied magnetic field.

The magnetic force on a particle (assume as spherical) suspended in a diamagnetic fluid medium with applied magnetic field could be written as (Jones, 1995):

$$F_m = 2\pi\mu_s R^3 \left(\frac{\mu_P - \mu_s}{\mu_p + 2\mu_s}\right) \nabla H_o^2 \qquad (2\text{-}2)$$

Where μ_p and μ_s are permeability of the particle and solution respectively, R is the radius of the particle (spherical) and H_o is field intensity. The permeability can be expressed in terms of susceptibility as follows:

$$\mu = \mu_o(\chi + 1) \qquad (2\text{-}3)$$

The gradient term can also be written as

$$\nabla H_o^2 = \nabla \left(\frac{B_o}{\mu_o}\right)^2 \tag{2-4}$$

The volume of the magnetic particle is given by:

$$V = \frac{4}{3}\pi R^3 \tag{2-5}$$

After combining the above equations 2-2 through 2-5, the magnetic force on a magnetic particle is given by:

$$F_m = 3V(\chi_s + 1)\left(\frac{\chi_p - \chi_s}{\chi_p + 2\chi_s + 3}\right)\nabla\left(\frac{B_o^2}{2\mu_o}\right) \tag{2-6}$$

where χ_p and χ_s are the susceptibility of the particle and solution. By assuming χ_p and χ_s << 1, much smaller than one, the above equation can be simplified as follows:

$$F_m = V(\chi_p - \chi_s)\frac{\nabla B_o^2}{2\mu_o} \tag{2-7}$$

where ∇B_o^2 is the magnetic energy gradient.

Magnetic field produces Maxwell stress in the space. Magnetic force can also be derived from Maxwell stress tensor. In a homogeneous, isotropic, linear medium the stress tensor reduces to a scalar of value $\frac{1}{2}BH$. The divergence of Maxwell stress tensor gives the force density (**f**) in the matter.

$$f = \nabla\left(\frac{1}{2}BH\right) = \nabla\left(\frac{1}{2}\mu_o MH\right) = \nabla\left(\frac{1}{2}B_o M\right) = \nabla\left(\frac{1}{2}\chi B_o H\right) \tag{2-8}$$

$$f = \chi \nabla \left(\frac{1}{2} B_o H\right) \tag{2-9}$$

The magnetic force is given by

$$F_m = fV = V\chi \nabla \left(\frac{1}{2} B_o H\right) \tag{2-10}$$

Here ($B_o = \mu_o H$) and magnetic force could be obtained as

$$F_m = V\chi \frac{\nabla B_o^2}{2\mu_o} \tag{2-11}$$

which is the same as equation 2-7.

Based on Stokes law, the drag force which counteracts the magnetic force could be expressed as:

$$F_d = 6\pi\eta \mathrm{Rv} \tag{2-12}$$

where η is the viscosity of the fluid, R is the radius of the particle and **v** is the terminal velocity of the particle.

Based on the assumption that gravity and buoyancy are negligible, force balance on the magnetic particle can be expressed as

$$F_m - F_d = 0 \tag{2-13}$$

where F_m is the magnetic force and F_d is drag force on the particle.

Thus, the terminal velocity of the particle is obtained as:

$$\vec{v} = \frac{\Delta\chi V}{6\pi\eta R} \nabla \left(\frac{B_o^2}{2\mu_o}\right) \tag{2-14}$$

The above expression is the form of a product of two quantities that are independent of each other. The left term $\frac{\Delta\chi V}{6\pi\eta R}$ designates the properties of the particle and fluid medium; the right term $\nabla\left(\frac{B_o^2}{2\mu_o}\right)$ is the magnetic pressure.

Then magnetophoretic mobility is defined as

$$\mu_m = \frac{\Delta\chi V}{6\pi\eta R} \tag{2-15}$$

also written as

$$\mu_m = \frac{v}{\nabla\left(\frac{B_o^2}{2\mu_o}\right)} \tag{2-16}$$

whose SI units are $\frac{m^3}{T\,A\,s}$ (meter cubed per Tesla-Ampere-second) designating as Rm; (where Rm stands for Rembaum, if we take 1 Rembaum = 1 $\frac{m^3}{T\,A\,s}$, the SI unit of magnetophoretic mobility, honoring the name of Dr. Alan Rembaum who pioneered the quantification of magnetic particles in the 1970s) (Rembaum et al., 1976; Yen et al., 1979, 1980). Usually, magnetophoretic mobilities of magnetic particles are in the range of 10^{-12} (pico) $\frac{m^3}{T\,A\,s}$, therefore expressed as pico Rembaum (pRm).

And magnetic pressure is defined as

$$S_m = \nabla\left(\frac{B_o^2}{2\mu_o}\right) \tag{2-17}$$

In the isodynamic field, S_m is constant. So, the value and direction of **v** are fixed, which implies that the same particles will move in a nearly uniform motion. When the magnetic field is kept constant, the particles with different magnetophoretic mobilities could be separated.

In the equation, $\mu_m = \frac{\Delta\chi V}{6\pi\eta R}$ (by assuming that the particle is spherical, then upon substituting the volume as $V = \frac{4}{3}\pi R^3$) we get

$$\mu_m = \frac{2R^2\Delta\chi}{9\eta} \tag{2-18}$$

The term $\frac{2R^2\Delta\chi}{9\eta}$ magnetophoretic mobility, related to properties (magnetic susceptibility, particle size) of the magnetic particle, is independent of the term $\nabla\left(\frac{B_o^2}{2\mu_o}\right)$, which is a result of the applied magnetic field.

Researchers are focusing more on magnetophoretic mobility studies, as it is the key property of magnetic particles which helps in advancing the fields of cell separation, nanoparticle endocytosis, quantitative and qualitative cell analysis, cell isolation, cell tracking velocimetry etc. (Chalmers et al., 1999; Häfeli et al., 2002; Jin et al., 2008; Kennedy et al., 2007; Jinho Kim et al., 2016; Kirby et al., 2015; McCloskey et al., 2000, 2001, 2003; Reece et al., 2010; Venkata Sunil Kumar Sajja et al., 2011; Suwa & Watarai, 2001; Watarai & Namba, 2002; Wise et al., 2015; Yu et al., 2010; Zhou et al., 2016, 2017, 2018).

2.2 Applications of Magnetic Particles

This section contains significant applications of magnetic particles and the importance of key characteristic-magnetophoretic mobility in these applications.

2.2.1 Magnetic Resonance Imaging (MRI)

Contrast agents in magnetic resonance imaging (MRI) play a vital role in obtaining clear and bright images of the human organs and tissues. This technique is based on proton alignment (either parallel or anti-parallel) with respect to the applied constant high magnetic field and the perpendicular electromagnetic radiofrequency current pulses. Energy is absorbed by the protons when current is applied and it is released when the applied radiofrequency is removed. This process occurs with relaxation times T_1 and T_2 (Haacke et al., 1999; Morris & Slesnick, 2018; Na et al., 2007; Rocklage et al., 1998). Magnetic nanoparticles with their unique properties such as biocompatibility, superparamagnetic property, iron oxide core-shell structure, low toxicity (Wilhelm & Gazeau, 2008) will serve as the better contrast agents when labeled with cells, by reducing the T2 relaxation time of MRI (Cunningham et al., 2005; Jain et al., 2008; Lee & Hyeon, 2012; Yan et al., 2018). Different surface modifications of magnetic nanoparticles such as stabilized coatings, polymer matrix and PEGylation improves cellular uptake and in turn help in creating better contrast agents (Chertok et al., 2008; Cole, David, et al., 2011, 2011; Kania et al., 2018).

Magnetophoretic mobility facilitates the prediction of susceptibility distribution and helps in identifying better contrast agents that are suitable for MRI study. The detection sensitivity of MRI is increased by particles with higher magnetic susceptibility (Schenck, 1996).

2.2.2 Drug Delivery

Magnetic nanoparticles when conjugated or encapsulated with drugs to target specific sites in the body were used to treat different tumors, leukemia and cancer theranostics (Cole, Yang, et al., 2011; El-Boubbou et al., 2017; McBain et al., 2008; Veiseh et al., 2010; Wong et al., 2017). With their high surface to volume ratio, they tend to accumulate at different sites of the human biological system depending on their particle size. So, targeted drug delivery depends on particle size distribution and pharmacokinetics (S.-D. Li & Huang, 2008; Zong et al., 2006). Magnetic nanoparticles need to overcome biological barriers to reach the targeted site (Yadav et al., 2011) where the characteristics, particle size and magnetophoretic mobility plays a key role in selecting the appropriate particles. The chitosan magnetic nanoparticles have high antimicrobial and biological properties (Anirudhan et al., 2014; Assa et al., 2017; Hurst, 2011; Ito et al., 2005; Kania et al., 2018).

Knowledge of magnetophoretic mobility of particles facilitates the better selection process and quantification of particles with dual functionalities such as targeting and imaging (Jing et al., 2008; Yu et al., 2010). The photometric magnetophoretic assay was used in estimating a virus that is bound to the magnetic nanoparticles (Tresilwised et al., 2010).

2.2.3 Cell Labeling and Separation

The target cells labeled with magnetic particles could easily be separated from a group of labeled and unlabeled cells using magnetic field attraction. The field-flow fraction (FFF) technique (J. Calvin Giddings, 1968; J C Giddings, 1993; J Calvin Giddings et al., 1970) which is based on chromatography and field-driven force separates the cells into different thin channels. The split flow thin channel (SPLITT) (J Calvin Giddings, 1985, 1992) technique was also developed, which is a continuous split separation of particles in thin channels. Based on FFF and

SPLITT technologies, Quadrupole FFF was developed (Carpino et al., 2005). The Quadrasep QMS which is a commercially available, continuous, high speed, high throughput cell sorting device was used to successfully separate the labeled islet cells(Venkata Sunil Kumar Sajja et al., 2011; Weegman et al., 2016). The magnetic cell separation technique was applied to the target cells such as rare circulating cancer cells(H. Xu et al., 2011), glial cells(Marek et al., 2008), stem cells (Reece et al., 2010), islet cells (Weegman et al., 2016) that are labeled with magnetic particles.

2.2.4 Magnetic Hyperthermia

Magnetic Hyperthermia is a treatment used to destroy cancer cells using a high-temperature environment induced by magnetic nanoparticles with the help of a magnetic field. The heat localization of the magnetic nanoparticles is very important in this application as it determines the efficiency of this treatment (Hergt et al., 2006, 2008; Thiesen & Jordan, 2008). The Neel relaxation, Brownian relaxation and hysteresis losses are the responsible factors to induce thermal energy. These depend on the size, shape and aggregation of the particles (Deatsch & Evans, 2014). Surface-modified, functionalized and biocompatible SPIONs are widely used in this treatment (Gangopadhyay et al., 2005; Kandasamy et al., 2018). Liver cancer cells were treated using functionalized SPIONs in fluid magnetic hyperthermia treatment (Jordan et al., 1999; Kandasamy et al., 2018).

2.2.5 Magnetic Particle Standard and Quality Control

Microsphere size standards of magnetic particles are maintained by the National Institute of Standards and Technology (NIST). According to NIST traceable size standards, magnetic particles are isolated into 3 size groups: nanobead (40 nm- 950 nm), microbead (1.00 μm- 9.00 μm) and mega bead (10.0 μm- 80.0 μm). These particles are measured using calibrated in-house instruments of NIST. These standard beads are sold explicitly for calibration purposes in various

applications, such as electron microscopy, light scattering, optical imaging and sizing. NIST does not provide any magnetic susceptibility information for the particles. No one to date has reported uniformity and magnetic susceptibility of particles based on their magnetophoretic mobility.

Companies usually report the average size of the magnetic particles they sell but cannot give detailed information like particle size, magnetophoretic mobility and magnetic susceptibility on a particle by particle basis. Estimating magnetophoretic mobility provides a better understanding of particles by quantifying the quality of the particles.

2.3 Magnetic Particle Characterization

Characterization of magnetic particles can be classified into two categories: Structural properties and Magnetic properties.

2.3.1 Structural property characterization

Different methods and devices have previously been recognized to characterize the magnetic structural properties such as particle size determination by Dynamic Light Scattering (DLS) (Jitkang Lim et al., 2013), observation of the particle microstructure by Scanning Electron Microscope (SEM)(Gherca et al., 2012), Transmission Electron Microscope (TEM) (Z. Li et al., 2012), Atomic Force Microscopy (AFM) (Lacava et al., 2000), Magnetic force microscopy (Cordova et al., 2017), determination of the elemental composition and crystalline phase information by X-Ray diffraction (XRD) (Popa et al., 2003; Tadic et al., 2014; Zhao et al., 2000) and energy dispersive X-Ray spectrometer (EDX) (Sun et al., 2000; Tarasov et al., 2008) respectively. The DynoMag AC susceptometer was used to measure structural properties and size distribution of the magnetic particles by measuring relaxation time after exciting the particles using high-frequency alternating current (F. Ludwig et al., 2017).

2.3.1.1 Optical light microscopy

The optical light microscopy includes dark field and bright field illumination. Darkfield microscopy is a technique which generates bright images of the particles on a dark background when the incoming source light is reflected or scattered from the sample wherein bright field microscopy generates dark images of the particles on a bright background when the light is transmitted from the particles (Cerbino, 2018; Hu et al., 2008). ImageJ software was used to analyze the optical images of hybrid plasmonic magnetic nanoparticles to obtain the particle size distribution (Larson et al., 2007). Plasmonic magnetic nanoparticles containing iron oxide core-shell with gold coating were characterized using optical dark field microscopy (JitKang Lim et al., 2007). The modified hyperspectral- dark-field microscopy system (from Cytoviva, Auburn, AL) was used to characterize the nanoparticles in biological media (Zamora-Perez et al., 2018). Janus plasmonic magnetic gold nanoparticles were characterized using optical dark and bright field microscopy(Reguera et al., 2017).

2.3.1.2 ImageJ

ImageJ is an open-source software (based on Java) which serves as an invaluable tool for image processing and analysis. This software is a platform-independent software that runs on different operating systems with the Java run-time environment. Applications of ImageJ include particle analysis, intensity processing and analysis, color-based thresholding, co-localization, fluorescence and staining analysis (Abràmoff et al., 2004; Collins, 2007; Jensen, 2013; Schneider et al., 2012). The size distribution of iron oxide particles was estimated by analyzing TEM images using ImageJ (Jain et al., 2008). In the study of continuous flow bioanalysis of magnetic particles, the average fluorescence intensity of particles, the greyscale intensities of diffusion bands were measured and investigated using this software (Peyman et al., 2009). The mobility of

superparamagnetic particle chains was analyzed using an inverted light microscope, video camera and ImageJ video tracking software (Wise et al., 2015).

2.3.2 Magnetic Property characterization

Magnetic property characterization is crucial in determining the application of magnetic particles in different areas of science. Magnetic particles and paramagnetic particles that can be magnetized in the presence of the external magnetic field possess better characteristics that specify the quality of the sample for a definite application.

Different methods and instruments have been discovered to measure magnetic properties over the past years. Some important instruments are described below.

2.3.2.1 Sherwood Scientific Magnetic Susceptibility Balance

The magnetic susceptibility of magnetic microcrystalline cellulose nanoparticles was measured using Sherwood Scientific magnetic susceptibility balance (Rashid et al., 2017). Several other researchers used this instrument to characterize this property of paramagnetic particles (Anirudhan et al., 2014; Sevgi et al., 2018). The underlying principle of this instrument is a generation of force to compensate and maintain the balance of the system when the magnetic material is placed on the other side of the balance. The force data will be recorded and displayed. Thus, the magnetic susceptibility values will be calculated by the following equation:

$$\chi_g = \frac{C * L * (R - R_o)}{M * 10^9} \tag{2-19}$$

Where C is the calibration constant of the instrument, L is the sample length in cm, R is reading of sample tube, R_o is reading of the empty tube, M is the weight of the sample in grams.

2.3.2.2 Vibrating Sample Magnetometer

This instrument was invented in 1956 by Foner (Foner, 1956, 1959), which is used to measure the magnetic properties of the liquid, powdered, thin films and also bulk samples. The principle of this instrument is recording magnetic flux change and induced voltage while the sample is vibrated in a sinusoidal motion. The hysteresis curves could be generated which contains coercivity, remnant magnetization and saturation magnetization (Filippousi et al., 2013; Kirupakar et al., 2016; Lopez-Dominguez et al., 2018). Applications of VSM include measuring the magnetic properties of anti-cancer drug magnetic microspheres (Kirupakar et al., 2016), substituted Co-Cu-Zn Nano ferrites (Bhukal et al., 2016).

2.3.2.3 Superconducting quantum interference device (SQUID)

A superconducting quantum interference device (Clarke, 1994) is a sensitive magnetometer which is used to measure very low magnetic fields. The device is based on the Josephson junction effect. The magnetic flux in the superconducting loop will be measured as a function of voltage. Two types of squids are available depending on direct current and radiofrequency. Applications of SQUIDs include detection of magnetic nanoparticles (Enpuku et al., 1999) and squid based magnetic resonance imaging (Buckenmaier et al., 2018). Squid based susceptometer is a versatile instrument which supports two types of measurements: VSM and dc scans (Hurt et al., 2013).

2.3.2.4 Magnetorelaxometry

Magnetorelaxometry (MRX) is a technique where the magnetic nanoparticles are immobilized by a brief magnetizing pulse and then SQUIDs will be used to measure the magnetization decay in the particles to determine the specificity and the degree of cell binding. This is based on Brownian relaxation and Neel relaxation mechanisms (Schmidl et al., 2007). The

superparamagnetic relaxometry was used to detect and localize sensitive cancer cells, which is a potential application of this method (De Haro et al., 2015; Johnson et al., 2012).

2.3.2.5 Atomic Force Microscopy (AFM)

The surface domain microstructure distribution of the magnetic particles was determined by measuring magnetic forces using atomic force microscopy (Saenz et al., 1987). The magnetic moment per unit mass was measured by the atomic force microscope (Park et al., 2007).

Magnetic force microscopy is also based on atomic force microscopy and is used to characterize SPIONs without labeling by collecting images in air and water (Cordova et al., 2017).

2.3.2.6 Hysteresis loop tracer equipment

This is used to measure low-frequency magnetic properties for thin layers (Crittenden Jr et al., 1951). Mn-Zn ferrite nanoparticles were characterized by this equipment to measure the coercivity, saturation magnetization and retentivity (Tangsali et al., 2011).

2.3.2.7 Ferromagnetic Resonance (FMR)

Ferromagnetic resonance is a spectroscopic technique used to characterize the magnetization of ferromagnetic nanoparticles, films and alloys (Brataas et al., 2002; Farle, 1998; T. Liu et al., 2014). This technique is based on the resonance phenomenon that happens when the frequency of sample magnetization matches with the frequency of external magnetic force. FMR was applied to characterize the Co-Fe core oxide shell nanoparticles (Kołtunowicz et al., 2017).

2.3.2.8 Hyperflux Velocimeter

The Hyperflux velocimeter is an instrument used to characterize magnetic particles in an isodynamic magnetic field and is based on principles of particle-tracking velocimetry (Chalmers et al., 1999; Gibson, 1936; Little et al., 2013; Zborowski et al., 1999; Zhou et al., 2016) and capture

dark-field images of the particle velocity tracks, thus analyzing twenty-three different characteristics of magnetic particles which include magnetophoretic mobility and particle size with the help of image analysis software. The instrument is used to quantify magnetic-labeled cells, identify distinct labeled cell populations and validate sample quality.

The instrument's hardware includes a flow system channel cell made up of borosilicate glass of 6 cm length and selectable cross-section, a magnetic assembly which creates an isodynamic field in such a way that the net magnetic force is perpendicular to gravity, an automated pump which helps to move the sample solution and priming buffer through the channel cell (Figures 2.4 and 2.5). It contains a dark-field LED light, high sensitivity and high resolution (4.4 μm) Grasshopper® monochrome 2.0 MP Fire-Wire CCD Camera (Point Grey), 2x to 8x telecentric lens (Edmund Optics) to capture the image frames at a rate of 30 frames per second. The 6x telecentric lens gives a 0.733 μm point-to-point resolution in the object plane within the liquid sample channel cell of 400 μm thick. These lenses are positioned between two Frantz type pole pieces(Gibson, 1936) to view the mapped isodynamic zone (Chalmers et al., 1999; Moore et al., 2000). Both camera and lens are positioned to a tri-axial micrometer stage which allows horizontal and vertical alignment of the camera onto the flow channel cell. A sample syringe and a prime buffer bottle are connected to one end of the channel cell while the other end is connected to a waste bottle. In these connections, solenoid pinch valves are used to control the flow through channel cell by means of 0.125-inch OD tubing. A DELL computer with a dual quad-core CPU design along with the Linux operating system (Kubuntu) is used to automate the process. Point Grey's FlyCapture Library was used to write the image capture and analysis in the IKOvision™, Cytotest™ and Magex™ softwares. Each image is permanently recorded and stored in the computer which allows us to replay the experiment and based on different intensity threshold

values and size gating settings, particle sample's magnetophoretic mobility, particle size and count along with twenty other characteristics are calculated automatically. The images are collected in sets, where each set represents a fresh fluid sample drawn using the vacuum pump.

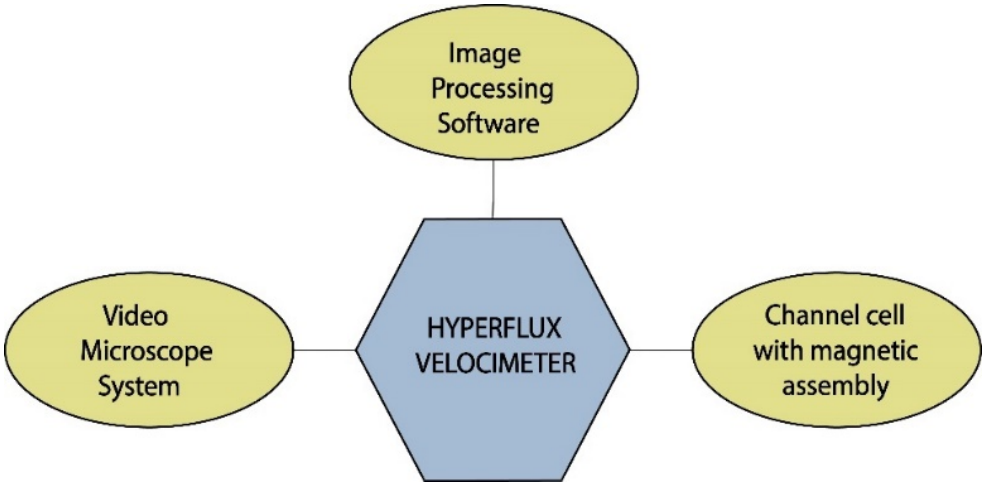

Figure 2.4 - Block diagram of the components of Hyperflux velocimeter.

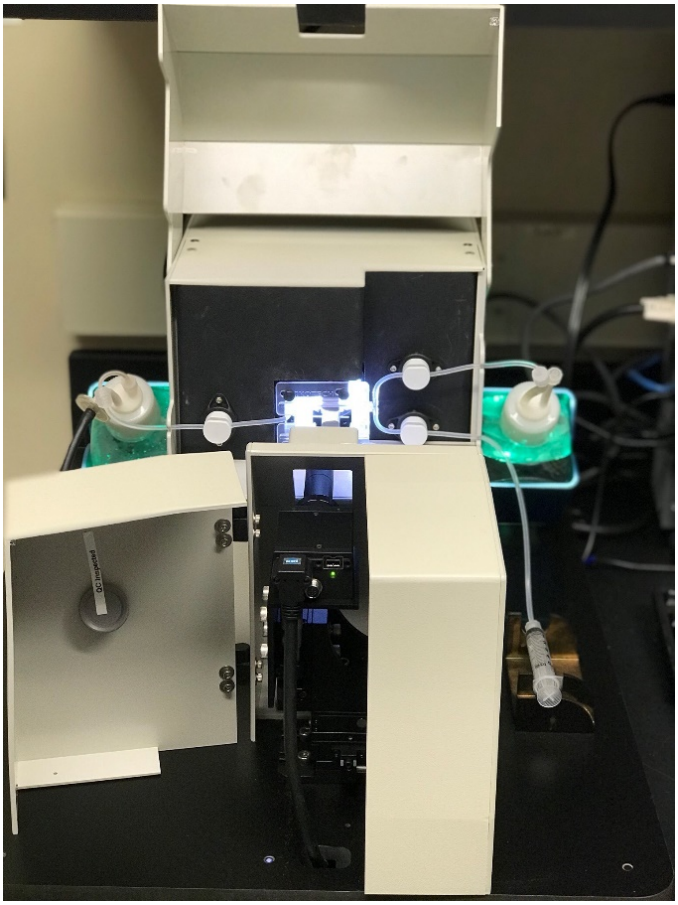

Figure 2.5 - Front view of Hyperflux Velocimeter- showing the microscopic camera, channel cell, sample syringe, buffer and waste containers.

2.3.2.9 Magnetic susceptibility measurement methods and devices

The magnetic susceptibility of different materials has been measured by different techniques and devices reported in the literature as given in Table 2.1.

Table 2.1 - Methods and devices used to measure magnetic susceptibility.

Method	Sample	Mechanism	Reference
Faraday Microbalance	Powdered samples, Selenium	Faraday method using torsion quartz microbalance	(Bakovets et al., 2018; Freyland & Cutler, 1980)
Superconducting Quantum Interference Device (SQUID)	Human iron stores	Josephson effect by Magnetometer- which measure small energy changes	(Brittenham et al., 1982)
Cryogenic Magnetometer	Rocks	Matrix susceptibility measurement in the high field	(Rochette, 1987)
High Field Fourier Transform NMR Spectroscopy	Paramagnetic particle solutions	H NMR frequency shifts with respect to the reference compound	(Sur, 1989)
Bartington MS2 sensors system	Water (diamagnetic), calibration sample (ferrimagnetic), Ferro	Sensors create a weak magnetic field by alternating current to	(Dearing, 1994)

	cassette tape (ferrimagnetic), steel wool (ferromagnetic)	detect magnetization of the material	
CS-2 apparatus and KLY-2 Kappabridge	Magnetic rocks	Measurement of thermal changes of magnetic susceptibility	(Hrouda, 1994)
NMR Spectroscopy	Insoluble solids: bone	Change in spectroscopic linewidth results in an induced frequency shift	(Hopkins & Wehrli, 1997)
High field torque meter	Rocks	N/A	(Banerjee & Stacey, 2013)

2.4 Magnetic Cell Separation

Magnetic cell separation depends on the theory of previously discussed parameters namely magnetic susceptibility, magnetic force, isodynamic magnetic field and magnetophoretic mobility of the labeled cells.

The magnetophoretic mobility of the labeled cells is given by

$$\mu_m = \frac{\Delta\chi V}{6\pi\eta R} \tag{2-20}$$

2.4.1 Parameters that affect Magnetophoretic mobility

In the literature, four parameters have been reported to affect the magnetophoretic mobility of cells labeled with secondary antibody-coated beads, namely antibody binding capacity of the cell population (ABC), secondary antibody binding amplification (Ψ), particle magnetic field interaction parameter ($\nabla\chi\, V_m$) and, particle diameter (D_c) (Mccloskey et al., 2003). For a labeled cell, the magnetophoretic mobility is given by

$$\mu_m = \frac{(ABC)\Psi n_3\, \Delta\chi V_m}{3\pi D_c \eta} = \frac{(n_1\theta_1\lambda_1)(n_2\theta_2\lambda_2)n_3\, \Delta\chi V_m}{3\pi D_c \eta} \qquad (2\text{-}21)$$

Where subscript 1 represents the primary antibody and 2 represents secondary antibody, n_1 is the number of antigen-binding sites per cell, n_2 is the number of binding sites on the primary antibody recognized by secondary antibody, n_3 is the number of magnetic nanoparticles conjugated to the antibody θ_1 is the fraction of antigen sites on the particle surface bound by a primary antibody, θ_2 is the fraction of sites on the primary antibody bound by the secondary antibody, λ_1 is the valence of primary antibody binding, λ_2 is the valence of primary antibody binding, ($n_1\ \theta_1\ \lambda_1$) is antibody binding capacity, ($n_2\ \theta_2\ \lambda_2$) is secondary antibody amplification (Ψ), $\Delta\chi$ is the difference in the magnetic susceptibility of particle and medium, V_m is the volume of magnetic particle, D_c is the particle diameter and η is the viscosity of the fluid medium.

2.4.2 Magnetic velocity and settling velocity

Settling velocity of the particle should also be considered when a particle is induced with magnetic velocity in a fluid medium with an applied external magnetic field. The settling velocity of the particle is given by

$$v_{settling} = \frac{\Delta\rho V}{6\pi\eta R} g \tag{2-22}$$

The ratio of the magnetic velocity and the settling velocity is given by

$$\frac{v_{magnetic}}{v_{settling}} = \frac{\Delta\chi}{\Delta\rho g} S_m \tag{2-23}$$

Assuming that the susceptibility and density of the particle are constant, the ratio of these velocities should be constant only if the applied magnetic pressure (S_m) is constant. The comparative studies of magnetically induced velocity and the settling velocity along with the effect of magnetophoretic mobility on settling velocity were reported in the literature by Jin et al. 2008. The size distribution of the particles will result in data spread of the magnetic as well as settling velocities (J. Xu et al., 2012).

2.4.3 Commercial magnetic cell separation technologies

The commercial magnetic cell separation devices and technologies available to the researchers are tabulated below (Table 2.2).

Table 2.2 - Commercially available magnetic cell separation devices in the market.

Company	Product	Description	Application
Miltenyi Biotech ("Miltenyi Biotec")	Cell Separation reagents, MACS® Microbeads, Cell sorters, Buffer and	MACS MicroBeads are superparamagnetic particles (50nm-diameter) which are very small to	Positive selection, Depletion, Untouched

	solutions, Flow Cytometers	activate cells. MACS Columns and MACS separator are used to isolate the labeled microbeads.	isolation, Sequential sorting
ThermoFisher Scientific ("ThermoFisher")	Dynabeads Human cell separation, Mouse cell separation by MagniSort technology	Dynabeads are superparamagnetic, mono-sized polymer beads. These beads, when bound to the target cells, are easy to isolate using a Dynal magnet	Positive and negative isolation, Depletion of unwanted cells
R&D Systems Inc. ("R&D Systems")	MagCellect™ cell selection and detection kits, Reagents, Positive and negative cell selection kits, Cell Enrichment Column Kits	Magcellect technology uses ferrofluids which contain superparamagnetic particles of diameter up to 150 nm. Higher binding rate and binding capacity are the key aspects of this technology	Rare cell detection, Positive isolation, Negative isolation

Menarini Silicon Biosystems Inc. ("Menarini Silicon Biosystems")	Cell Search® Circulating Tumor Cell (CTC) Kit, CellSearch® CTC Control Kit, CellSave Preservative Tube, CellTracks® AutoPrep® System, CellTracks Analyzer II®	Provides a laboratory platform which standardizes sample collection, cell capture, staining, enumeration and characterization of CTCs	Identification, counting and characterization of tumor cells
Stemcell Technologies Inc. ("Stemcell Technologies")	Cell Isolation using the following products: EasySep, RoboSep, StemCep, RossetteSep, SepMate	These products provide an easy, rapid and column-free cell selection system with open-gradient quadrupole magnetic field configuration. Target cell bounded to MNPs will be retained and separated	Positive selection and isolation, Depletion of unwanted cells
BD Biosciences ("BD Biosciences")	BD IMag™	BD IMagnet is an economical, strong permanent magnet	Positive and negative selection of leukocyte

			subpopulation, Cell enrichment
BioLegend ("BioLegend")	MojoSort™ magnetic cell separation system	MojoSort Magnet, nanobeads, Isolation kits	Positive and negative selection or depletion
Magnaquant LLC ("Magnaquant")	Quadrupole Magnetic Sorter (QMS)	Cell sorting is based on the magnetophoretic mobility of individual particles	Positive and negative selection with high throughput, pure and high quantity

2.5 Cell Labeling and Cellular Endocytosis

As discussed in section 2.4, magnetic cell separation could be achieved by labeling cells with different types of magnetic nanoparticles (Bohmer & Jordan, 2015; Gupta et al., 2003; Hanot et al., 2015). The internalization of magnetic nanoparticles depends on their surface properties (Kolosnjaj-Tabi et al., 2013). Endocytosis is a process in which external magnetic nanoparticles are taken into (internalized) the cell membrane by different mechanisms (Bohmer & Jordan, 2015; S. Zhang et al., 2015). Endocytosis is divided into two main categories, namely Phagocytosis and Pinocytosis. Phagocytosis is the process in which large particles are internalized into the cell cytoplasm by forming phagosomes. This mechanism helps in removal of cell debris and pathogens from the cell cytoplasm (Oh & Park, 2014; Sahay et al., 2010; S. Xu et al., 2013).

Pinocytosis, on the other hand, is the intake of extracellular fluid by invagination and formation of pockets. Pinocytosis is further classified into three different mechanisms, clathrin-dependent, clathrin-independent and macro-pinocytosis. Clathrin independent mechanism (Cheng et al., 2006) is further sub-divided into caveolae-mediated (Kiss & Botos, 2009; Nabi & Le, 2003) and clathrin & caveolae independent mechanisms (J. S. Kim et al., 2006). The caveolae & clathrin-independent mechanism is further classified based on the type of endocytosis proteins involved in the internalization process.

Magnetic nanoparticles with different surface modifications will bring in new chemical properties to the labeled cell system (Mok & Zhang, 2013). Endocytosis of magnetic nanoparticles depends on several factors (Sahay et al., 2010; Zablotskii et al., 2011; S. Zhang et al., 2015). The particle size and zeta potential (electrostatic interaction between the particle and surrounding biological fluid) are the important factors for cellular endocytosis mechanism (Cañete et al., 2010; Kania et al., 2018). Table 2.3 gives the hydrodynamic size, polydispersity index and zeta potential measured by dynamic light scattering technique for magnetic nanoparticles with different surface modifications.

Table 2.3 - Literature reported hydrodynamic size and zeta potential values for different magnetic beads with varied surface modifications, dispersed in distilled water and cell culture media.

Particle Type	Dispersed in distilled water			Dispersed in cell culture media			Reference
	Size (nm)	PdI	ZP (mV)	Size (nm)	PdI	ZP (mV)	
Starch (50 nm)	55 ± 5	0.28	2.9 ± 0.1	28 ± 0	0.32	-5.4 ± 0.5	(Schaub et al., 2014)
Starch (100 nm)			-9.6	71		-6.6	(Eberbeck et al., 2010)
	104.7 ± 1.7		-4.4 ± 0.5				(J. Zhang et al., 2013)
	104.1 ± 2.3	0.07	9 ± 0.8				(Cole, David, et al., 2011)
	110 ± 1	0.12	3.1 ± 0.2				(R. Ludwig et al., 2014)
				66		-6.6	(Eberbeck et al., 2010)
	98.2 ± 25	0.1	-11.3 ± 6.89				(Anani, 2018)
	105						(Zhou, 2017)
Starch (150 nm)	150		-4.88				(Bahring et al., 2012)
	135 ± 1	0.15	11.8 ± 0.4				(R. Ludwig et al., 2014)
Starch (200 nm)	170 ± 2	0.18	-3.1 ± 0.1				(R. Ludwig et al., 2014)
	182 ± 18		1 ± 6				(Riegler et al., 2013)
Starch	1400		-10	1500		-15	

				1300		-25	(Aires et al., 2017)
FluidMAG -Amine (50 nm)	79 ± 0	0.23	24.3 ± 2.4	78 ± 1	0.34	-7.8 ± 0.5	(Schaub et al., 2014)
FluidMAG -Amine (100 nm)	83 ± 1	0.15	34.5 ± 0.7	99 ± 1	0.33	-6.3 ± 0.3	
	90		45 ± 10			-25 ± 5	(Aires et al., 2017)
						-30	
	114.2 ± 1.2	0.15	54.6 ± 0.8				(Cole, David, et al., 2011)
Aminated Starch (100 nm)	136.3 ± 5.5		38.9 ± 3.2				(J. Zhang et al., 2013)
	134.3 ± 2.1	0.06	58.9 ± 0.6				(Cole, David, et al., 2011)
	131.2 ± 34.1	0.12	16.7 ± 7.29				(Anani, 2018)
	136.2 ± 0.28	-	52.67 ± 0.98				
	139.43 ± 2.83	0.12	34.47 ± 1.19				
	139.43 ± 2.83	0.12	45 ± 2				(Yeh, 2018)
	170.6		36				(Zhou, 2017)
Dextran Sulfate DXS (100 nm)			-18	379		-14	(Eberbeck et al., 2010)

The properties of nanoparticles measured in distilled water and cell culture media are different due to the presence of several anionic proteins in the culture media. The hydrodynamic size and zeta potential values reported by different labs (Table 2.3) differ approximately by two standard deviations. According to (Eberbeck et al., 2010) and (Gräfe et al., 2016), the size and ZP of the beads are decreased when the concentration of the serum in the culture media is increased.

The endocytosis mechanisms of magnetic nanoparticles are investigated using different methods such as permanent micro-flux sources (Osman et al., 2012), chemical inhibitors (Dutta & Donaldson, 2012; Vercauteren et al., 2010). Different types of inhibitors are used to inhibit one/ or more types of endocytosis mechanisms (Dutta & Donaldson, 2012; Vercauteren et al., 2010). Some of the chemical inhibitors include hypertonic sucrose, potassium depletion, chlorpromazine, phenyl arsine oxide, chloroquine, monensin, filipin, cytochalasin-D, genistein, amiloride, dynasore.

Chlorpromazine is a cationic amphiphilic drug that inhibits clathrin-coated pit formation by a reversible translocation of clathrin from the cell plasma membrane. Potassium depletion inhibits the formation of clathrin-coated pits by dissociating the clathrin at the inner leaflet of the cell plasma membrane. Genistein is a tyrosine kinase inhibitor and inhibits caveolae-mediated endocytosis. Genistein causes local disruption of the actin network at the site of endocytosis and inhibits the employment of dynamin II. Methyl β - cyclodextrin (M β CD) is a cyclic oligomer of glucopyranoside that inhibits cholesterol-dependent endocytic processes by reversibly extracting the steroid out of the cell plasma. The dependence of endocytosis on lipid rafts is usually determined by M β CD (Vercauteren et al., 2010).

References

Abràmoff, M. D., Magalhães, P. J., & Ram, S. J. (2004). Image Processing with ImageJ Second Edition. In *Biophotonics International* (Vol. 11, Issue 7). https://doi.org/10.1017/CBO9781107415324.004.

Aires, A., Cabrera, D., Alonso-Pardo, L. C., Cortajarena, A. L., & Teran, F. J. (2017). Elucidation of the physicochemical properties ruling the colloidal stability of iron oxide nanoparticles under physiological conditions. *ChemNanoMat*, *3*(3), 183–189.

Anani, T. (2018). Matrix Metalloproteinase-Responsive Superparamagnetic Iron Oxide Nanoparticles (SPIONs) to Distinguish Between Aggressive and Indolent Cancer. *Auburn University Dissertations*.

Anirudhan, T. S., Gopal, S. S., & Sandeep, S. (2014). Synthesis and characterization of montmorillonite/N-(carboxyacyl) chitosan coated magnetic particle nanocomposites for controlled delivery of paracetamol. *Applied Clay Science*, *88*, 151–158.

Assa, F., Jafarizadeh-Malmiri, H., Ajamein, H., Vaghari, H., Anarjan, N., Ahmadi, O., & Berenjian, A. (2017). Chitosan magnetic nanoparticles for drug delivery systems. *Critical Reviews in Biotechnology*, *37*(4), 492–509.

Bahring, F., Schlenk, F., Wotschadlo, J., Buske, N., Liebert, T., Bergemann, C., Heinze, T., Hochhaus, A., Fischer, D., & Clement, J. H. (2012). Suitability of viability assays for testing biological effects of coated superparamagnetic nanoparticles. *IEEE Transactions on Magnetics*, *49*(1), 383–388.

Bakovets, V. V, Sotnikov, A. V, Agazhanov, A. S., Stankus, S. V, Korotaev, E. V, Pishchur, D. P., & Shkatulov, A. I. (2018). Some features of thermophysical properties of $γ$-Gd2S3 ceramics based on real structure. *Journal of the American Ceramic Society*, *101*(10), 4773–

4782.

Banerjee, S. K., & Stacey, F. D. (2013). The high-field torque-meter method of measuring magnetic anisotropy of rocks. In *Developments in Solid Earth Geophysics* (Vol. 3, pp. 470–476). Elsevier.

BD Biosciences. (n.d.). Retrieved October 10, 2018, from http://www.bdbiosciences.com/us/reagents/research/magnetic-cell-separation/other-species-cell-separation-reagents/cell-separation-magnet/p/552311.

Bhukal, S., Dhiman, M., Bansal, S., Tripathi, M. K., & Singhal, S. (2016). Substituted Co-Cu-Zn nanoferrites: Synthesis, fundamental and redox catalytic properties for the degradation of methyl orange. *RSC Advances*, *6*(2), 1360–1375. https://doi.org/10.1039/c5ra22561b.

Binns, C., Prieto, P., Baker, S., Howes, P., Dondi, R., Burley, G., Lari, L., Kröger, R., Pratt, A., Aktas, S., & Mellon, J. K. (2012). Preparation of hydrosol suspensions of elemental and core-shell nanoparticles by co-deposition with water vapour from the gas-phase in ultra-high vacuum conditions. *Journal of Nanoparticle Research*, *14*(9). https://doi.org/10.1007/s11051-012-1136-6.

BioLegend. (n.d.). Retrieved October 10, 2018, from https://www.biolegend.com/mojosort

Bohmer, N., & Jordan, A. (2015). Caveolin-1 and CDC42 mediated endocytosis of silica-coated iron oxide nanoparticles in HeLa cells. *Beilstein Journal of Nanotechnology*, *6*(1), 167–176. https://doi.org/10.3762/bjnano.6.16.

Brataas, A., Tserkovnyak, Y., Bauer, G. E. W., & Halperin, B. I. (2002). Spin battery operated by ferromagnetic resonance. *Physical Review B*, *66*(6), 60404.

Brittenham, G. M., Farrell, D. E., Harris, J. W., Feldman, E. S., Danish, E. H., Muir, W. A., Tripp, J. H., & Bellon, E. M. (1982). Magnetic-susceptibility measurement of human iron

stores. *New England Journal of Medicine*, *307*(27), 1671–1675.

Buckenmaier, K., Rudolph, M., Fehling, P., Back, C., Bernarding, J., Koelle, D., Kleiner, R., Scheffler, K., & Plaumann, M. (2018). SQUID based magnetic resonance imaging for the investigation of in situ and in vivo hyperpolarization techniques. *13th Annual Meeting of the European Society for Molecular Imaging (EMIM 2018)*.

Cañete, M., Soriano, J., Villanueva, A., Roca, A. G., Veintemillas, S., Serna, C. J., Miranda, R., & Del Puerto Morales, M. (2010). The endocytic penetration mechanism of iron oxide magnetic nanoparticles with positively charged cover: a morphological approach. *International Journal of Molecular Medicine*, *26*(4), 533–539.

Carpenter, E. E., Sims, J. A., Wienmann, J. A., Zhou, W. L., & O'Connor, C. J. (2000). Magnetic properties of iron and iron platinum alloys synthesized via microemulsion techniques. *Journal of Applied Physics*, *87*(9), 5615–5617. https://doi.org/10.1063/1.372468

Carpino, F., Moore, L. R., Chalmers, J. J., Zborowski, M., & Williams, P. S. (2005). Quadrupole magnetic field-flow fractionation for the analysis of magnetic nanoparticles. *Journal of Physics: Conference Series*, *17*(1), 174.

Cerbino, R. (2018). Quantitative optical microscopy of colloids: The legacy of Jean Perrin. *Current Opinion in Colloid & Interface Science*.

Chalmers, J. J., Zhao, Y., Nakamura, M., Melnik, K., Lasky, L., Moore, L., & Zborowski, M. (1999). Instrument to determine the magnetophoretic mobility of labeled, biological cells and paramagnetic particles. *Journal of Magnetism and Magnetic Materials*, *194*(1), 231–241. https://doi.org/10.1016/S0304-8853(98)00557-5.

Chen, D.-H., & He, X.-R. (2001). Synthesis of nickel ferrite nanoparticles by sol-gel method. *Materials Research Bulletin*, *36*(7–8), 1369–1377.

Cheng, Z.-J., Singh, R. D., Sharma, D. K., Holicky, E. L., Hanada, K., Marks, D. L., & Pagano, R. E. (2006). Distinct mechanisms of clathrin-independent endocytosis have unique sphingolipid requirements. *Molecular Biology of the Cell*, *17*(7), 3197–3210.

Chertok, B., Moffat, B. A., David, A. E., Yu, F., Bergemann, C., Ross, B. D., & Yang, V. C. (2008). Iron oxide nanoparticles as a drug delivery vehicle for MRI monitored magnetic targeting of brain tumors. *Biomaterials*, *29*(4), 487–496.

Clarke, J. (1994). SQUIDs. *Scientific American*, *271*(2), 46–53.

Cole, A. J., David, A. E., Wang, J., Galbán, C. J., Hill, H. L., & Yang, V. C. (2011). Polyethylene glycol modified, cross-linked starch-coated iron oxide nanoparticles for enhanced magnetic tumor targeting. *Biomaterials*, *32*(8), 2183–2193. https://doi.org/10.1016/j.biomaterials.2010.11.040.

Cole, A. J., David, A. E., Wang, J., Galbán, C. J., & Yang, V. C. (2011). Magnetic brain tumor targeting and biodistribution of long-circulating PEG-modified, cross-linked starch-coated iron oxide nanoparticles. *Biomaterials*, *32*(26), 6291–6301. https://doi.org/10.1016/j.biomaterials.2011.05.024.

Cole, A. J., Yang, V. C., & David, A. E. (2011). Cancer theranostics: the rise of targeted magnetic nanoparticles. *Trends in Biotechnology*, *29*(7), 323–332.

Collins, T. J. (2007). ImageJ for microscopy. *Biotechniques*, *43*(S1), S25--S30.

Cordova, G., Attwood, S., Gaikwad, R., Gu, F., & Leonenko, Z. (2017). Magnetic force microscopy characterization of superparamagnetic iron oxide nanoparticles (SPIONs). *ArXiv Preprint ArXiv:1704.08316*.

Crittenden Jr, E. C., Hudimac, A. A., & Strough, R. I. (1951). Magnetization hysteresis loop tracer for long specimens of extremely small cross section. *Review of Scientific Instruments*,

22(12), 872–877.

Cunningham, C. H., Arai, T., Yang, P. C., McConnell, M. V, Pauly, J. M., & Conolly, S. M. (2005). Positive contrast magnetic resonance imaging of cells labeled with magnetic nanoparticles. *Magnetic Resonance in Medicine: An Official Journal of the International Society for Magnetic Resonance in Medicine*, *53*(5), 999–1005.

De Haro, L. P., Karaulanov, T., Vreeland, E. C., Anderson, B., Hathaway, H. J., Huber, D. L., Matlashov, A. N., Nettles, C. P., Price, A. D., Monson, T. C., & others. (2015). Magnetic relaxometry as applied to sensitive cancer detection and localization. *Biomedical Engineering/Biomedizinische Technik*, *60*(5), 445–455.

Dearing, J. A. (1994). Environmental magnetic susceptibility using the Bartington MS2 System. *Kenilworth U.K.: Chi Publishing*, 52.

Deatsch, A. E., & Evans, B. A. (2014). Heating efficiency in magnetic nanoparticle hyperthermia. *Journal of Magnetism and Magnetic Materials*, *354*, 163–172. https://doi.org/10.1016/j.jmmm.2013.11.006.

Deng, J., He, C., Peng, Y., Wang, J., Long, X., Li, P., & Chan, A. S. C. (2003). Magnetic and conductive Fe3O4--polyaniline nanoparticles with core--shell structure. *Synthetic Metals*, *139*(2), 295–301.

Dutta, D., & Donaldson, J. G. (2012). *Intended specificity and unintended consequences*. *December*, 203–208.

Eberbeck, D., Kettering, M., Bergemann, C., Zirpel, P., Hilger, I., & Trahms, L. (2010). Quantification of the aggregation of magnetic nanoparticles with different polymeric coatings in cell culture medium. *Journal of Physics D: Applied Physics*, *43*(40), 405002.

El-Boubbou, K., Azar, D., Bekdash, A., & Abi-Habib, R. J. (2017). Doxironide Magnetic

Nanoparticles for Selective Drug Delivery to Human Acute Myeloid Leukemia. *Journal of Biomedical Nanotechnology*, *13*(5), 500–512.

Enpuku, K., Minotani, T., Gima, T., Kuroki, Y., Itoh, Y., Yamashita, M., Katakura, Y., & Kuhara, S. (1999). Detection of magnetic nanoparticles with superconducting quantum interference device (SQUID) magnetometer and application to immunoassays. *Japanese Journal of Applied Physics*, *38*(10A), L1102.

Farle, M. (1998). Ferromagnetic resonance of ultrathin metallic layers. *Reports on Progress in Physics*, *61*(7), 755.

Filippousi, M., Altantzis, T., Stefanou, G., Betsiou, M., Bikiaris, D. N., Angelakeris, M., Pavlidou, E., Zamboulis, D., & Van Tendeloo, G. (2013). Polyhedral iron oxide core-shell nanoparticles in a biodegradable polymeric matrix: Preparation, characterization and application in magnetic particle hyperthermia and drug delivery. *RSC Advances*, *3*(46), 24367–24377. https://doi.org/10.1039/c3ra43747g.

Foner, S. (1956). Vibrating sample magnetometer. *Review of Scientific Instruments*, *27*(7), 548.

Foner, S. (1959). Versatile and sensitive vibrating-sample magnetometer. *Review of Scientific Instruments*, *30*(7), 548–557.

Fredrick, S. A. (1960). Production of magnetic iron particles. *U.S. Patent No. 2,938,781*. Washington, DC: U.S. Patent and Trademark Office.

Frey, N. A., Peng, S., Cheng, K., & Sun, S. (2009). Magnetic nanoparticles: Synthesis, functionalization, and applications in bioimaging and magnetic energy storage. *Chemical Society Reviews*, *38*(9), 2532–2542. https://doi.org/10.1039/b815548h.

Freyland, W., & Cutler, M. (1980). Magnetic susceptibility of expanded liquid selenium. *Journal of the Chemical Society, Faraday Transactions 2: Molecular and Chemical Physics*, *76*,

756–760.

Gangopadhyay, P., Gallet, S., Franz, E., Persoons, A., & Verbiest, T. (2005). Novel superparamagnetic core (shell) nanoparticles for magnetic targeted drug delivery and hyperthermia treatment. *IEEE Transactions on Magnetics*, *41*(10), 4194–4196.

Gherca, D., Pui, A., Cornei, N., Cojocariu, A., Nica, V., & Caltun, O. (2012). Synthesis, characterization and magnetic properties of MFe2O4(M=Co, Mg, Mn, Ni) nanoparticles using ricin oil as capping agent. *Journal of Magnetism and Magnetic Materials*, *324*(22), 3906–3911. https://doi.org/10.1016/j.jmmm.2012.06.027.

Gibson, F. S. (1936). Magnetic separation method and means. *US Patent no. US2056426A* Washington, DC, USA: U.S. Patent and Trademark Office.

Giddings, J. Calvin. (1968). Nonequilibrium Theory of Field-Flow Fractionation. *The Journal of Chemical Physics*, *49*(1), 81–85. https://doi.org/10.1063/1.1669863.

Giddings, J C. (1993). Field-flow fractionation: analysis of macromolecular, colloidal, and particulate materials. *Science*, *260*(5113), 1456 LP – 1465. http://science.sciencemag.org/content/260/5113/1456.abstract

Giddings, J Calvin. (1966). A New Separation Concept Based on a Coupling of Concentration and Flow Nonuniformities. *Separation Science*, *1*(1), 123–125. https://doi.org/10.1080/01496396608049439.

Giddings, J Calvin. (1985). A System Based on Split-Flow Lateral-Transport Thin (SPLITT) Separation Cells for Rapid and Continuous Particle Fractionation. *Separation Science and Technology*, *20*(9–10), 749–768. https://doi.org/10.1080/01496398508060702.

Giddings, J Calvin. (1992). Optimization of Transport-Driven Continuous SPLITT Fractionation. *Separation Science and Technology*, *27*(11), 1489–1504.

https://doi.org/10.1080/01496399208019438.

Giddings, J Calvin, Hovingh, M. E., & Thompson, G. H. (1970). Measurement of thermal diffusion factors by thermal field-flow fractionation. *The Journal of Physical Chemistry*, *74*(24), 4291–4294.

Gräfe, C., Weidner, A., vd Lühe, M., Bergemann, C., Schacher, F. H., Clement, J. H., & Dutz, S. (2016). Intentional formation of a protein corona on nanoparticles: serum concentration affects protein corona mass, surface charge, and nanoparticle–cell interaction. *The International Journal of Biochemistry & Cell Biology*, *75*, 196–202.

Gupta, A. K., Berry, C., Gupta, M., & Curtis, A. (2003). Receptor-mediated targeting of magnetic nanoparticles using insulin as a surface ligand to prevent endocytosis. *IEEE Transactions on Nanobioscience*, *2*(4), 255–261. https://doi.org/10.1109/TNB.2003.820279

Haacke, E. M., Brown, R. W., Thompson, M. R., Venkatesan, R., & others. (1999). *Magnetic resonance imaging: physical principles and sequence design* (Vol. 82). Wiley-Liss New York.

Häfeli, U. O., Ciocan, R., & Dailey, J. P. (2002). Characterization of magnetic particles and microspheres and their magnetophoretic mobility using a digital microscopy method. *European Cells and Materials*, *3*(SUPPL. 2), 24–27.

Hanot, C. C., Choi, Y. S., Anani, T. B., Soundarrajan, D., & David, A. E. (2015). Effects of iron-oxide nanoparticle surface chemistry on uptake kinetics and cytotoxicity in CHO-K1 cells. *International Journal of Molecular Sciences*, *17*(1), 1–15. https://doi.org/10.3390/ijms17010054.

Hergt, R., Dutz, S., Müller, R., & Zeisberger, M. (2006). Magnetic particle hyperthermia: nanoparticle magnetism and materials development for cancer therapy. *Journal of Physics:*

Condensed Matter, *18*(38), S2919.

Hergt, R., Dutz, S., & Röder, M. (2008). Effects of size distribution on hysteresis losses of magnetic nanoparticles for hyperthermia. *Journal of Physics Condensed Matter*, *20*(38). https://doi.org/10.1088/0953-8984/20/38/385214.

Hopkins, J. A., & Wehrli, F. W. (1997). Magnetic susceptibility measurement of insoluble solids by NMR: Magnetic susceptibility of bone. *Magnetic Resonance in Medicine*, *37*(4), 494–500.

Hrouda, F. (1994). A technique for the measurement of thermal changes of magnetic susceptibility of weakly magnetic rocks by the CS-2 apparatus and KLY-2 Kappabridge. *Geophysical Journal International*, *118*(3), 604–612.

Hu, M., Novo, C., Funston, A., Wang, H., Staleva, H., Zou, S., Mulvaney, P., Xia, Y., & Hartland, G. V. (2008). Dark-field microscopy studies of single metal nanoparticles: understanding the factors that influence the linewidth of the localized surface plasmon resonance. *Journal of Materials Chemistry*, *18*(17), 1949–1960.

Huang, J., Pen, H., Xu, Z., & Yi, C. (2008). Magnetic Fe3O4/poly (styrene-co-acrylamide) composite nanoparticles prepared by microwave-assisted emulsion polymerization. *Reactive and Functional Polymers*, *68*(1), 332–339.

Hurst, S. J. (2011). Biomedical nanotechnology. *Methods in Molecular Biology (Clifton, N.J.)*, *726*, 1–13. https://doi.org/10.1007/978-1-61779-052-2_1

Hurt, D., Li, S., & Amann, A. (2013). Versatile SQUID susceptometer with multiple measurement modes. *IEEE Transactions on Magnetics*, *49*(7), 3541–3544.

Inouye, K., Endo, R., Otsuka, Y., Miyashiro, K., Kaneko, K., & Ishikawa, T. (1982). Oxygenation of ferrous ions in reversed micelle and reversed microemulsion. *The Journal*

of Physical Chemistry, *86*(8), 1465–1469.

Ito, A., Shinkai, M., Honda, H., & Kobayashi, T. (2005). Medical application of functionalized magnetic nanoparticles. *Journal of Bioscience and Bioengineering*, *100*(1), 1–11. https://doi.org/10.1263/jbb.100.1.

Jain, T. K., Richey, J., Strand, M., Leslie-Pelecky, D. L., Flask, C. A., & Labhasetwar, V. (2008). Magnetic nanoparticles with dual functional properties: drug delivery and magnetic resonance imaging. *Biomaterials*, *29*(29), 4012–4021.

Jensen, E. C. (2013). Quantitative analysis of histological staining and fluorescence using ImageJ. *The Anatomical Record*, *296*(3), 378–381.

Jie, G., Yang, L., & Jinghai, Y. (2010). Influence of Co-Doping on Synthesis, Structure and Magnetic Properties of Ni Nanoparticles. *Rare Metal Materials and Engineering*, *39*, 328–331.

Jin, X., Zhao, Y., Richardson, A., Moore, L., Williams, P. S., Zborowski, M., & Chalmers, J. J. (2008). Differences in magnetically induced motion of diamagnetic, paramagnetic, and superparamagnetic microparticles detected by cell tracking velocimetry. *Analyst*, *133*(12), 1767–1775.

Jing, Y., Mal, N., Williams, P. S., Mayorga, M., Penn, M. S., Chalmers, J. J., & Zborowski, M. (2008). Quantitative intracellular magnetic nanoparticle uptake measured by live cell magnetophoresis. *The FASEB Journal*, *22*(12), 4239–4247.

Jing, Y., Moore, L. R., Schneider, T., Williams, P. S., Chalmers, J. J., Farag, S. S., Bolwell, B., & Zborowski, M. (2007). Negative selection of hematopoietic progenitor cells by continuous magnetophoresis. *Experimental Hematology*, *35*(4), 662–672.

Johnson, C., Adolphi, N. L., Butler, K. L., Lovato, D. M., Larson, R., Schwindt, P. D. D., &

Flynn, E. R. (2012). Magnetic relaxometry with an atomic magnetometer and SQUID sensors on targeted cancer cells. *Journal of Magnetism and Magnetic Materials*, *324*(17), 2613–2619.

Jones, T. B. (1995). Electromechanics of ParticlesCambridge Univ. *Press, Cambridge*.

Jönsson, P. E., Mamiya, H., & Takayama, H. (2004). Glassy dynamics of an interacting Fe--N nanoparticle system. *Journal of Magnetism and Magnetic Materials*, *272*, 1290–1291.

Jordan, A., Scholz, R., Wust, P., Fähling, H., & Felix, R. (1999). Magnetic fluid hyperthermia (MFH): Cancer treatment with AC magnetic field induced excitation of biocompatible superparamagnetic nanoparticles. *Journal of Magnetism and Magnetic Materials*, *201*(1–3), 413–419.

Kandasamy, G., Sudame, A., Luthra, T., Saini, K., & Maity, D. (2018). Functionalized hydrophilic superparamagnetic iron oxide nanoparticles for magnetic fluid hyperthermia application in liver cancer treatment. *ACS Omega*, *3*(4), 3991–4005.

Kania, G., Sternak, M., Jasztal, A., Chlopicki, S., Błażejczyk, A., Nasulewicz-Goldeman, A., Wietrzyk, J., Jasiński, K., Skórka, T., Zapotoczny, S., & others. (2018). Uptake and bioreactivity of charged chitosan-coated superparamagnetic nanoparticles as promising contrast agents for magnetic resonance imaging. *Nanomedicine: Nanotechnology, Biology and Medicine*, *14*(1), 131–140.

Katepetch, C., & Rujiravanit, R. (2011). Synthesis of magnetic nanoparticle into bacterial cellulose matrix by ammonia gas-enhancing in situ co-precipitation method. *Carbohydrate Polymers*, *86*(1), 162–170.

Kennedy, D. J., Todd, P., Logan, S., Becker, M., Papas, K. K., & Moore, L. R. (2007). Engineering quadrupole magnetic flow sorting for the isolation of pancreatic islets. *Journal*

of Magnetism and Magnetic Materials, *311*(1 SPEC. ISS.), 388–395. https://doi.org/10.1016/j.jmmm.2006.10.1160.

Kim, J.-E., Shin, J.-Y., & Cho, M.-H. (2012). Magnetic nanoparticles: an update of application for drug delivery and possible toxic effects. *Archives of Toxicology*, *86*(5), 685–700. https://doi.org/10.1007/s00204-011-0773-3.

Kim, J. S., Yoon, T. J., Yu, K. N., Mi, S. N., Woo, M., Kim, B. G., Lee, K. H., Sohn, B. H., Park, S. B., Lee, J. K., & Cho, M. H. (2006). Cellular uptake of magnetic nanoparticle is mediated through energy-dependent endocytosis in A549 cells. *Journal of Veterinary Science*, *7*(4), 321–326. https://doi.org/10.4142/jvs.2006.7.4.321.

Kim, Jaeyun, Kim, H. S., Lee, N., Kim, T., Kim, H., Yu, T., Song, I. C., Moon, W. K., & Hyeon, T. (2008). Multifunctional uniform nanoparticles composed of a magnetite nanocrystal core and a mesoporous silica shell for magnetic resonance and fluorescence imaging and for drug delivery. *Angewandte Chemie*, *120*(44), 8566–8569.

Kim, Jinho, Cho, H., Han, S. I., & Han, K. H. (2016). Single-Cell Isolation of Circulating Tumor Cells from Whole Blood by Lateral Magnetophoretic Microseparation and Microfluidic Dispensing. *Analytical Chemistry*, *88*(9), 4857–4863. https://doi.org/10.1021/acs.analchem.6b00570.

Kirby, D., Glynn, M., Kijanka, G., & Ducre, J. (2015). Rapid and cost-efficient enumeration of rare cancer cells from whole blood by low-loss centrifugo-magnetophoretic purification under stopped-flow conditions. *Cytometry Part A*, *87*(1), 74–80. https://doi.org/10.1002/cyto.a.22588.

Kirupakar, B. R., Vishwanath, B. A., & Sree, M. P. (2016). Vibrating Sample Magnetometer and Its Application In Characterisation Of Magnetic Property Of The Anti Cancer Drug

Magnetic Microspheres. *International Journal of Pharmaceutics and Drug Analysis*, *4*, 227–233.

Kiss, A. L., & Botos, E. (2009). Endocytosis via caveolae: Alternative pathway with distinct cellular compartments to avoid lysosomal degradation. *Journal of Cellular and Molecular Medicine*, *13*(7), 1228–1237. https://doi.org/10.1111/j.1582-4934.2009.00754.x.

Kolosnjaj-Tabi, J., Wilhelm, C., Clément, O., & Gazeau, F. (2013). Cell labeling with magnetic nanoparticles: opportunity for magnetic cell imaging and cell manipulation. *Journal of Nanobiotechnology*, *11 Suppl 1*(Suppl 1), S7. https://doi.org/10.1186/1477-3155-11-S1-S7

Kołtunowicz, T. N., Zukowski, P., Sidorenko, J., Bayev, V., Fedotova, J. A., Opielak, M., & Marczuk, A. (2017). Ferromagnetic resonance spectroscopy of CoFeZr-Al2O3 granular films containing FeCo core--oxide shell nanoparticles. *Journal of Magnetism and Magnetic Materials*, *421*, 98–102.

Lacava, B. M., Azevedo, R. B., Silva, L. P., Lacava, Z. G. M., Neto, K. S., Buske, N., Bakuzis, A. F., & Morais, P. C. (2000). Particle sizing of magnetite-based magnetic fluid using atomic force microscopy: A comparative study with electron microscopy and birefringence. *Applied Physics Letters*, *77*(12), 1876–1878.

Larson, T. A., Bankson, J., Aaron, J., & Sokolov, K. (2007). Hybrid plasmonic magnetic nanoparticles as molecular specific agents for MRI/optical imaging and photothermal therapy of cancer cells. *Nanotechnology*, *18*(32), 325101.

Lee, N., & Hyeon, T. (2012). Designed synthesis of uniformly sized iron oxide nanoparticles for efficient magnetic resonance imaging contrast agents. *Chemical Society Reviews*, *41*(7), 2575–2589.

Li, S.-D., & Huang, L. (2008). Pharmacokinetics and biodistribution of nanoparticles. *Molecular*

Pharmaceutics, *5*(4), 496–504.

Li, Z., Kawashita, M., Kudo, T. A., & Kanetaka, H. (2012). Sol-gel synthesis, characterization, and in vitro compatibility of iron nanoparticle-encapsulating silica microspheres for hyperthermia in cancer therapy. *Journal of Materials Science: Materials in Medicine*, *23*(10), 2461–2469. https://doi.org/10.1007/s10856-012-4735-y.

Lim, JitKang, Tilton, R. D., Eggeman, A., & Majetich, S. A. (2007). Design and synthesis of plasmonic magnetic nanoparticles. *Journal of Magnetism and Magnetic Materials*, *311*(1), 78–83.

Lim, Jitkang, Yeap, S. P., Che, H. X., & Low, S. C. (2013). Characterization of magnetic nanoparticle by dynamic light scattering. *Nanoscale Res Lett*, *8*(1), 381. https://doi.org/10.1186/1556-276X-8-381.

Little, C. A. E., Pellegrino, J., & Russek, S. E. (2013). Microfluidic platform for magnetic nanoparticle trapping and detection. *IEEE Transactions on Magnetics*, *49*(7), 3402–3405.

Liu, Q., & Xu, Z. (1995). Self-assembled monolayer coatings on nanosized magnetic particles using 16-mercaptohexadecanoic acid. *Langmuir*, *11*(12), 4617–4622.

Liu, T., Chang, H., Vlaminck, V., Sun, Y., Kabatek, M., Hoffmann, A., Deng, L., & Wu, M. (2014). Ferromagnetic resonance of sputtered yttrium iron garnet nanometer films. *Journal of Applied Physics*, *115*(17), 17A501.

Lopez-Dominguez, V., Quesada, A., Guzmán-M\’\inguez, J. C., Moreno, L., Lere, M., Spottorno, J., Giacomone, F., Fernández, J. F., Hernando, A., & Garc\’\ia, M. A. (2018). A simple vibrating sample magnetometer for macroscopic samples. *Review of Scientific Instruments*, *89*(3), 34707.

Lu, A. H., Salabas, E. L., & Schüth, F. (2007). Magnetic nanoparticles: Synthesis, protection,

functionalization, and application. *Angewandte Chemie - International Edition*, *46*(8), 1222–1244. https://doi.org/10.1002/anie.200602866.

Ludwig, F., Balceris, C., Jonasson, C., & Johansson, C. (2017). Analysis of ac susceptibility spectra for the characterization of magnetic nanoparticles. *IEEE Transactions on Magnetics*, *53*(11), 1–4.

Ludwig, R., Stapf, M., Dutz, S., Müller, R., Teichgräber, U., & Hilger, I. (2014). Structural properties of magnetic nanoparticles determine their heating behavior-an estimation of the in vivo heating potential. *Nanoscale Research Letters*, *9*(1), 602.

Magnaquant. (n.d.). Retrieved October 10, 2018, from https://www.magnaquant.com/technology/ikotech-qms/

Marek, R., Caruso, M., Rostami, A., Grinspan, J. B., & Sarma, J. Das. (2008). Magnetic cell sorting: a fast and effective method of concurrent isolation of high purity viable astrocytes and microglia from neonatal mouse brain tissue. *Journal of Neuroscience Methods*, *175*(1), 108–118.

Masubuchi, Y., Yamashita, S., Motohashi, T., Kikkawa, S., & Niederberger, M. (2011). Magnetite/maghemite mixture prepared in benzyl alcohol for the preparation of α -$Fe_{16}N_2$ with α-Fe. *Journal of the European Ceramic Society*, *31*(14), 2471–2474.

McBain, S. C., Yiu, H. H. P., & Dobson, J. (2008). Magnetic nanoparticles for gene and drug delivery. *International Journal of Nanomedicine*, *3*(2), 169.

Mccloskey, K. E., Chalmers, J. J., & Zborowski, M. (2003). Magnetic Cell Separation : Characterization of Magnetophoretic Mobility to enrich or deplete cells of interest from a heterogeneous. *Analytical Chemistry*, *75*(24), 6868–6874. https://doi.org/10.1021/ac034315j.

McCloskey, K. E., Chalmers, J. J., & Zborowski, M. (2000). Magnetophoretic mobilities correlate to antibody binding capacities. *Cytometry*, *40*(4), 307–315. https://doi.org/10.1002/1097-0320(20000801)40:4<307::AID-CYTO6>3.0.CO;2-H.

McCloskey, K. E., Comella, K., Chalmers, J. J., Margel, S., & Zborowski, M. (2001). Mobility measurements of immunomagnetically labeled cells allow quantitation of secondary antibody binding amplification. *Biotechnology and Bioengineering*, *75*(6), 642–655. https://doi.org/10.1002/bit.10040.

McCloskey, K. E., Moore, L. R., Hoyos, M., Rodriguez, A., Chalmers, J. J., & Zborowski, M. (2003). Magnetophoretic cell sorting is a function of antibody binding capacity. *Biotechnology Progress*, *19*(3), 899–907. https://doi.org/10.1021/bp020285e

Menarini Silicon biosystems. (n.d.). Retrieved October 10, 2018, from https://www.cellsearchruo.com/

Meng, C., Zhikun, W., Qiang, L., Chunling, L., Shuangqing, S., & Songqing, H. (2018). Preparation of amino-functionalized Fe3O4@ mSiO2 core-shell magnetic nanoparticles and their application for aqueous Fe3+ removal. *Journal of Hazardous Materials*, *341*, 198–206.

Miltenyi Biotec. (n.d.). Retrieved October 10, 2018, from https://www.miltenyibiotec.com/US-en/products/macs-cell-separation.html.

Moise, S., Céspedes, E., Soukup, D., Byrne, J. M., El Haj, A. J., & Telling, N. D. (2017). The cellular magnetic response and biocompatibility of biogenic zinc-and cobalt-doped magnetite nanoparticles. *Scientific Reports*, *7*, 39922.

Mok, H., & Zhang, M. (2013). Superparamagnetic iron oxide nanoparticle-based delivery systems for biotherapeutics. *Expert Opinion on Drug Delivery*, *10*(1), 73–87. https://doi.org/10.1517/17425247.2013.747507.

Moore, L. R., Zborowski, M., Nakamura, M., McCloskey, K., Gura, S., Zuberi, M., Margel, S., & Chalmers, J. J. (2000). The use of magnetic-doped polymeric microspheres in calibrating cell tracking velocimetry. *J. Biochem. Biophys. Methods*, *44*, 115–130.

Morris, S. A., & Slesnick, T. C. (2018). Magnetic resonance imaging. *Visual Guide to Neonatal Cardiology*, 104–108.

Na, H. Bin, Lee, J. H., An, K., Park, Y. Il, Park, M., Lee, I. S., Nam, D.-H., Kim, S. T., Kim, S.-H., Kim, S.-W., & others. (2007). Development of a T1 contrast agent for magnetic resonance imaging using MnO nanoparticles. *Angewandte Chemie*, *119*(28), 5493–5497.

Nabi, I. R., & Le, P. U. (2003). Caveolae/raft-dependent endocytosis. *Journal of Cell Biology*, *161*(4), 673–677. https://doi.org/10.1083/jcb.200302028.

Oh, N., & Park, J.-H. (2014). Endocytosis and exocytosis of nanoparticles in mammalian cells. *International Journal of Nanomedicine*, *9*(Suppl 1), 51.

Osman, O., Zanini, L. F., Frénéa-Robin, M., Dumas-Bouchiat, F., Dempsey, N. M., Reyne, G., Buret, F., & Haddour, N. (2012). Monitoring the endocytosis of magnetic nanoparticles by cells using permanent micro-flux sources. *Biomedical Microdevices*, *14*(5), 947–954. https://doi.org/10.1007/s10544-012-9673-4.

Pankhurst, Q. A., Connolly, J., Jones, S. K., & Dobson, J. J. (2003). Applications of magnetic nanoparticles in biomedicine. *Journal of Physics D: Applied Physics*, *36*(13), R167.

Park, J. W., Yoo, I. S., Chang, W. S., Lee, E. C., Ju, H., Chung, B. H., & Kim, B. S. (2007). Magnetic moment measurement of magnetic nanoparticles using atomic force microscopy. *Measurement Science and Technology*, *19*(1), 17005.

Peyman, S. A., Iles, A., & Pamme, N. (2009). Mobile magnetic particles as solid-supports for rapid surface-based bioanalysis in continuous flow. *Lab on a Chip*, *9*(21), 3110–3117.

Popa, M., Hong, L. Van, & Kakihana, M. (2003). *Particle morphology characterization and magnetic properties of LaMnO 3 + d perovskites*. *327*, 237–240.

R&D Systems. (n.d.). Retrieved October 10, 2018, from https://www.rndsystems.com/products/magcellect-tm-cell-selection-kits-reagents

Rashid, M., Gafur, M. A., Sharafat, M. K., Minami, H., Miah, M. A. J., & Ahmad, H. (2017). Biocompatible microcrystalline cellulose particles from cotton wool and magnetization via a simple in situ co-precipitation method. *Carbohydrate Polymers*, *170*, 72–79.

Reece, L. M., Sanders, L., Kennedy, D., Guernsey, B., Todd, P., & Leary, J. F. (2010). *High-throughput magnetic flow sorting of human cells selected on the basis of magnetophoretic mobility*. *February 2010*, 75680P. https://doi.org/10.1117/12.842956.

Reece, L. M., Sanders, L., Kennedy, D., Guernsey, B., Todd, P., & Leary, J. F. (2010). High-throughput magnetic flow sorting of human cells selected on the basis of magnetophoretic mobility. *Imaging, Manipulation, and Analysis of Biomolecules, Cells, and Tissues VIII*, *7568*, 75680P.

Reguera, J., de Aberasturi, D. J., Henriksen-Lacey, M., Langer, J., Espinosa, A., Szczupak, B., Wilhelm, C., & Liz-Marzán, L. M. (2017). Janus plasmonic--magnetic gold--iron oxide nanoparticles as contrast agents for multimodal imaging. *Nanoscale*, *9*(27), 9467–9480.

Reiss, G., & Hütten, A. (2016). Magnetic nanoparticles. In *Handbook of nanophysics* (pp. 28–40). CRC press.

Rembaum, A., Yen, S.-P. S., & Dreyer, W. J. (1976). Crosslinked, porous, polyacrylate beads. *U.S. Patent No. 3,957,741*. Washington, DC: U.S. Patent and Trademark Office.

Riegler, J., Liew, A., Hynes, S. O., Ortega, D., O'Brien, T., Day, R. M., Richards, T., Sharif, F., Pankhurst, Q. A., & Lythgoe, M. F. (2013). Superparamagnetic iron oxide nanoparticle

targeting of MSCs in vascular injury. *Biomaterials*, *34*(8), 1987–1994.

Rochette, P. (1987). Magnetic susceptibility of the rock matrix related to magnetic fabric studies. *Journal of Structural Geology*, *9*(8), 1015–1020.

Rocklage, S. M., Kucharczyk, J., & Moseley, M. E. (1998). Magnetic resonance imaging. *U.S. Patent No. 5,833,947*. Washington, DC: U.S. Patent and Trademark Office.

Saenz, J. J., Garcia, N., Grütter, P., Meyer, E., Heinzelmann, H., Wiesendanger, R., Rosenthaler, L., Hidber, H. R., & Güntherodt, H.-J. (1987). Observation of magnetic forces by the atomic force microscope. *Journal of Applied Physics*, *62*(10), 4293–4295.

Sahay, G., Alakhova, D. Y., & Kabanov, A. V. (2010). Endocytosis of nanomedicines. *Journal of Controlled Release*, *145*(3), 182–195.

Sajja, V. S K, Kennedy, D. J., Todd, P. W., & Hanley, T. R. (2011). Computational fluid dynamics simulation of a quadrupole magnetic sorter flow channel: Effect of splitter position on nonspecific crossover. *Canadian Journal of Chemical Engineering*, *89*(5), 1068–1075. https://doi.org/10.1002/cjce.20541.

Sajja, Venkata Sunil Kumar, Hanley, T. R., Gapsis, H., Guernsey, B., Kennedy, D. J., Taylor, M. J., Papas, K. K., & Todd, P. W. (2011). Application of magnetic particle tracking velocimetry to quadrupole magnetic sorting of porcine pancreatic islets. *Biotechnology and Bioengineering*, *108*(9), 2107–2117. https://doi.org/10.1002/bit.23157.

Sajja, Venkata Sunil Kumar, Hanley, T. R., Gapsis, H., Guernsey, B., Kennedy, D. J., Taylor, M. J., Papas, K. K., & Todd, P. W. (2011). Application of magnetic particle tracking velocimetry to quadrupole magnetic sorting of porcine pancreatic islets. *Biotechnology and Bioengineering*, *108*(9), 2107–2117.

Schaub, N. J., Rende, D., Yuan, Y., Gilbert, R. J., & Borca-Tasciuc, D.-A. (2014). Reduced

astrocyte viability at physiological temperatures from magnetically activated iron oxide nanoparticles. *Chemical Research in Toxicology*, *27*(12), 2023–2035.

Schenck, J. F. (1996). The role of magnetic susceptibility in magnetic resonance imaging: MRI magnetic compatibility of the first and second kinds. *Medical Physics*, *23*(6), 815–850.

Schmidl, F., Weber, P., Koettig, T., Büttner, M., Prass, S., Becker, C., Mans, M., Heinrich, J., Röder, M., Wagner, K., & others. (2007). Characterization of energy barrier and particle size distribution of lyophilized ferrofluids by magnetic relaxation measurements. *Journal of Magnetism and Magnetic Materials*, *311*(1), 171–175.

Schneider, C. A., Rasband, W. S., & Eliceiri, K. W. (2012). NIH Image to ImageJ: 25 years of image analysis. *Nature Methods*, *9*(7), 671.

Sevgi, F., Bagkesici, U., Kursunlu, A. N., & Guler, E. (2018). Fe (III), Co (II), Ni (II), Cu (II) and Zn (II) complexes of schiff bases based-on glycine and phenylalanine: Synthesis, magnetic/thermal properties and antimicrobial activity. *Journal of Molecular Structure*, *1154*, 256–260.

Sood, A., Arora, V., Shah, J., Kotnala, R. K., & Jain, T. K. (2017). Multifunctional gold coated iron oxide core-shell nanoparticles stabilized using thiolated sodium alginate for biomedical applications. *Materials Science and Engineering: C*, *80*, 274–281.

Stemcell Technologies. (n.d.). Retrieved October 10, 2018, from https://www.stemcell.com/products/brands/easysep-cell-separation.html

Sun, S., Murray, C. B., Weller, D., Folks, L., & Moser, A. (2000). Monodisperse FePt nanoparticles and ferromagnetic FePt nanocrystal superlattices. *Science*, *287*(5460), 1989–1992.

Sur, S. K. (1989). Measurement of magnetic susceptibility and magnetic moment of

paramagnetic molecules in solution by high-field Fourier transform NMR spectroscopy. *Journal of Magnetic Resonance (1969)*, *82*(1), 169–173.

Suwa, M., & Watarai, H. (2001). Magnetophoretic velocimetry of manganese(II) in a single emulsion droplet at the femtomole level. *Analytical Chemistry*, *73*(21), 5214–5219. https://doi.org/10.1021/ac010418v.

Tadic, M., Panjan, M., Damnjanovic, V., & Milosevic, I. (2014). Magnetic properties of hematite (α-Fe_2O_3) nanoparticles prepared by hydrothermal synthesis method. *Applied Surface Science*, *320*, 183–187.

Tang, Z. X., Hadjipanayis, G. C., Shah, S. I., Papaefthymiou, V., & Klabunde, K. J. (1993). Preparation of Fe4N from Nd-containing precursors. *Journal of Magnetism and Magnetic Materials*, *119*(1–2), 49–53.

Tangsali, R. B., Budkuley, J. S., Keluskar, S. H., Naik, G. K., & Watawe, S. C. (2011). *High density nanoparticle Mn-Zn ferrite synthesis, characterisation and magnetic properties*.

Tarasov, K. A., Isupov, V. P., Bokhonov, B. B., Gaponov, Y. A., Tolochko, B. P., Yulikov, M. M., Yudanov, V. F., Davidson, A., Beaunier, P., Marceau, E., & Che, M. (2008). Control of particle size via chemical composition: Structural and magnetic characterization of Ni-Co alloy nanoparticles encapsulated in lamellar mixed oxides. *Microporous and Mesoporous Materials*, *107*(1–2), 202–211. https://doi.org/10.1016/j.micromeso.2007.05.026.

ThermoFisher. (n.d.). Retrieved October 10, 2018, from https://www.thermofisher.com/us/en/home/life-science/cell-analysis/cell-isolation-and-expansion/cell-isolation.html.

Thiesen, B., & Jordan, A. (2008). Clinical applications of magnetic nanoparticles for hyperthermia. *International Journal of Hyperthermia*, *24*(6), 467–474.

Tresilwised, N., Pithayanukul, P., Mykhaylyk, O., Holm, P. S., Holzmuller, R., Anton, M., Thalhammer, S., Adiguzel, D., Doblinger, M., & Plank, C. (2010). Boosting oncolytic adenovirus potency with magnetic nanoparticles and magnetic force. *Molecular Pharmaceutics*, *7*(4), 1069–1089.

Veiseh, O., Gunn, J. W., & Zhang, M. (2010). Design and fabrication of magnetic nanoparticles for targeted drug delivery and imaging. *Advanced Drug Delivery Reviews*, *62*(3), 284–304.

Vercauteren, D., Vandenbroucke, R. E., Jones, A. T., Rejman, J., Demeester, J., De Smedt, S. C., Sanders, N. N., & Braeckmans, K. (2010). The use of inhibitors to study endocytic pathways of gene carriers: Optimization and pitfalls. *Molecular Therapy*, *18*(3), 561–569. https://doi.org/10.1038/mt.2009.281.

Watarai, H., & Namba, M. (2002). Capillary magnetophoresis of human blood cells and their magnetophoretic trapping in a flow system. *Journal of Chromatography A*, *961*(1), 3–8. https://doi.org/10.1016/S0021-9673(02)00748-3.

Weegman, B. P., Kumar Sajja, V. S., Suszynski, T. M., Rizzari, M. D., Scott III, W. E., Kitzmann, J. P., Mueller, K. R., Hanley, T. R., Kennedy, D. J., Todd, P. W., & others. (2016). Continuous quadrupole magnetic separation of islets during digestion improves purified porcine islet viability. *Journal of Diabetes Research*, *2016*.

Wickham, D. G., Mark, J., & Knox, K. (1967). Metal iron (III) oxides. *Inorganic Syntheses*, *9*, 152–156.

Wilhelm, C., & Gazeau, F. (2008). Universal cell labelling with anionic magnetic nanoparticles. *Biomaterials*, *29*(22), 3161–3174. https://doi.org/10.1016/j.biomaterials.2008.04.016

Wise, N., Grob, D. T., Morten, K., Thompson, I., & Sheard, S. (2015). Magnetophoretic velocities of superparamagnetic particles, agglomerates and complexes. *Journal of*

Magnetism and Magnetic Materials, *384*, 328–334. https://doi.org/10.1016/j.jmmm.2015.02.031.

Wise, N., Grob, T., Morten, K., Thompson, I., & Sheard, S. (2015). Magnetophoretic velocities of superparamagnetic particles, agglomerates and complexes. *Journal of Magnetism and Magnetic Materials*, *384*, 328–334.

Wong, J., Prout, J., & Seifalian, A. (2017). Magnetic nanoparticles: new perspectives in drug delivery. *Current Pharmaceutical Design*, *23*(20), 2908–2917.

Xu, H., Aguilar, Z. P., Yang, L., Kuang, M., Duan, H., Xiong, Y., Wei, H., & Wang, A. (2011). Antibody conjugated magnetic iron oxide nanoparticles for cancer cell separation in fresh whole blood. *Biomaterials*, *32*(36), 9758–9765.

Xu, J., Mahajan, K., Xue, W., Winter, J. O., Zborowski, M., & Chalmers, J. J. (2012). Simultaneous, single particle, magnetization and size measurements of micron sized, magnetic particles. *Journal of Magnetism and Magnetic Materials*, *324*(24), 4189–4199. https://doi.org/10.1016/j.jmmm.2012.07.039.

Xu, S., Olenyuk, B. Z., Okamoto, C. T., & Hamm-Alvarez, S. F. (2013). Targeting receptor-mediated endocytotic pathways with nanoparticles: rationale and advances. *Advanced Drug Delivery Reviews*, *65*(1), 121–138. https://doi.org/10.1016/j.addr.2012.09.041.

Xu, Z., Hou, Y., & Sun, S. (2007). Magnetic core/shell Fe3O4/Au and Fe3O4/Au/Ag nanoparticles with tunable plasmonic properties. *Journal of the American Chemical Society*, *129*(28), 8698–8699.

Yadav, K. S., Chuttani, K., Mishra, A. K., & Sawant, K. K. (2011). Effect of size on the biodistribution and blood clearance of etoposide-loaded PLGA nanoparticles. *PDA J Pharm Sci Technol*, *65*(2), 131–139.

Yan, L., Amirshaghaghi, A., Huang, D., Miller, J., Stein, J. M., Busch, T. M., Cheng, Z., & Tsourkas, A. (2018). Protoporphyrin IX (PpIX)-Coated Superparamagnetic Iron Oxide Nanoparticle (SPION) Nanoclusters for Magnetic Resonance Imaging and Photodynamic Therapy. *Advanced Functional Materials*, *28*(16), 1707030.

Yeh, B. J. (2018). Improving the homogeneity of superparamagnetic nanoparticles and a study of their physicochemical properties and applications. *Auburn University Dissertations*.

Yen, S. P. S., Rembaum, A., & Molday, R. S. (1979). Metal containing polymeric functional microspheres. *U.S. Patent No. 4,157,323*. Washington, DC: U.S. Patent and Trademark Office.

Yen, S. P. S., Rembaum, A., & Molday, R. S. (1980). Cell sorting apparatus. *U.S. Patent No. 4,219,411*. Washington, DC: U.S. Patent and Trademark Office.

Yu, F., Zhang, L., Huang, Y., Sun, K., David, A. E., & Yang, V. C. (2010). The magnetophoretic mobility and superparamagnetism of core-shell iron oxide nanoparticles with dual targeting and imaging functionality. *Biomaterials*, *31*(22), 5842–5848.

Zablotskii, V., Lunov, O., Dejneka, A., Jastrabk, L., Polyakova, T., Syrovets, T., & Simmet, T. (2011). Nanomechanics of magnetically driven cellular endocytosis. *Applied Physics Letters*, *99*(18), 1–4. https://doi.org/10.1063/1.3656020.

Zamora-Perez, P., Tsoutsi, D., Xu, R., & Rivera_Gil, P. (2018). Hyperspectral-Enhanced Dark Field Microscopy for Single and Collective Nanoparticle Characterization in Biological Environments. *Materials*, *11*(2), 243.

Zborowski, M., & Chalmers, J. J. (2011). *Magnetic cell separation* (Vol. 32). Elsevier.

Zborowski, M., Chalmers, J., & Moore, L. R. (1999). Method for determining particle characteristics. *US Patent US6142025*, Washington, DC, USA: U.S. Patent and Trademark

Office.

Zhang, H., Pan, D., & Duan, X. (2009). Synthesis, characterization, and magnetically controlled release behavior of novel core- shell structural magnetic ibuprofen-intercalated LDH nanohybrids. *The Journal of Physical Chemistry C*, *113*(28), 12140–12148.

Zhang, J., Shin, M. C., David, A. E., Zhou, J., Lee, K., He, H., & Yang, V. C. (2013). Long-circulating heparin-functionalized magnetic nanoparticles for potential application as a protein drug delivery platform. *Molecular Pharmaceutics*, *10*(10), 3892–3902.

Zhang, S., Gao, H., & Bao, G. (2015). Physical Principles of Nanoparticle Cellular Endocytosis. *ACS Nano*, *9*(9), 8655–8671. https://doi.org/10.1021/acsnano.5b03184.

Zhao, B., Wan, X., Song, W., Sun, Y., & Du, J. (2000). Nano-MgO particle addition in silver-sheathed $(Bi,Pb)_2Sr_2Ca_2Cu_3O_x$ tapes. *Physica C: Superconductivity and Its Applications*, *337*(1), 138–144. https://doi.org/10.1016/S0921-4534(00)00074-5.

Zhi, J., Wang, Y., Lu, Y., Ma, J., & Luo, G. (2006). In situ preparation of magnetic chitosan/Fe_3O_4 composite nanoparticles in tiny pools of water-in-oil microemulsion. *Reactive and Functional Polymers*, *66*(12), 1552–1558.

Zhou, C. (2017). Characterization and Quantification of Magnetic Particles and Magnetically Labeled Cells by Magnetic Cytometry. *Auburn University Dissertations*.

Zhou, C., Boland, E. D., Todd, P. W., & Hanley, T. R. (2016). Magnetic particle characterization—magnetophoretic mobility and particle size. *Cytometry Part A*, *89*(6), 585–593. https://doi.org/10.1002/cyto.a.22866.

Zhou, C., Choi, Y. S., David, A. E., Todd, P. W., & Hanley, T. R. (2018). Nanomaterial endocytosis: Estimation of particles per cell by magnetic measurement. *IEEE Magnetics Letters*, *9*, 7–11. https://doi.org/10.1109/LMAG.2018.2830754.

Zhou, C., Qian, Z., Choi, Y. S., David, A. E., Todd, P., & Hanley, T. R. (2017). Application of magnetic carriers to two examples of quantitative cell analysis. *Journal of Magnetism and Magnetic Materials*, *427*(November 2016), 25–28. https://doi.org/10.1016/j.jmmm.2016.11.009.

Zong, Y., Guo, J., Ke, T., Mohs, A. M., Parker, D. L., & Lu, Z.-R. (2006). Effect of size and charge on pharmacokinetics and in vivo MRI contrast enhancement of biodegradable polydisulfide Gd (III) complexes. *Journal of Controlled Release*, *112*(3), 350–356.

Chapter 3 - Characterization of Intrinsic Magnetic Properties by Multiparameter Dark Field Imaging Velocimetry

Abstract

Magnetic particle characterization determines the quality of the magnetic particles and is of great importance in particle technology, drug delivery, cell separation, in vivo diagnostics and other biomedical applications. The particle size uniformity and colloidal stability of paramagnetic particles have been the focus of most producers, but magnetization is never specified and is typically mentioned only in terms of percent iron oxide content. Bulk measurements of magnetic susceptibility and saturation magnetization, using a SQUID or a Vibrating Sample Magnetometer (VSM), provide an average value at best and do not account for the distributed nature of these variables or for particles with zero or very low susceptibility and magnetization. By means of particle tracking velocimetry in dark field illumination we measured multiple characteristics of several thousand individual micron-sized particles per sample. A commercial particle tracking velocimeter was used to record and captures dark-field images of particle trajectories in an applied isodynamic magnetic field. It instantaneously records and reports particle size and magnetophoretic mobility within a total of twenty-six different characteristics of each magnetic bead imaged. Magnetophoretic mobility and diameter of the particles are the important parameters for estimating the intrinsic magnetic properties of single particles using velocimetry. As the dark field images overestimate the size of the particle, there is a need to calibrate the instrument and find the relationship between the instrument-reported diameter and the actual particle diameter. In the present study, the size calibration capability of the instrument was extended with twenty-one different calibration beads by using transmission electron microscopy to validate the particle size reported by different vendors and thus enabling the estimation of intrinsic magnetic properties,

namely apparent magnetic susceptibility and saturation magnetization, of individual particles. The intrinsic magnetic properties of the magnetic beads estimated by both the velocimeter and Vibrating Sample Magnetometer (VSM) are in good agreement. It was found that estimation of the magnetophoretic mobility distributions and intrinsic magnetic properties of magnetic microparticles using dark-field particle tracking allows economical and time-efficient magnetic evaluation of a broad range of magnetic particle sizes.

Keywords: magnetic instruments, magnetic particle characterization, particle size distribution, magnetophoretic mobility, magnetic susceptibility, saturation magnetization, velocimetry.

3.1 Introduction

Magnetic-particle reagents have been extensively used in the magnetic sorting of labeled cells (Williams et al., 1999; Zborowski & Chalmers, 2011), drug delivery and targeting, magnetic resonance imaging (Chertok et al., 2008; Eberbeck et al., 2011), hyperthermia (Goya et al., 2008; Tay et al., 2018), cellular endocytosis studies (Gupta & Gupta, 2005; Hanot et al., 2015; Jie et al., 2010; Jing et al., 2008; Zhou et al., 2017, 2018), bio-separation and engineering (Harrison et al., 2015), biological pathogen detection (Sullivan & Prorok, 2015), biochemical analysis and other biomedical applications. The particle size and intrinsic magnetic properties play a prominent role in describing the quality of the sample (Paper et al., 1995). Different methods and devices have been recognized previously to characterize the bulk average properties of the magnetic particles such as particle size determination by Dynamic Light Scattering (DLS) (Lim et al., 2013), observation of the particle microstructure by Scanning Electron Microscopy (SEM) (Gherca et al., 2012), Transmission Electron Microscopy (TEM) (Li et al., 2012), Atomic Force Microscopy (AFM) (Lacava et al., 2000), Magnetic force microscopy (Cordova et al., 2017), DynoMag AC susceptometer (Ludwig et al., 2017), determination of the elemental composition and crystalline

phase information by X-Ray diffraction (XRD) (Popa et al., 2003; Tadic et al., 2014; Zhao et al., 2000) and energy dispersive X-Ray spectrometer (EDX) (Sun et al., 2000; Tarasov et al., 2008). Magnetic susceptibility measurement by Superconducting quantum interference device (SQUID) (Granata & Vettoliere, 2016; Hurt et al., 2013), Vibrating sample magnetometer (VSM) (Liao et al., 2018), Faraday microbalance (Laachir et al., 1991), Guoy's scale (Marcon & Ostanina, 2012), torque meter (Kligfield et al., 1981), The Bartington Magnetic Susceptibility System sensors (Dearing, 1999), magnetic magnetoresistance sensors (Little et al., 2013) and modified magnetization curves (Liu et al., 2009). These methods estimate either bulk average particle size or bulk average magnetic susceptibility of the samples. The characterization of intrinsic magnetic properties on a particle by particle basis can be achieved by simultaneous assessment of both the particle size and the magnetophoretic mobility (Chalmers et al., 1999; Sannidhi et al., 2019; Xu et al., 2012; Zborowski, Chalmers, et al., 1999; Zborowski & Chalmers, 2011).

Magnetophoretic mobility which defines the key property of the magnetic particles depends on the particle size, magnetic susceptibility and viscosity of the medium. Particle tracking velocimetry has been utilized to measure magnetophoretic mobility which has been used in quantification and separation of magnetically labeled cells (Mccloskey et al., 2003; McCloskey et al., 2000, 2001; Watarai & Namba, 2002; Williams et al., 1999; Yu et al., 2010) and in developing the continuous quadrupole magnetic sorter (Sajja et al., 2011; Weegman et al., 2016; Zborowski, Sun, et al., 1999). Similar and new methodologies have been employed to estimate the magnetophoretic mobility and susceptibility of single magnetic particles (Grob et al., 2018; Maldonado-Camargo et al., 2017; Wise et al., 2015). Magnetophoretic mobility is independent of the applied magnetic field (H) for paramagnetic species. The determination of intrinsic magnetic properties (apparent susceptibility and/or saturation magnetization) depends on simultaneous

knowledge of the mobility and size of each particle. In one approach the ratio of magnetically induced velocity to the settling velocity has been used to calculate the saturation magnetization, thereby eliminating particle size from the susceptibility equation (Jin et al., 2008). In another approach cell tracking velocimetry and modified susceptibility solutions were applied to measure volumetric magnetic susceptibility of polystyrene beads labeled with magnetic nanoparticles (Zhang et al., 2005). Sedimentation velocity depends on, in addition to particle size, particle density, solution density and viscosity so that its substitution for particle size is not always possible. In the current work, the diameter of every particle is measured along with its magnetophoretic mobility thereby providing a particle-by-particle evaluation of apparent magnetic susceptibility and saturation magnetization.

Hyperflux™ velocimeter is an instrument used to measure the particle count, magnetophoretic mobility and particle size distribution on a particle by particle basis of magnetic particles and magnetically labeled cells. This instrument is also used in quantitative cell analysis as a surrogate for Fluorescence Activated Cell Sorters (FACS) (Zhou et al., 2017) and in quantifying nanoparticle endocytosis (Zhou et al., 2018). The size calibration of the instrument is critical in determining the exact particle diameter of the sample as the dark field imaging technique over-estimates the particle size based on image pixel size (Sannidhi et al., 2018, Sannidhi et al., 2019; Zhou et al., 2016).

The objective of accurate single-particle diameter measurement by the velocimeter instrument was to enable the determination of intrinsic magnetic properties of individual particles -- a multiparameter approach as is used in flow and image cytometry. The calibration of the instrument is done by the validation of instrument reported diameter and vendor reported diameter.

Several de-identified commercial bead samples were used to interpret the particle size and intrinsic magnetic property distributions which varied among the different vendors.

3.2 Theory

Magnetophoresis is used to estimate the magnetophoretic mobility of particles which helps in quantifying labeled cells, for example (Chalmers et al., 1999; Zborowski, Chalmers, et al., 1999; Zborowski & Chalmers, 2011). The force balance on a spherical particle in an isodynamic magnetic field and viscous medium gives the terminal velocity (v) attained by the particle, as

$$v = \frac{D^2 \Delta\chi}{18\eta} . \nabla \left(\frac{B_o^2}{2\mu_o} \right) \tag{3-1}$$

The first term of the equation (3-1) represents the properties of the particle and fluid medium and the second term is the gradient of the magnetic field energy. Magnetophoretic mobility of magnetic beads is defined as the ratio of field-induced bead velocity (dimensions of m/s) to the magnetic field body force (N/m^3) exerted on the free space displaced by the bead so that its dimension is m^4/N.s, equal to m^3/T.A.s. Magnetophoretic mobility U_m of magnetic beads as a function of diameter of the particle D and the difference of magnetic volume susceptibility $\Delta\chi$ between particle and fluid medium is given by

$$U_m = \frac{D^2 \Delta\chi}{18\eta} \tag{3-2}$$

The difference in susceptibility ($\Delta\chi$) is approximated to the volume susceptibility of the particle χ_p, while the susceptibility of the fluid medium, distilled water, is negligible. η is the viscosity of distilled water.

By estimating the particle size and magnetophoretic mobility simultaneously in the medium of known viscosity, the magnetic susceptibility of every single particle can be calculated (Chalmers et al., 1999; Gibson, 1936; Reddy et al., 1996; Xu et al., 2012; Zborowski & Chalmers,

2011). In most practical cases, the difference in magnetic susceptibility is approximated to the susceptibility of the particle. The susceptibility value given by the Hyperflux instrument is measured at an applied field of 0.56 Tesla which lies in the saturated region of the magnetization curve (Sannidhi et al., 2019), thus giving the equation for *apparent* magnetic susceptibility of the particle, (χ_{app}) as

$$\chi_{app} = \frac{18\eta U_m}{D^2} \tag{3-3}$$

where *apparent magnetic susceptibility* is defined as the slope of a straight line on the *M* vs. *H* curve (Figure 3.7) between the origin and the applied magnetic field B_o. Thus, χ_{app} is the variable that determines magnetophoretic mobility at any level of the applied field and is always less than the initial susceptibility (defined as the slope of the *M* vs. *H* curve at the origin, $\chi_{in} = M/H$).

The intrinsic saturation magnetization of the particle, M_s in terms of magnetophoretic mobility, size of the bead, intensity of the applied magnetic field and the viscosity of fluid medium is given by

$$M_s = \chi_{app} H = \frac{18\eta U_m B_o}{D^2 \mu_o} \tag{3-4}$$

Where *H* is the applied magnetic field strength, B_o is the local magnetic flux density of permanent magnet and μ_o is the permeability of free space. The magnetic field forms a gradient in an isodynamic field region where the product of $B.\nabla B$ is constant. Equations 3-3 and 3-4 were used to estimate the intrinsic magnetic properties of several thousand individual micron sized composite magnetic particles per sample.

3.3 Materials and Methods

3.3.1 Calibration beads

Twenty-one calibration beads which include both magnetic and non-magnetic beads with different vendor specified diameters were used in this study. Sixteen different magnetic beads (designated P1 – P16) having the size (diameter) range from 0.68 to 5.01 micrometers and five different non-magnetic beads (designated P17-P21) ranging from 0.43 to 4.99 micrometers in diameter were studied. Table 3.1 shows the list of different beads (both magnetic and non-magnetic beads) along with their vendor diameter, instrument reported mean diameter, calculated filtered mean diameter and the TEM mean diameter with their standard deviations as determined in this study (see below).

Three additional magnetic bead samples, i.e., commercial Estapor magnetic beads designated N2, N4, (obtained from Merck Chimie SAS (Estapor 2018) and Dynabeads (N16) (procured from Thermofisher, USA) listed in Table 3.4 were added to study intrinsic magnetic properties vs. % iron oxides bringing to six the number of samples for which vendors had provided % iron oxides for the data used in Figure 3.9.

3.3.2 Hyperflux™ velocimeter

The *Hyperflux™ velocimeter* (Magnaquant, Louisville, KY, USA) is an instrument which captures the dark field images of several thousand tracks of the particles passed through a glass channel cell, thus analyzing twenty-six different characteristics of the magnetic particles (Figure 3.1) (Sannidhi et al., 2019; Zhou et al., 2016) which include particle size, magnetophoretic mobility, intensity and others. Image data from every experiment conducted by the velocimeter are stored and can be replayed and studied by altering the parameters of interest such as threshold intensity and size gating. The embedded software 'Cytotest' analyzes the image data within

seconds and tabulates the characteristics of several thousand particles into a "tracks.csv" spreadsheet. The video of each individual track of the particle can be interactively selected and viewed by the velocimeter's "Magex" software package. The list-mode spreadsheet variables used to determine "raw" dark-field particle diameters in this study were "tAvgIntensity" (gray-scale intensity between 0 – 255, higher being brighter) and "tAvgSize" (the number of pixels in the dark-field image of the particle). These are used as filters to select legitimate values of "tAvgSphereDiameter" (a circle-equivalent diameter calculated algorithmically from pixel occupancy). The "Avg" designation means that the value was averaged over measurements made in every video frame in which the given particle was present (the spreadsheet also reports the standard deviation of each such average).

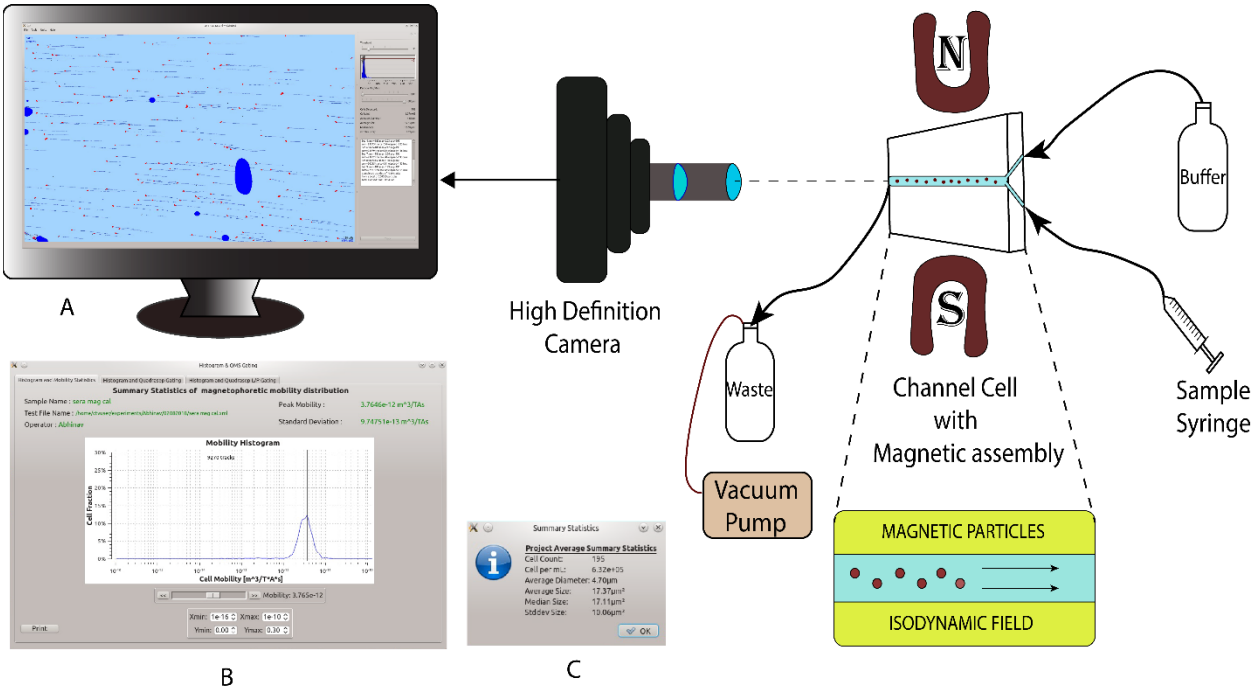

Figure 3.1 - Schematic representation of the Hyperflux™ velocimeter with particle trajectories A, magnetophoretic mobility histogram of the sample B and the summary statistics C.

3.3.3 Transmission Electron Microscopy (TEM)

A Zeiss EM 10 Transmission Electron Microscope (TEM) operating at 60 KV was used to capture the images of the beads. A suspension of beads of about 5 to 10 μL was deposited and air dried on copper grids with formvar/carbon film- 300 mesh size (Catalog No: FCF300-CU) obtained from Electron Microscopy Sciences (Hatfield, PA, USA).

3.3.4 Vibrating Sample Magnetometer (VSM)

The *Physical Property Measurement System* (PPMS) Dynacool instrument of Quantum Design (San Diego, CA) was used to measure the bulk average magnetization and susceptibility of the dried samples of each type. The sample measurements require 90 to 120 minutes of run-time to perform a magnetization curve based on the specified sweep rate of the applied magnetic field and temperature conditions.

3.4 Procedure

3.4.1 Velocimetry

The magnetic particle samples were diluted to a concentration of about 10^4 to 10^5 particles/mL (volume fraction of about 10^{-8} to 10^{-6}) to avoid particle track interference while tracking. Usually, the instrument requires a sample volume up to 3 mL to characterize and estimate the average properties of the beads over 10 sets by refreshing the sample in the region of interest within the sample cell. Each data "set" takes about 2 seconds at a rate of 30 frames per second. Overall, the instrument captures 600 frames of a sample in one typical experiment. The parameters such as the number of frames per second (fps), number of sets per experiment can be altered in the graphical user interface of the software before starting the experiment. The image acquisition takes about 20 seconds for 10 sets, and the intensity threshold limit selection, auto-selection of the screen apart from the exclusion zones of the screen, tracking the trajectories of individual particles

take about 30 to 45 seconds (Zhou et al., 2016, 2017). The embedded software generates a .csv file with 23 different characteristics of the particles on a particle-by-particle basis which also includes the magnetophoretic mobility histogram. Individual bead diameters were calculated from dark-field image size using a calibration-based algorithm (Zhou et al., 2016). By considering the relationships between magnetophoretic mobility and intrinsic magnetic properties (equations 3-3 and 3-4), apparent volume susceptibility and saturation magnetization of the selected beads were calculated and summarized in this chapter. The temperature dependency of magnetic particle characterization by velocimeter and the precautionary measures of velocimeter operation are given in Appendix A and Appendix B of this dissertation.

3.4.2 VSM

Each dried sample was weighed (usually requiring 10-20 mg for optimum results) before inserting the sample into the chamber. After updating the required maximum magnetic field intensity and temperature settings based on the sweep rate of 0.001 Tesla/second it takes around 2 hours for the generation of a complete hysteresis loop.

3.4.3 Data analysis

Video image analysis was performed by the Hyperflux velocimeter software package Cytotest^{TM}, which creates a 26-parameter list-mode spreadsheet titled “tracks.csv”, from permanently recorded video frames. These spreadsheet data were used in fitting linear and quadratic functions described below and calculating means and standard deviations using spreadsheet packages such as Microsoft Excel^{TM}. Particle size distributions, means and standard deviations were derived from TEM images using ImageJ^{TM}.

3.5 Results and Discussion

3.5.1 Magnetophoretic Mobility

The magnetophoretic mobility of each particle of the sample was estimated by Hyperflux velocimeter in pRm (pRm is defined as pico Rembaum, where 1 pRm = 10^{-12} m^3/T.A.s, honoring the units in the name of Alan Rembaum for his pioneering work on magnetophoretic mobility and cell sorting apparatus (Rembaum, 1984; Yen et al., 1980) in the early 1980's.

3.5.2 Diameter data validation

The following two forms of data validation were used to interpret the actual particle diameter from the dark field images in order to calibrate the instrument.

3.5.2.1 Validation of the raw diameter values from the velocimeter

Three main methods were used to confirm the validity of the raw diameter values obtained from dark-field images before calibration. First, the value returned automatically in the Hyperflux display by the Cytotest software given as "Instrument reported average diameter" in Table 3.1, which comprises filtered values based on intensity thresholds and size limits for reporting automatically on a user-friendly standard format. Second, the value determined by visual inspection of the raw particle diameter histograms. The visual analysis of the raw particle size histograms always revealed a major peak at or near the actual mean diameter value in the cases of all particles. This is considered a "modal" value and is not included in Table 3.1. Third, the calculation of actual mean diameter by filtering raw data according to intensity threshold and size limits.

Table 3.1 - Vendor diameter, instrument reported average diameter, calculated filtered mean diameter and TEM mean diameter of 21 different particles. SD represents standard deviation of the average diameter values.

Particle Name	Vendor Diameter (micrometers)	Instrument reported average diameter (micrometers)	Calculated filtered mean diameter (micrometers)	SD	TEM mean diameter (micrometers)	SD
MAGNETIC BEADS						
P1	0.68	4.48	3.4	0.05	0.5	0.135
P2	0.7	4.16	3.36	0.073	0.4	0.08
P3	0.87	5.73	3.66	0.087	1	0.2
P4	0.96	5.07	3.41	0.045	0.85	0.017
P5	1	4.48	3.51	0.083	0.9	0.28
P6	1	3.64	3.32	0.066	1	0.11
P7	1.1	5.68	4.92	0.055	1.5	0.18
P8	2.39	9.72	6.45	0.22	2.35	0.051
P9	2.6	10.63	7.26	0.113	2.7	0.058
P10	2.7	8.11	5.63	0.128	2.28	0.049
P11	2.7	9.03	5.08	0.074	1.43	0.068
P12	3	10.16	5.52	0.062	2.8	0.054
P13	3.12	7.1	9.72	0.22	3.18	0.125
P14	3.13	9.74	8.93	0.098	3	0.091
P15	3.27	10.92	7.43	0.07	3	0.076
P16	5.01	4.8	14.99	0.257	4.9	0.14
NON-MAGNETIC BEADS						
P17	0.43	3.78	2.55	0.015	0.44	0.18
P18	2.01	9.31	5.81	0.04	1.9	0.04
P19	2.9	11.4	7.56	0.044	3	0.038
P20	4.8	15.62	12.91	0.1316	4.5	0.058
P21	4.993	15.27	13.03	0.312	5	0.043

In this method, the raw data given by the tracks.csv spreadsheet is sorted by two parameters namely, “tAvgIntensity” (the average intensity along the individual track of the particle given by the dark field image) and “tAvgSize” (representing the average size based on pixel count of the individual particle blob within the entire track of the individual particle). The parameter “tAvgIntensity” is filtered to include all the data points with an average intensity greater than 35 gray-scale units. The parameter ‘tAvgSize’ is filtered to include the data points between 5 and 300 squared pixels for the beads with vendor diameter less than 2.6 micrometers, the upper limit of tAvgSize parameter is 600 squared pixels for beads with vendor diameter greater than 2.6 micrometers.

3.5.2.2 Validation of vendor reported diameters

The diameter values reported by different vendors were justified by the mean diameter values estimated from the TEM captured images as shown in Figure 3.2. These images were made

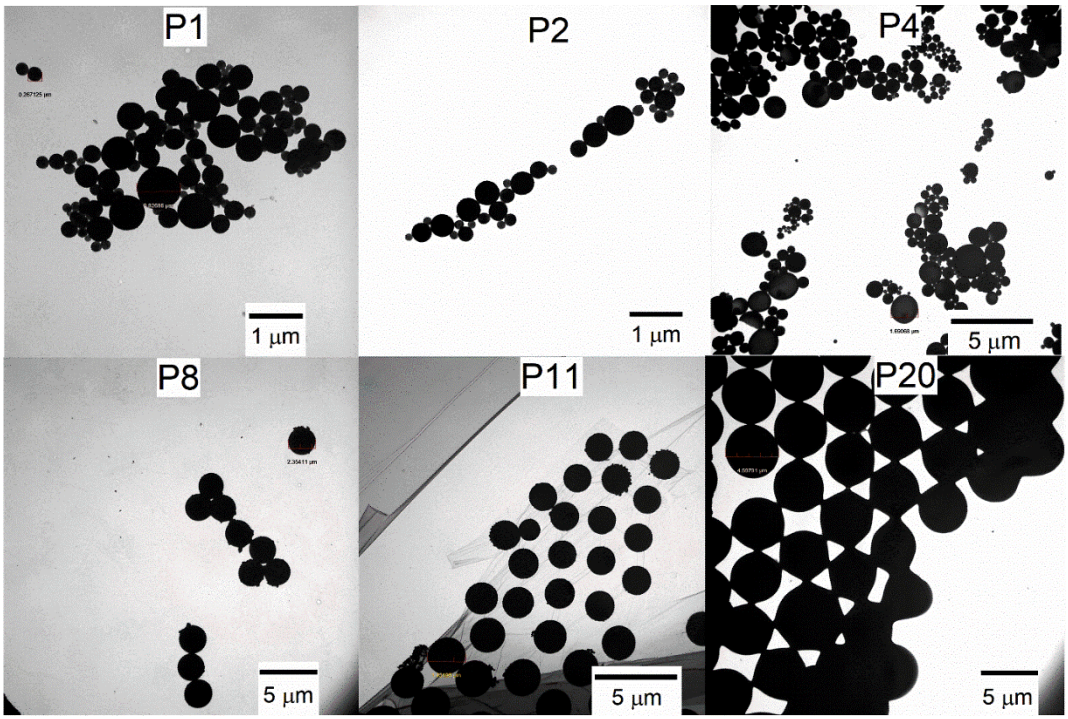

Figure 3.2 - TEM Images of the beads P1, P2, P4, P8, P11 and P20 covering the full range of the commercial particle sizes.

with "raw" samples, not magnetically selected before preparing for electron microscopy, as velocimeter data were also obtained using raw samples. (Many, if not all, vendors recommend a magnetic purification step before using their beads for labeling or as reagents). The diameters are reported in the last two columns of Table 3.1 and most of them are confirmatory of the vendor diameters (second column of Table 3.1 and Figure 3.3 (D)).

3.5.3 Diameter Calibration curves

The data of Table 3.1 were used to construct diameter calibration curves for the Hyperflux velocimeter following the examples of (Zhou et al., 2016, 2018). The calibration curves of the instrument shown in Figure 3.3 illustrates the relationship among different diameters reported in Table 3.1. The calibration plots shown in Figures 3.3 (A) and 3.3 (B) between "Calculated filtered mean diameter" and "Vendor diameter" are compared to show the small effect of two outlying data of P11 and P12 beads (possibly related to vendor statements), with the slope and intercept agreeing at better than two decimal places and acceptable goodness of fit (R^2) values. As expected, based on the use of dark-field illumination, instrument calculated filtered mean diameter is always greater than the true diameter, whether given by vendor or determined by TEM. The relationship between the TEM mean diameter and the vendor diameter is given by the linear curve compared with the expected y = x dotted line as shown in Figure 3.3 (D). The linear curve fit parameters of the calibration curves along with standard deviations and goodness of fit values are given in Table 3.2.

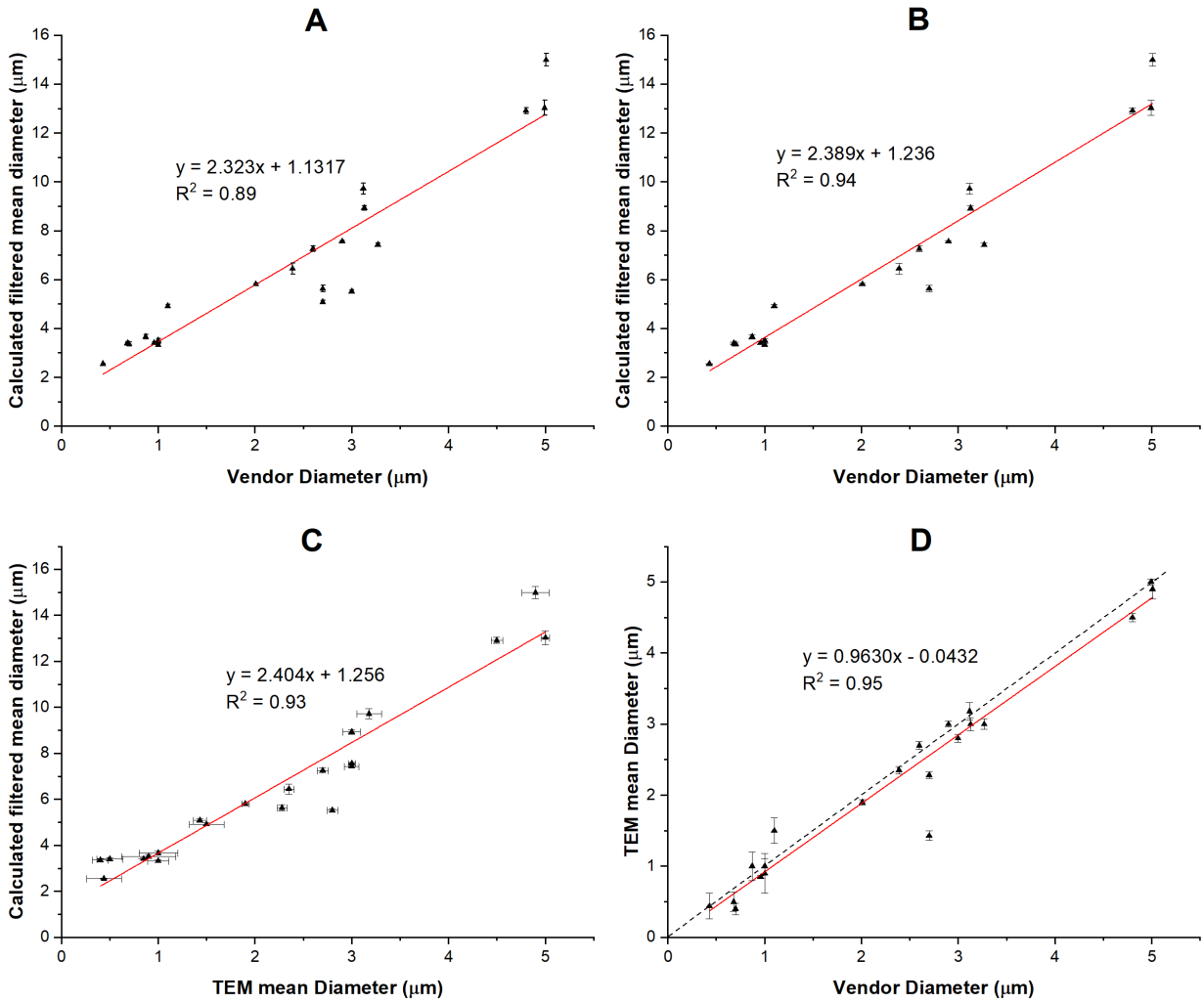

Figure 3.3 - Calibration curves with linear fits: **(A)** Calculated filtered mean diameter vs Vendor diameter; **(B)** Calculated filtered mean diameter vs Vendor diameter without outlier samples P11 and P12; **(C)** Calculated filtered mean diameter vs TEM mean diameter; **(D)** TEM mean diameter vs Vendor diameter.

Table 3.2 - Calibration curve parameters with standard deviations and R^2 values of the curves fitted to the plots given in Figure 3.3.

Calibration graph type	Linear curve fit parameters, y=mx+c		
	Slope	Intercept	R^2
Calculated filtered mean diameter vs Vendor diameter	2.323 ± 0.1856	1.1317 ± 0.5088	0.89
Calculated filtered mean diameter vs Vendor diameter (without outliers P11 and P12)	2.389 ± 0.1405	1.236 ± 0.3835	0.94
Calculated filtered mean diameter vs TEM mean diameter	2.404 ± 0.1510	1.256 ± 0.3959	0.93
TEM mean diameter vs Vendor diameter	0.9630 ± 0.0497	-0.0432 ± 0.1364	0.95

3.5.4 Intrinsic Magnetic Properties

Intrinsic magnetic properties of the magnetic particles such as magnetic volume susceptibility and saturation magnetization are vital in knowing the quality of the sample. In this study, the shape of the particles is assumed to be spherical. After calculating the actual diameter of each particle based on the generated calibration curves of the velocimeter instrument, the raw data from .csv files were subjected to data filters to generate the intrinsic magnetic properties such as apparent volume susceptibility and saturation magnetization of the individual particles.

3.5.4.1 Apparent magnetic susceptibility distribution

The apparent volume susceptibility of magnetic particles is inversely related to the applied field (B) when particles undergo saturation magnetization as shown in Figure 3.7. The work by Jin et al. presents magnetization, *M* vs. *B* and shows, as expected, saturation (Jin et al., 2008). In this present study, the used induction value of 0.56 T is in the saturation range for all the beads

(Figure 3.7 and ref. (Zhou et al., 2016)), so susceptibility, which is the slope of *M* vs. *B*, will be lower than the initial slope, χ_{in}, of the curve in the range where *M* increases linearly, up to a certain value less than 0.1 T. The intrinsic magnetic properties of the beads, the average apparent volume susceptibility and average saturation magnetization estimated by the velocimeter were in good agreement with those measured by bulk average method using Vibrating Sample Magnetometry (VSM) (Sannidhi et al., 2019). The apparent magnetic susceptibility of the individual magnetic particles are calculated based on the relationship between susceptibility and magnetophoretic mobility (equation 3.3) using the actual diameter calculated from the linear curve equation of calibration plot 'Calculated filtered mean diameter vs Vendor diameter' (given in Table 3.2) and assuming the viscosity of the medium (distilled water) to be 0.001 Pa s (Pascal-second). An example of the histograms of the two calculated parameters is given for the P15 beads in Figure 3.4, where the solid vertical line in the upper panel (Figure 3.4 (A)) denotes the vendor diameter, which is near the major peak bin of the size histogram. The log-scale histogram of apparent susceptibility is given in the lower panel. The 2-parameter apparent susceptibility vs actual diameter distributions for all the beads is shown in Figure 3.5, where the vertical solid line represents the vendor reported diameter and the horizontal dotted line corresponds to the mean apparent magnetic susceptibility. The apparent susceptibility is inversely proportional to the square of the diameter ($\chi_{app}\ \alpha\ 1/D^2$) theoretically given by equation 3-3, which agrees with the experimental values reported in Figure 3.5. The experimental 2- parameter plots between- 'Apparent volume susceptibility vs Actual diameter' are fitted by the model equation, $y = A + B/x^2$. Table 3.3 provides the curve fitting parameters of the model equation for all the sixteen beads. The apparent volume susceptibility is directly proportional to the percent iron oxides present in the beads (Figure 3.9).

Table 3.3 - Mean apparent susceptibility and mean saturation magnetization for all the 16 magnetic beads. Apparent volume susceptibility vs calculated diameter with the fitted curve parameters of the model equation, $y = A + B/x^2$, underscored tabs represent the curves with $R^2 > 0.8$.

Particle Name	Vendor Diameter (micrometers)	Mean apparent susceptibility χ_{app} (SI)	Mean saturation magnetization M_{sat} (kA/m)	Apparent Volume Susceptibility (SI) vs Calculated Diameter (micrometers) Model Equation: $y = A + B/x^2$		
				A	B	R^2
P1	0.68	0.218	97.272	0.0167 ± 0.0028	0.0558 ± 0.0012	0.63
P2	0.7	0.230	104.250	0.0302 ± 0.0056	0.0449 ± 0.0023	0.49
P3	0.87	0.282	126.101	0.0349 ± 0.0091	0.1189 ± 0.0038	0.64
P4	0.96	0.097	43.356	0.0123 ± 0.0012	0.0388 ± 0.0004	0.84
P5	1	0.12	53.853	0.0260 ± 0.0053	0.0573 ± 0.0031	0.57
P6	1	0.203	90.865	0.0259 ± 0.0053	0.0557 ± 0.0023	0.53
P7	1.1	0.121	53.951	0.0155 ± 0.0029	0.0817 ± 0.0015	0.66
P8	2.39	0.027	12.349	0.0016 ± 0.0059	0.0962 ± 0.0047	0.89
P9	2.6	0.083	37.098	0.0246 ± 0.0075	0.0860 ± 0.0045	0.63
P10	2.7	0.071	32.033	0.0341 ± 0.0043	0.0359 ± 0.0035	0.18
P11	2.7	0.239	106.688	0.0129 ± 0.0040	0.1984 ± 0.0027	0.85
P12	3	0.13	58.027	0.0093 ± 0.0020	0.1433 ± 0.0016	0.84
P13	3.12	0.029	12.934	0.0205 ± 0.0057	0.0403 ± 0.0036	0.27
P14	3.13	0.146	65.450	0.0291 ± 0.0034	0.1785 ± 0.0025	0.84
P15	3.27	0.050	23.501	0.0183 ± 0.0014	0.1203 ± 0.0013	0.81
P16	5.01	0.020	8.920	0.0088 ± 0.0008	0.1808 ± 0.0134	0.50

In Table 3.3 it is seen that two-parameter data from several bead samples show a poor fit to the $1/D^2$ rule of equation 3.3. Inspection of the two-parameter displays of Figure 3.5 reveals points quite distant, most of them below, the fitted curve. All the data were obtained using

untreated samples of beads as received. Most vendors recommend pre-treatment of bead samples by qualitative magnetic selection before use as reagents for labeling or capturing experiments. This is typically done by holding an external magnet of unknown strength against the external wall of the vessel containing the sample for a specified length of time and then decanting all particles not trapped by the external magnet. Thus, the distributions shown in this work are for "raw" samples prior to any magnetic selection. Many of the samples have mean apparent volumetric susceptibility rather close to 0.1. Smaller beads are consistently above this level and larger beads below. The reason is apparent in Figure 3.9, where smaller beads have a higher per cent iron oxides and vice versa.

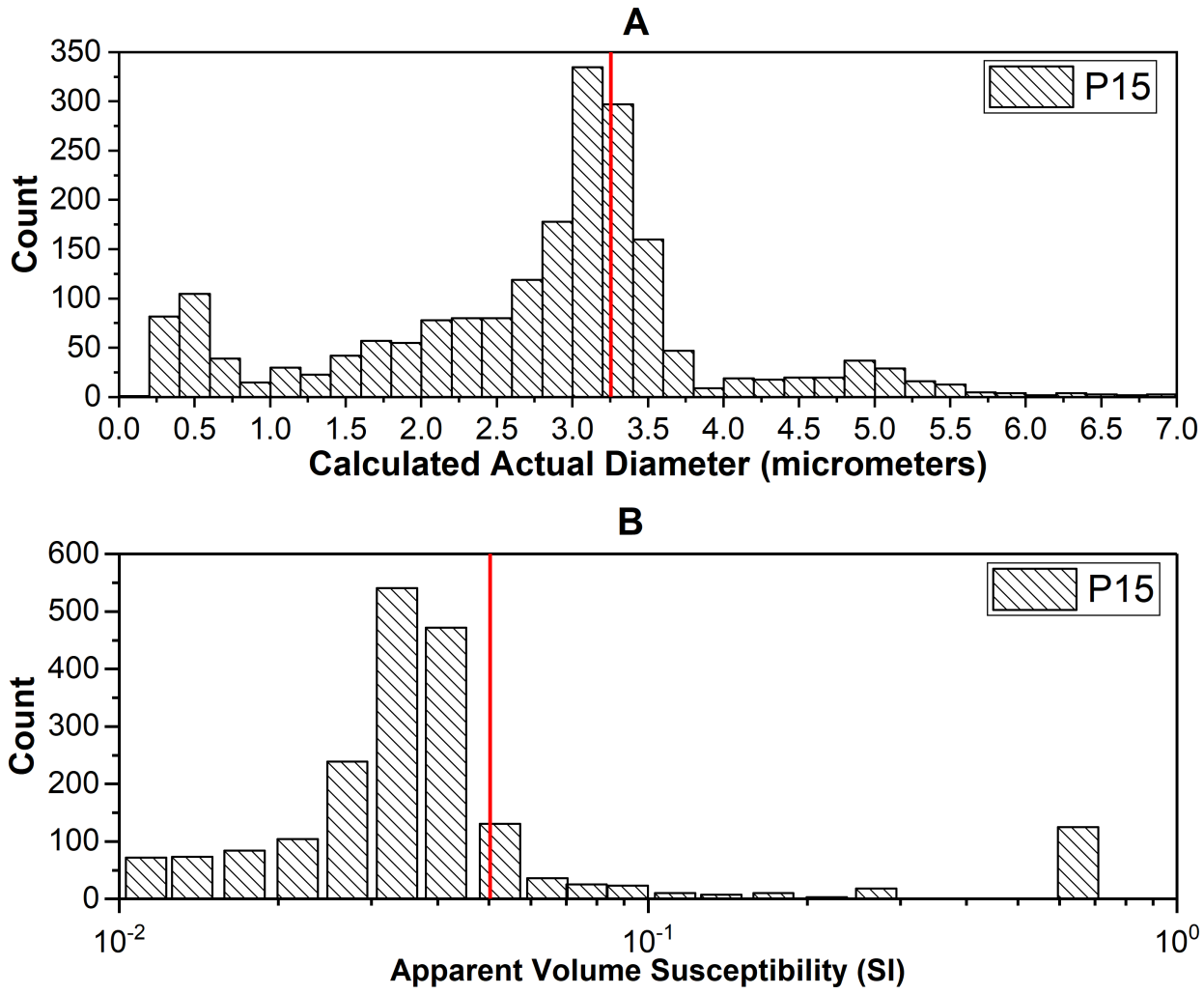

Figure 3.4 - Actual diameter and apparent volume susceptibility histograms of P15 beads. **(A)** The solid vertical line in the top panel represents the vendor reported diameter. Actual Diameter of each bead is calculated from the linear calibration curve between "Calculated filtered mean diameter vs Vendor diameter" as shown in Figure 3.3 (B). Populations of particle doublets and debris particles (which are also found in distilled water used as a diluent) are evident. **(B)** The solid vertical line in the bottom panel corresponds to the calculated mean apparent susceptibility, which is above the mode due to small numbers of very high (small diameter) susceptibility beads represented by the cumulative bar at $\chi_{app} = 0.6$.

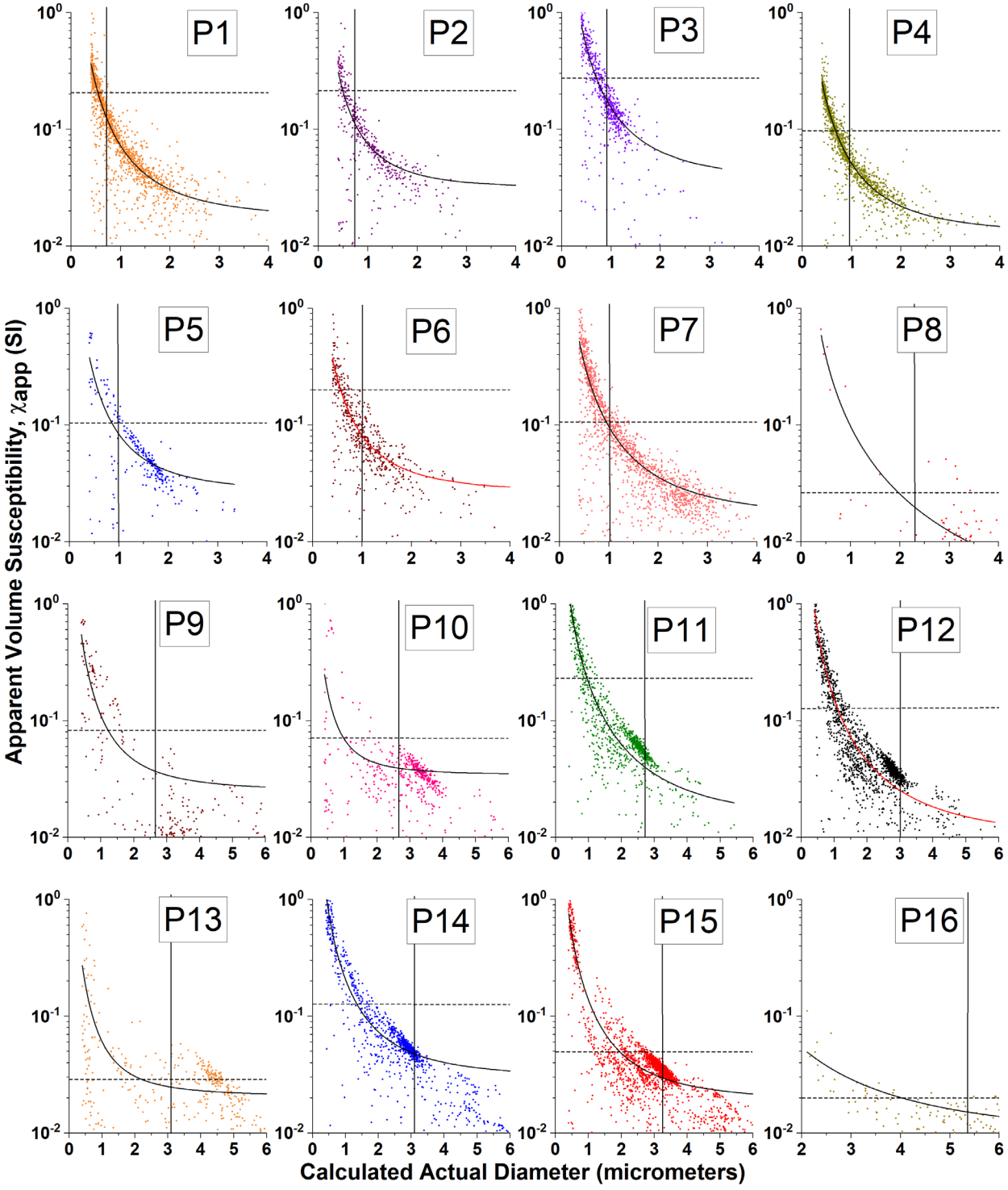

Figure 3.5 - Apparent Volume Susceptibility vs Calculated actual diameter for 16 different magnetic beads, with curve fitting $1/D^2$ (Using filter χ_{app}> 0.01 for all the beads and actual diameter>2 µm for P16 beads only; here each "Calculated Actual Diameter" is estimated by using the calibration curve between "Calculated filtered mean diameter vs Vendor diameter" as shown in Figure 3.3 (B).

3.5.4.2 Saturation Magnetization

As the applied magnetic field (0.56 T) lies in the saturation region of the magnetization curves of particles, the calculated magnetization using equation 3.4 is named "saturation magnetization". A significant broad distribution of the particles in each sample is evident from the calculated saturation magnetization vs. calculated diameter curves shown in Figure 3.6, where an example of the $1/D^2$ fit is shown for particles P1 ($R^2 = 0.63$). In all cases some counts of non-magnetic debris are seen below the $1/D^2$ curve. The experimental data are consistent with the equation which determines the saturation magnetization of the beads as inversely proportional to the square of the diameter ($M_s \propto 1/D^2$).

The bulk average intrinsic magnetic properties of selected magnetic beads were estimated by VSM Dynacool instrument, Quantum Design. Figure 3.7 summarizes the magnetization curves from which initial volume susceptibility of the beads (χ_{in}) which is the slope of the hysteresis curve near the origin, the apparent volume susceptibility (χ_{app}) which is the slope of the line from origin to the corresponding point on the curve at $B_o = 0.56\ T$ and saturation magnetization of the beads (M_{sat}) were determined and entered into Table 3.4.

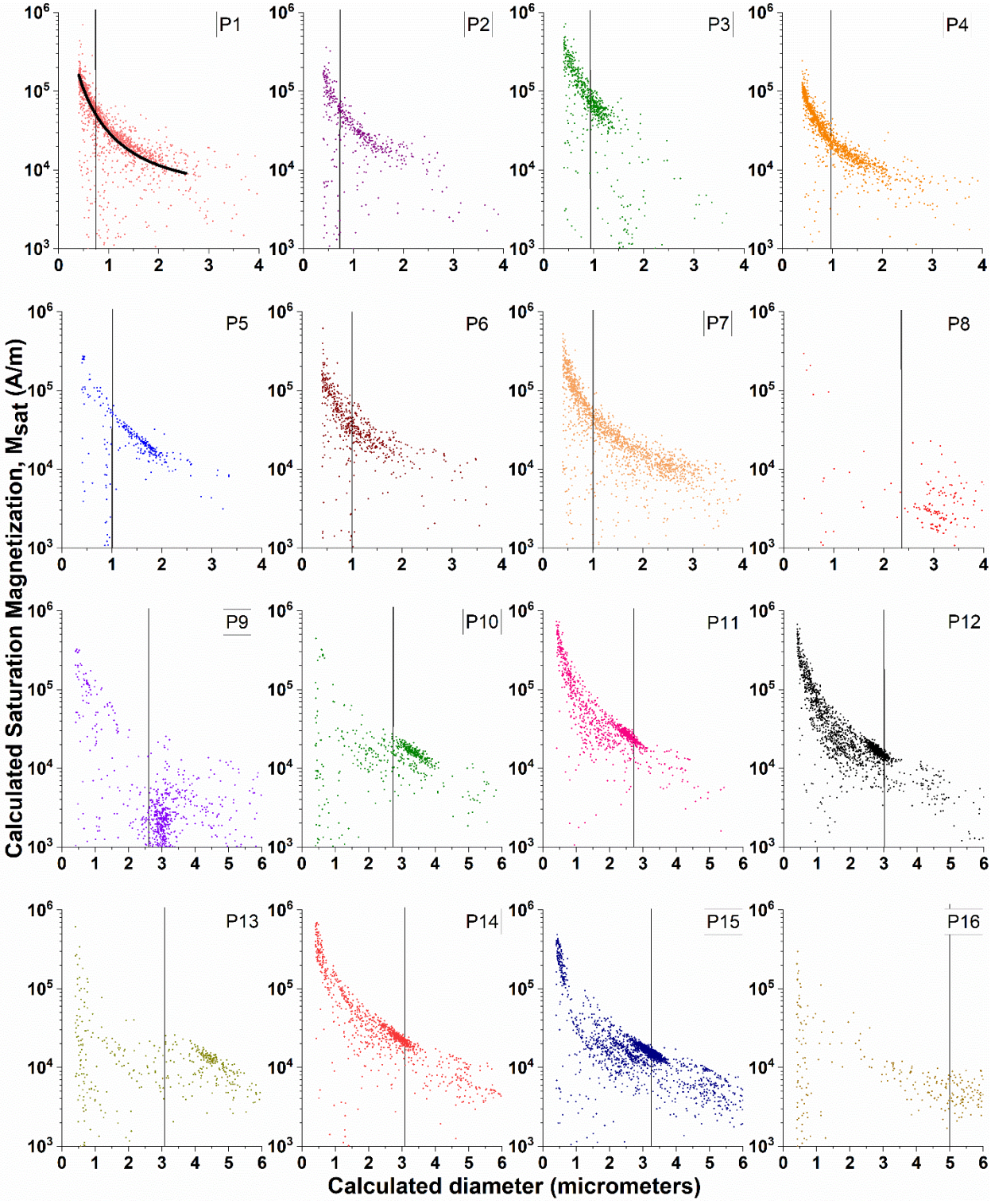

Figure 3.6 - Calculated Saturation Magnetization vs. calculated Diameter (Equation 3-4) for 16 different commercial magnetic beads. The vertical line indicates the diameter specified by the vendor in each case. The solid curve in the P1 data fits the $1/D^2$ function with $R^2 = 0.63$.

3.5.5 Magnetic property comparison between VSM and Hyperflux velocimeter

The applied local flux density of the velocimeter is 0.56 *T*, which is far into the saturation region (usually above about 100 *mT* for magnetic microparticles) (Bronzeau & Pamme, 2008), the susceptibility at this fixed magnetic field is termed "apparent volume susceptibility" in the present research. The saturation magnetization and apparent volume susceptibility of those beads for which sufficient sample material was available are compared between those of VSM and Hyperflux velocimeter and summarized in Table 3.4.

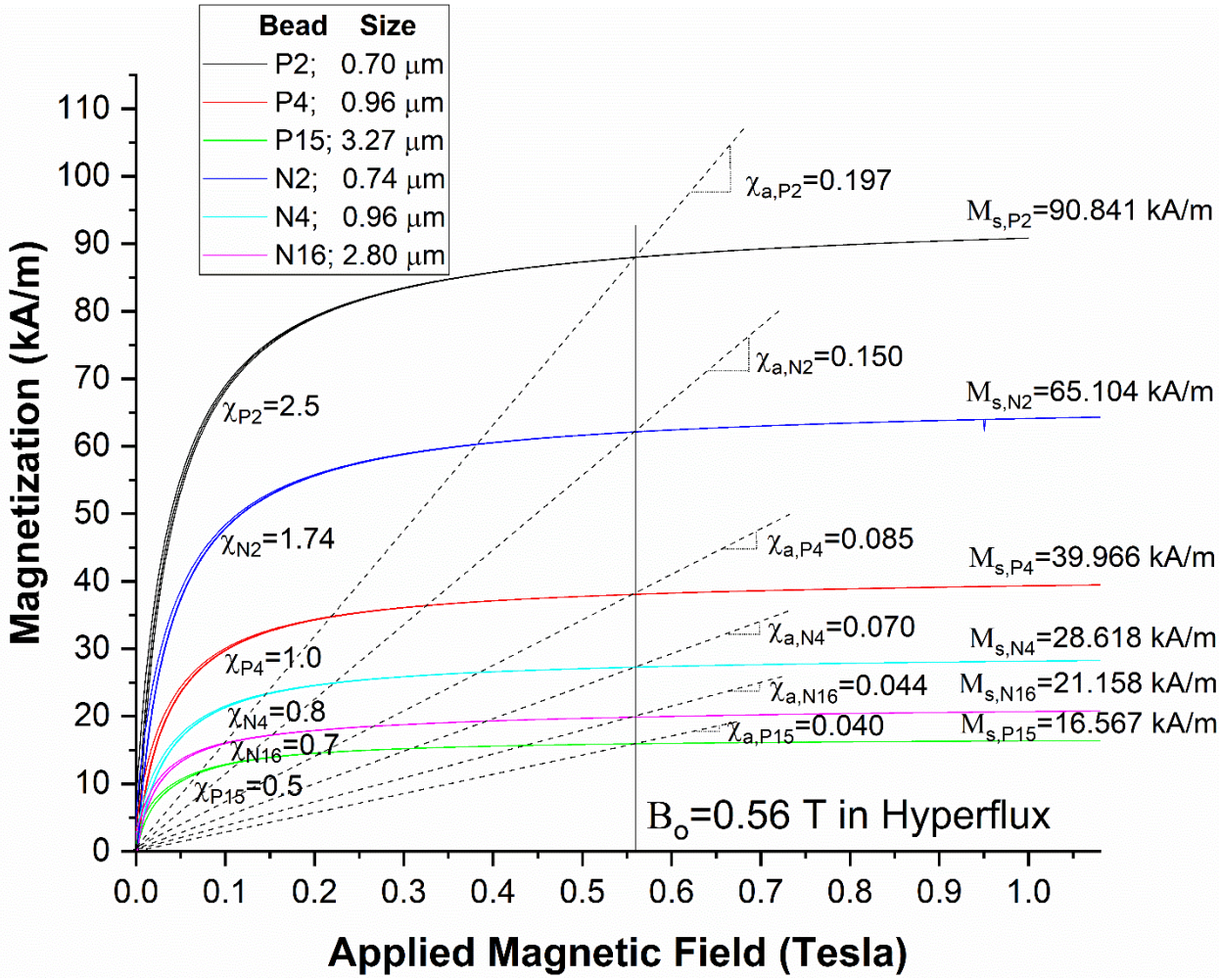

Figure 3.7 - Magnetization curves determined by VSM for 6 different beads. The apparent susceptibility is calculated for a magnetizing field of 0.56 T and is the slope of a straight line between the origin and the 0.56 T point on the magnetization curve.

A similar comparative study has been made previously (Moore et al., 2000), by using four synthesized different PSM microspheres (Jin et al., 2008). Magnetic data comparison is shown in Figure 3.8 where the magnetization of the beads is directly proportional to the percentage of iron oxides contained in the beads. The saturation magnetization of pure iron is reported as $1.7 * 10^6$ *A/m* and the magnetization of ultrafine Fe nanoparticles ranged from 10^5 to 10^6 *A/m* (Gangopadhyay et al., 1992).

Table 3.4 - Intrinsic saturation magnetization and susceptibility comparison between VSM and Hyperflux. For standard deviations see Figure 3.8.

Magnetic Beads Composition			Saturation Magnetization (kA/m)		Volume Susceptibility (SI)		
Bead name	Vendor Size (µm)	Fe Oxides (%)	by VSM	by Hyperflux	Initial χ by VSM	Apparent χ by VSM	Apparent χ by Hyperflux
P2	0.70	41.00	90.841	104.250	2.500	0.197	0.230
N2	0.74	37.50	65.104	76.778	1.740	0.150	0.172
P4	0.96	23.70	39.966	43.356	1.000	0.085	0.097
N4	0.96	23.70	28.618	45.913	0.800	0.070	0.100
P15	3.27	14.00	16.567	23.501	0.500	0.040	0.050
N16	2.80	13.25	21.158	21.633	0.700	0.044	0.048

The magnetic beads used in this study have an iron oxide composition of 13 to 45 percent, so the saturation magnetization of these beads is in the range of 10^4 to 10^5 *A/m,* less than that of pure iron. Only few publications have reported the size, composition and volume magnetization of the beads (Häfeli et al., 2002; Haynes, 2014). The saturation magnetization and apparent volume susceptibility of the samples measured by VSM and Hyperflux were in acceptable agreement. The susceptibility estimated by micro-magnetometry of a single Dynabead of size 2.8 micrometers is 0.65 SI (Sinha et al., 2012). The single particle analysis achieved by this technique gives the magnetic property distributions within each sample (Figure 3.6) and the magnetic

properties measured by velocimeter are always slightly larger than the average results obtained by VSM (Table 3.4) (Sannidhi et al., 2019).

The linear relationships for the results in Figure 3.8 are statistically significant with the coefficient of determination (R^2) values greater than 0.9. The saturation magnetization by VSM given in *emu/g* is converted to *A/m* by the known values of density of the beads from the manufacturers to maintain uniform units for better comparison. Most of the publications in the literature have reported the intrinsic magnetic properties in units of mass, either bulk average mass susceptibility (in m^3/kg) or molar magnetic susceptibility (in m^3/mol) and bulk average saturation magnetization (in *emu/g* or Am^2/kg) (Hunt et al., 1995; Shi et al., 2015); volumetric units were not specified. Intrinsic properties specified in volumetric units and exact compositional information of the beads provide ease for the reader for conversion and comparison of results.

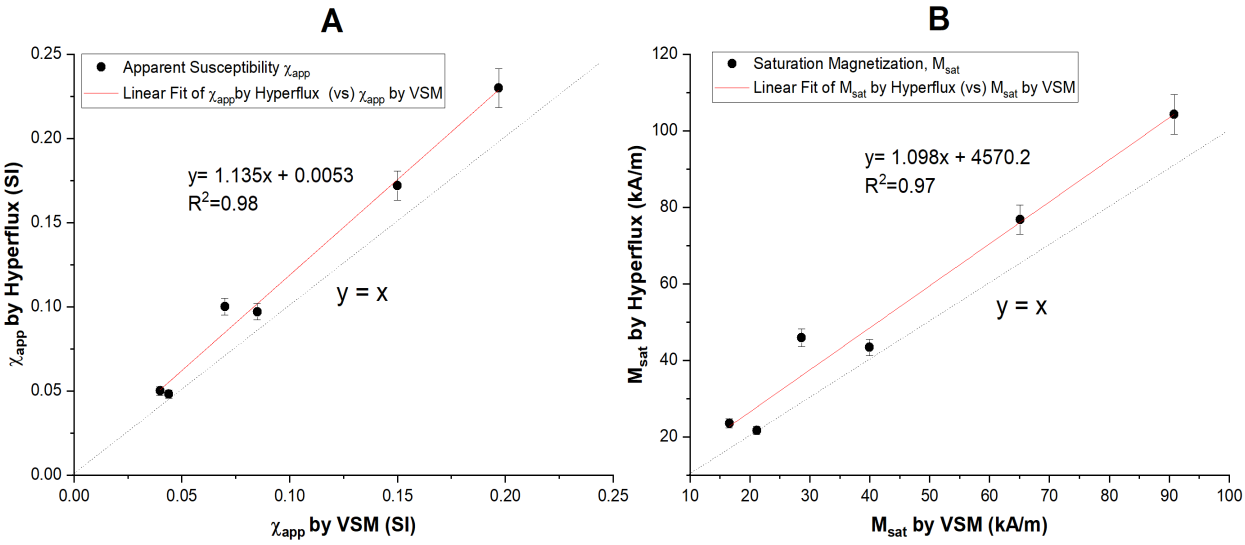

Figure 3.8 - Comparison of intrinsic magnetic properties determined by the two methods.
(A) Apparent volume susceptibility comparison between Hyperflux velocimeter and VSM
(B) Saturation Magnetization comparison between Hyperflux velocimeter and VSM.

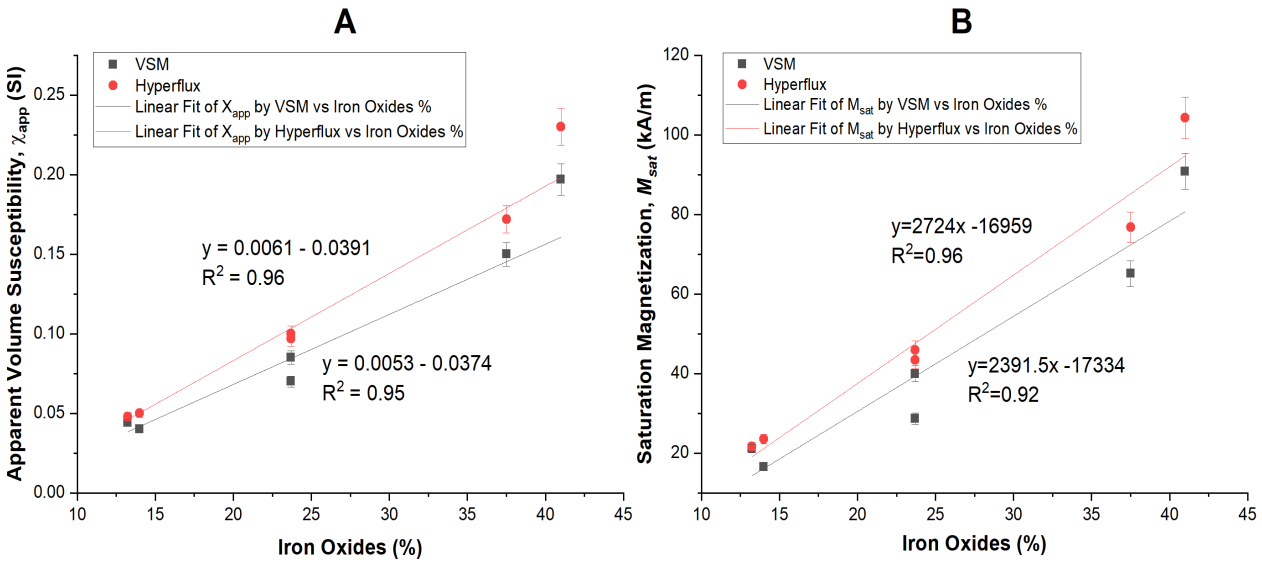

Figure 3.9 - Apparent Susceptibility **(A)** and Saturation Magnetization **(B)** vs. percent iron oxides for P2, P4, P15, N2, N4 and N16 beads listed in Table 3.4.

3.6 Conclusions

Following suitable size calibration of the Hyperflux velocimeter instrument linear calibration curves of particle size provide a means of determining individual actual particle size from the overestimated value given by the captured dark-field image. This benefits researchers and vendors to determine intrinsic magnetic property distributions of magnetic bead samples. Under most conditions of magnetic bead use the beads are magnetically saturated by the applied field, so the appropriate magnetization variables in determining magnetophoretic mobility are *apparent* magnetic susceptibility or saturation magnetization (Sannidhi et al., 2019) as seen in equations 3.3 and 3.4 and not initial magnetic susceptibility (Figure 3.7). It is also seen that apparent magnetic susceptibility will be inversely related to the applied field that magnetizes the beads. One possible measure of bead sample quality is the goodness of fit (R^2) of the $1/D^2$ rule to the two-parameter sample data (Figure 3.5). A poor fit implies large numbers of beads not having the specified per cent iron oxides.

The estimation of intrinsic magnetic properties of individual particles using particle velocimetry (approximate run-time 2 minutes) is time-efficient and reduces the time of analysis by 98% when compared to that of VSM (approximate run-time of 2 hours). Adequate sample size for particle tracking is less than 10^6 beads in total, about $1/1000^{th}$ that required for VSM. A better understanding of particle sample quality is achieved by estimating the magnetic properties of the sample on a particle-by-particle basis. Velocimetry results are in good agreement with VSM, which is a traditional but more demanding measurement, but velocimetry does not produce magnetization curves. Overall, the usage of velocimetry when compared to VSM or SQUID is time efficient and cost-effective.

Acknowledgments

The authors thank Dr. Michael Miller, Auburn University, Auburn, AL, USA and Dr. Michael Buettner, University of Alabama, Tuscaloosa, AL, USA for training and helping in conducting TEM and VSM measurements respectively. Research support was provided by Auburn University Research Funding.

References

Bronzeau, S., & Pamme, N. (2008). Simultaneous bioassays in a microfluidic channel on plugs of different magnetic particles. *Analytica Chimica Acta*, *609*(1), 105–112. https://doi.org/10.1016/J.ACA.2007.11.035.

Chalmers, J. J., Zhao, Y., Nakamura, M., Melnik, K., Lasky, L., Moore, L., & Zborowski, M. (1999). Instrument to determine the magnetophoretic mobility of labeled, biological cells and paramagnetic particles. *Journal of Magnetism and Magnetic Materials*, *194*(1), 231–241. https://doi.org/10.1016/S0304-8853(98)00557-5.

Chertok, B., Moffat, B. A., David, A. E., Yu, F., Bergemann, C., Ross, B. D., & Yang, V. C. (2008). Iron oxide nanoparticles as a drug delivery vehicle for MRI monitored magnetic targeting of brain tumors. *Biomaterials*, *29*(4), 487–496.

Cordova, G., Attwood, S., Gaikwad, R., Gu, F., & Leonenko, Z. (2017). Magnetic force microscopy characterization of superparamagnetic iron oxide nanoparticles (SPIONs). *ArXiv Preprint ArXiv:1704.08316*.

Dearing, J. A. (1999). Environmental Magnetic Susceptibility Using the Bartington MS2 System. *Keniloworth, U.K.: Chi Publishing*, 52.

Eberbeck, D., Wiekhorst, F., Wagner, S., & Trahms, L. (2011). How the size distribution of magnetic nanoparticles determines their magnetic particle imaging performance. *Applied Physics Letters*, *98*(18), 1–4. https://doi.org/10.1063/1.3586776.

Estapor (2018), Estapor SuperParamagnetic Microspheres from MilliporeSigma, [Online]. Available at: https://www.sigmaaldrich.com/content/dam/sigma-aldrich/docs/Sigma-Aldrich/Brochure/1/estapor-superparamagnetic-microspheres.pdf.

Gangopadhyay, S., Hadjipanayis, G. C., Dale, B., Sorensen, C. M., Klabunde, K. J.,

Papaefthymiou, V., & Kostikas, A. (1992). Magnetic properties of ultrafine iron particles. *Physical Review B*, *45*(17), 9778.

Gherca, D., Pui, A., Cornei, N., Cojocariu, A., Nica, V., & Caltun, O. (2012). Synthesis, characterization and magnetic properties of MFe_2O_4(M=Co, Mg, Mn, Ni) nanoparticles using ricin oil as capping agent. *Journal of Magnetism and Magnetic Materials*, *324*(22), 3906–3911. https://doi.org/10.1016/j.jmmm.2012.06.027.

Gibson, F. S. (1936). Magnetic separation method and means. *US Patent no. US2056426A* Washington, DC, USA: U.S. Patent and Trademark Office.

Goya, G. F., Lima Jr, E., Arelaro, A. D., Torres, T., Rechenberg, H. R., Rossi, L., Marquina, C., & Ibarra, M. R. (2008). Magnetic Hyperthermia With Fe_3O_4 Nanoparticles: The Influence of Particle Size on Energy Absorption. *IEEE Transactions on Magnetics*, *44*(11), 4444–4447.

Granata, C., & Vettoliere, A. (2016). Nano superconducting quantum interference device: A powerful tool for nanoscale investigations. *Physics Reports*, *614*, 1–69.

Grob, D. T., Wise, N., Oduwole, O., & Sheard, S. (2018). Magnetic susceptibility characterisation of superparamagnetic microspheres. *Journal of Magnetism and Magnetic Materials*, *452*, 134–140.

Gupta, A. K., & Gupta, M. (2005). Cytotoxicity suppression and cellular uptake enhancement of surface modified magnetic nanoparticles. *Biomaterials*, *26*(13), 1565–1573.

Häfeli, U. O., Ciocan, R., & Dailey, J. P. (2002). Characterization of magnetic particles and microspheres and their magnetophoretic mobility using a digital microscopy method. *European Cells and Materials*, *3*(SUPPL. 2), 24–27.

Hanot, C. C., Choi, Y. S., Anani, T. B., Soundarrajan, D., & David, A. E. (2015). Effects of iron-

oxide nanoparticle surface chemistry on uptake kinetics and cytotoxicity in CHO-K1 cells. *International Journal of Molecular Sciences*, *17*(1), 1–15. https://doi.org/10.3390/ijms17010054.

Harrison, R. G., Todd, P. W., Rudge, S. R., & Petrides, D. P. (2015). *Bioseparations science and engineering*. Oxford University Press, USA.

Haynes, W. M. (2014). *CRC handbook of chemistry and physics*. CRC press, doi: 10.1201/b17118.

Hunt, C. P., Moskowitz, B. M., Banerjee, S. K., & others. (1995). Magnetic properties of rocks and minerals. *Rock Physics and Phase Relations: A Handbook of Physical Constants*, *3*, 189–204.

Hurt, D., Li, S., & Amann, A. (2013). Versatile SQUID susceptometer with multiple measurement modes. *IEEE Transactions on Magnetics*, *49*(7), 3541–3544. https://doi.org/10.1109/TMAG.2013.2241029.

Jie, G., Yang, L., & Jinghai, Y. (2010). Influence of Co-Doping on Synthesis, Structure and Magnetic Properties of Ni Nanoparticles. *Rare Metal Materials and Engineering*, *39*, 328–331.

Jin, X., Zhao, Y., Richardson, A., Moore, L., Williams, P. S., Zborowski, M., & Chalmers, J. J. (2008). Differences in magnetically induced motion of diamagnetic, paramagnetic, and superparamagnetic microparticles detected by cell tracking velocimetry. *Analyst*, *133*(12), 1767–1775.

Jing, Y., Mal, N., Williams, P. S., Mayorga, M., Penn, M. S., Chalmers, J. J., & Zborowski, M. (2008). Quantitative intracellular magnetic nanoparticle uptake measured by live cell magnetophoresis. *The FASEB Journal*, *22*(12), 4239–4247.

Kligfield, R., Owens, W. H., & Lowrie, W. (1981). Magnetic susceptibility anisotropy, strain, and progressive deformation in Permian sediments from the Maritime Alps (France). *Earth and Planetary Science Letters*, *55*(1), 181–189.

Laachir, A., Perrichon, V., Badri, A., Lamotte, J., Catherine, E., Lavalley, J. C., El Fallah, J., Hilaire, L., Le Normand, F., Quéméré, E., & others. (1991). Reduction of CeO_2 by hydrogen. Magnetic susceptibility and Fourier-transform infrared, ultraviolet and X-ray photoelectron spectroscopy measurements. *Journal of the Chemical Society, Faraday Transactions*, *87*(10), 1601–1609.

Lacava, B. M., Azevedo, R. B., Silva, L. P., Lacava, Z. G. M., Neto, K. S., Buske, N., Bakuzis, A. F., & Morais, P. C. (2000). Particle sizing of magnetite-based magnetic fluid using atomic force microscopy: A comparative study with electron microscopy and birefringence. *Applied Physics Letters*, *77*(12), 1876–1878.

Li, Z., Kawashita, M., Kudo, T. A., & Kanetaka, H. (2012). Sol-gel synthesis, characterization, and in vitro compatibility of iron nanoparticle-encapsulating silica microspheres for hyperthermia in cancer therapy. *Journal of Materials Science: Materials in Medicine*, *23*(10), 2461–2469. https://doi.org/10.1007/s10856-012-4735-y.

Liao, S.-H., Huang, H.-S., & Su, Y.-K. (2018). Scaling characteristics of the magnetization increments of functionalized nanoparticles determined using a vibrating sample magnetometer for liquid magnetic immunoassays. *IEEE Sensors Journal*.

Lim, J., Yeap, S. P., Che, H. X., & Low, S. C. (2013). Characterization of magnetic nanoparticle by dynamic light scattering. *Nanoscale Res Lett*, *8*(1), 381. https://doi.org/10.1186/1556-276X-8-381.

Little, C. A. E., Pellegrino, J., & Russek, S. E. (2013). Microfluidic platform for magnetic

nanoparticle trapping and detection. *IEEE Transactions on Magnetics*, *49*(7), 3402–3405. https://doi.org/10.1109/TMAG.2013.2251416.

Liu, W., Zhou, M., & Kong, L. (2009). Estimation of the size distribution of magnetic nanoparticles using modified magnetization curves. *Measurement Science and Technology*, *20*(12). https://doi.org/10.1088/0957-0233/20/12/125802.

Ludwig, F., Balceris, C., Jonasson, C., & Johansson, C. (2017). Analysis of ac susceptibility spectra for the characterization of magnetic nanoparticles. *IEEE Transactions on Magnetics*, *53*(11), 1–4.

Maldonado-Camargo, L., Unni, M., & Rinaldi, C. (2017). *Magnetic Characterization of Iron Oxide Nanoparticles for Biomedical Applications* (pp. 47–71). https://doi.org/10.1007/978-1-4939-6840-4.

Marcon, P., & Ostanina, K. (2012). Overview of Methods for Magnetic Susceptibility Measurement. *PIERS Proceedings*, *5*, 420–424.

Mccloskey, K. E., Chalmers, J. J., & Zborowski, M. (2003). Magnetic Cell Separation : Characterization of Magnetophoretic Mobility to enrich or deplete cells of interest from a heterogeneous. *Analytical Chemistry*, *75*(24), 6868–6874. https://doi.org/10.1021/ac034315j.

McCloskey, K. E., Chalmers, J. J., & Zborowski, M. (2000). Magnetophoretic mobilities correlate to antibody binding capacities. *Cytometry*, *40*(4), 307–315. https://doi.org/10.1002/1097-0320(20000801)40:4<307::AID-CYTO6>3.0.CO;2-H.

McCloskey, K. E., Comella, K., Chalmers, J. J., Margel, S., & Zborowski, M. (2001). Mobility measurements of immunomagnetically labeled cells allow quantitation of secondary antibody binding amplification. *Biotechnology and Bioengineering*, *75*(6), 642–655.

https://doi.org/10.1002/bit.10040.

Moore, L. R., Zborowski, M., Nakamura, M., McCloskey, K., Gura, S., Zuberi, M., Margel, S., & Chalmers, J. J. (2000). The use of magnetic-doped polymeric microspheres in calibrating cell tracking velocimetry. *J. Biochem. Biophys. Methods*, *44*, 115–130.

Paper, I., Popplewell, J., & Sakhnini, L. (1995). *The dependence of the physical and magnetic properties of magnetic fluids on particle size*. *149*, 72–78.

Popa, M., Hong, L. Van, & Kakihana, M. (2003). *Particle morphology characterization and magnetic properties of $LaMnO_{3+d}$ perovskites*. *327*, 237–240.

Reddy, S., Moore, L. R., Sun, L., Zborowski, M., & Chalmers, J. J. (1996). Determination of the magnetic susceptibility of labeled particles by video imaging. *Chemical Engineering Science*, *51*(6), 947–956.

Rembaum, A. (1984). Cell labeling with magnetic and non magnetic immunomicrospheres for separation and diagnosis. *Pure and Applied Chemistry*, *56*(10), 1305–1307.

Sajja, V. S. K., Hanley, T. R., Gapsis, H., Guernsey, B., Kennedy, D. J., Taylor, M. J., Papas, K. K., & Todd, P. W. (2011). Application of magnetic particle tracking velocimetry to quadrupole magnetic sorting of porcine pancreatic islets. *Biotechnology and Bioengineering*, *108*(9), 2107–2117.

Sannidhi, A., Todd, P. W., & Hanley, T. R. (2019). Estimation of Intrinsic Magnetic Properties of Single Particles by Particle Tracking Velocimetry. *IEEE Magnetics Letters*, 1. https://doi.org/10.1109/LMAG.2019.2950298.

Sannidhi, A., Todd, P. W., & Hanley, T. R. (2019). Magnetic Nanoparticle Characterization by Dark-Field Imaging and Bright-Field Absorbance, *120c*. *AIChE Annual Meeting Proceedings 2019.* Avaiable at: https://www.aiche.org/conferences/aiche-annual-

meeting/2019/proceeding/paper/120c-magnetic-nanoparticle-characterization-dark-field-imaging-and-bright-field-absorbance.

Sannidhi, A., Todd, P. W., & Hanley, T. R. (2018). Multiparameter Paramagnetic Particle Characterization By Dark-Field Imaging, *71c*. *AIChE Annual Meeting Proceedings 2018.* Avaiable at: https://www.aiche.org/conferences/aiche-annual-meeting/2018/proceeding/paper/71c-multiparameter-paramagnetic-particle-characterization-dark-field-imaging.

Shi, Y., Pramanik, A., Tchounwou, C., Pedraza, F., Crouch, R. A., Chavva, S. R., Vangara, A., Sinha, S. S., Jones, S., Sardar, D., Hawker, C., & Ray, P. C. (2015). Multifunctional Biocompatible Graphene Oxide Quantum Dots Decorated Magnetic Nanoplatform for Efficient Capture and Two-Photon Imaging of Rare Tumor Cells. *ACS Applied Materials and Interfaces*, *7*(20), 10935–10943. https://doi.org/10.1021/acsami.5b02199.

Sinha, B., Anandakumar, S., Oh, S., & Kim, C. (2012). Micro-magnetometry for susceptibility measurement of superparamagnetic single bead. *Sensors and Actuators, A: Physical*, *182*(May), 34–40. https://doi.org/10.1016/j.sna.2012.05.001.

Sullivan, M., & Prorok, B. C. (2015). A biosensor based on magnetic resonance relaxation. *Sensing for Agriculture and Food Quality and Safety VII*, *9488*, 94880B.

Sun, S., Murray, C. B., Weller, D., Folks, L., & Moser, A. (2000). Monodisperse FePt nanoparticles and ferromagnetic FePt nanocrystal superlattices. *Science*, *287*(5460), 1989–1992.

Tadic, M., Panjan, M., Damnjanovic, V., & Milosevic, I. (2014). Magnetic properties of hematite (α-Fe_2O_3) nanoparticles prepared by hydrothermal synthesis method. *Applied Surface Science*, *320*, 183–187.

Tarasov, K. A., Isupov, V. P., Bokhonov, B. B., Gaponov, Y. A., Tolochko, B. P., Yulikov, M. M., Yudanov, V. F., Davidson, A., Beaunier, P., Marceau, E., & Che, M. (2008). Control of particle size via chemical composition: Structural and magnetic characterization of Ni-Co alloy nanoparticles encapsulated in lamellar mixed oxides. *Microporous and Mesoporous Materials*, *107*(1–2), 202–211. https://doi.org/10.1016/j.micromeso.2007.05.026.

Tay, Z. W., Chandrasekharan, P., Chiu-Lam, A., Hensley, D. W., Dhavalikar, R., Zhou, X. Y., Yu, E. Y., Goodwill, P. W., Zheng, B., Rinaldi, C., & others. (2018). Magnetic particle imaging-guided heating in vivo using gradient fields for arbitrary localization of magnetic hyperthermia therapy. *ACS Nano*, *12*(4), 3699–3713.

Watarai, H., & Namba, M. (2002). Capillary magnetophoresis of human blood cells and their magnetophoretic trapping in a flow system. *Journal of Chromatography A*, *961*(1), 3–8. https://doi.org/10.1016/S0021-9673(02)00748-3.

Weegman, B. P., Kumar Sajja, V. S., Suszynski, T. M., Rizzari, M. D., Scott III, W. E., Kitzmann, J. P., Mueller, K. R., Hanley, T. R., Kennedy, D. J., Todd, P. W., & others. (2016). Continuous quadrupole magnetic separation of islets during digestion improves purified porcine islet viability. *Journal of Diabetes Research*, *2016*.

Williams, P. S., Zborowski, M., & Chalmers, J. J. (1999). Flow rate optimization for the quadrupole magnetic cell sorter. *Analytical Chemistry*, *71*(17), 3799–3807. https://doi.org/10.1021/ac990284.

Wise, N., Grob, D. T., Morten, K., Thompson, I., & Sheard, S. (2015). Magnetophoretic velocities of superparamagnetic particles, agglomerates and complexes. *Journal of Magnetism and Magnetic Materials*, *384*, 328–334. https://doi.org/10.1016/j.jmmm.2015.02.031.

Xu, J., Mahajan, K., Xue, W., Winter, J. O., Zborowski, M., & Chalmers, J. J. (2012). Simultaneous, single particle, magnetization and size measurements of micron sized, magnetic particles. *Journal of Magnetism and Magnetic Materials*, *324*(24), 4189–4199. https://doi.org/10.1016/j.jmmm.2012.07.039.

Yen, S. P. S., Rembaum, A., & Molday, R. S. (1980). Cell sorting apparatus. *U.S. Patent No. 4,219,411*. Washington, DC: U.S. Patent and Trademark Office.

Yu, F., Zhang, L., Huang, Y., Sun, K., David, A. E., & Yang, V. C. (2010). The magnetophoretic mobility and superparamagnetism of core-shell iron oxide nanoparticles with dual targeting and imaging functionality. *Biomaterials*, *31*(22), 5842–5848.

Zborowski M, Chalmers J J (2011), Magnetic cell separation (Vol. 32), *Elsevier*.

Zborowski, M., Chalmers, J., & Moore, L. R. (1999). Method for determining particle characteristics. *US Patent US6142025*, Washington, DC, USA: U.S. Patent and Trademark Office.

Zborowski, M., Sun, L., Moore, L. R., Williams, P. S., & Chalmers, J. J. (1999). Continuous cell separation using novel magnetic quadrupole flow sorter. *Journal of Magnetism and Magnetic Materials*, *194*(1–3), 224–230.

Zhang, H., Moore, L. R., Zborowski, M., Williams, P. S., Margel, S., & Chalmers, J. J. (2005). Establishment and implications of a characterization method for magnetic nanoparticle using cell tracking velocimetry and magnetic susceptibility modified solutions. *Analyst*, *130*(4), 514–527. https://doi.org/10.1039/b412723d.

Zhao, B., Wan, X., Song, W., Sun, Y., & Du, J. (2000). Nano-MgO particle addition in silver-sheathed $(Bi,Pb)_2Sr_2Ca_2Cu_3O_x$ tapes. *Physica C: Superconductivity and Its Applications*, *337*(1), 138–144. https://doi.org/10.1016/S0921-4534(00)00074-5.

Zhou, C., Boland, E. D., Todd, P. W., & Hanley, T. R. (2016). Magnetic particle characterization—magnetophoretic mobility and particle size. *Cytometry Part A*, *89*(6), 585–593. https://doi.org/10.1002/cyto.a.22866.

Zhou, C., Choi, Y. S., David, A. E., Todd, P. W., & Hanley, T. R. (2018). Nanomaterial endocytosis: Estimation of particles per cell by magnetic measurement. *IEEE Magnetics Letters*, *9*, 7–11. https://doi.org/10.1109/LMAG.2018.2830754.

Zhou, C., Qian, Z., Choi, Y. S., David, A. E., Todd, P., & Hanley, T. R. (2017). Application of magnetic carriers to two examples of quantitative cell analysis. *Journal of Magnetism and Magnetic Materials*, *427*(November 2016), 25–28. https://doi.org/10.1016/j.jmmm.2016.11.009.

Chapter 4 - Methods to Estimate Magnetophoretic Mobility of Individual Magnetic Nanoparticles

Abstract

Magnetic particle characterization determines the quality of the magnetic particles and is of great importance in particle technology, drug delivery, cell separation, in vivo diagnostics, and other biomedical applications. The Hyperflux^{TM} velocimeter is utilized to provide quantitative video analysis of particles using a high definition camera and captures the images of the particle trajectories in an isodynamic field. The direct measurement of magnetophoretic mobility of the particles with a size of less than 400 nanometers is limited by optical resolution. To overcome the size limitation, six different approaches such as optical density methods, chain velocity methods, and intrinsic magnetic properties were studied to estimate the mobility of 100 nm beads. The optical density method is based on optical absorbance versus time measured in a bright field. The chain velocity method takes advantage of chain formation of the superparamagnetic nanoparticles in an applied magnetic field, making particles visible in the dark field and extrapolates the magnetophoretic mobility of nanoparticle chains. The estimation of magnetophoretic mobility of magnetic nanoparticles using dark-field particle tracking gives more reasonable results when compared to the optical density methods.

Keywords: magnetophoretic mobility, magnetic nanobead characterization, chain velocity, nanoparticle magnetophoretic mobility.

4.1 Introduction

Superparamagnetic Iron Oxide Nanoparticles (SPIONs) in the size range of 10 to 500 nm are biocompatible and most widely used in various biomedical applications such as drug delivery and targeting (Mahmoudi et al., 2011), cell separation (Williams et al., 1999; Zborowski & Chalmers, 2011), magnetic resonance imaging (Chertok et al., 2008; Eberbeck et al., 2011; Yoffe et al., 2013), cellular phagocytosis/endocytosis studies (Gupta & Gupta, 2005; Hanot et al., 2015; Jie et al., 2010; Jing et al., 2008; Prijic et al., 2010; Zhou et al., 2017, 2018). The magnetic properties of individual nanoparticles such as magnetophoretic mobility and intrinsic magnetic properties are of greater importance when compared to that of bulk average values. Ongoing research has estimated the magnetophoretic mobility of single magnetic nanoparticles by different research groups (Grob et al., 2018; Maldonado-Camargo et al., 2017; Wise et al., 2015).

In this study, the velocimeter instrument was used to conduct dark field and bright field experiments. The direct mobility measurement of nanoparticles by velocimeter using the darkfield technique is limited by optical resolution. The objective of single-nanoparticle mobility measurement was to enable the determination of magnetic properties using the velocimeter at the nanoscale of below 400 nm at which most of the drug targeting and cellular studies are focused. Six different approaches were studied to measure magnetophoretic mobility of individual magnetic nanoparticles using the optical density method, chain velocity method, and intrinsic magnetic properties. Among the different approaches, the chain velocity methods are more reasonable and estimated by more robust methods than the optical density methods.

4.2 Theory

Magnetophoretic mobility is estimated by the ratio of terminal velocity (v_m) attained by the particle to the applied magnetic pressure (S_m)

$$U_m = \frac{v_m}{S_m} \tag{4-1}$$

The applied magnetic pressure is given by

$$S_m = \frac{B_o(dB/dx)}{\mu_o} \tag{4-2}$$

Here, B_o represents the applied magnetic field intensity, (dB/dx) is the gradient of the magnetic field, μ_o is the magnetic permeability constant.

Additional theory is provided for each of the methods applied to single-particle mobility estimation in each subsection of 4.5 - Results and Discussion.

4.3 Materials and Methods

4.3.1 Magnetic Nanoparticles

FluidMag-DXS nanoparticles of size 100 nm (procured from Chemicell, Germany) with dextran-sulfate (DXS) coating were studied in this research.

4.3.2 LED white light

A single LED light procured from LEDGLE (rechargeable Neck LED light Model no-2710750-DW) with Daylight white color (6500 - 7500K), 3.7 V, and 650 mAh Li-on battery was

used to produce a bright field imaging setup. This LED light has dual features of flood and spotlight.

4.3.3 Hyperflux™ velocimeter (original and modified)

The description of the unmodified original velocimeter is given in the 3.3.2 section of Chapter-3. This instrument is used to measure mobility data using the dark-field imaging technique. To overcome the limitation of poor focus of nanoparticles, we modified the instrument to conduct bright field-optical density experiments. The modifications include the following major changes in the original instrument setup. By opening the back cabinet of the instrument, the foam plug from the center of illumination ring was replaced with the LED light to focus on the sweet spot of the channel cell. The LED light was covered with a double layer of white office paper acting as a diffuser to produce uniform illumination. The instrument has been operated semi-manually by disengaging all lines from their valves and using slide clamps (Qosina slide clamps-13014 which fits 0.125-inch OD tubing) to control the input/output flow of the sample and buffer through the sample channel cell. The sample has been inserted into the channel cell using 1 mL syringes (Air-Tite 1 mL Luer lock syringes) and the waste line has been terminated into a waste beaker. Since the optical density method involves high particle concentrations, the modified instrument has been designed to minimize sample volume usage and to be able to preserve sample after the experiment.

4.3.4 Food coloring

La Flor food coloring (blue, yellow, and red) were combined in equal volumes to produce a dark grey solution which gives a good absorbance with the LED light.

4.3.5 Spectrophotometer and method of use

The SpectraMax i3 instrument from Molecular Devices (San Jose, CA) was used to measure the absorbance of different dye and particle suspensions of 200 μL volume in a 96-well plate reader.

4.3.6 Procedures

4.3.6.1 Experimental procedure for optical density method

The velocimeter was modified to record the movement of magnetic nanoparticles and the clearing rate of SPIONs to determine the velocity of nanoparticles in the applied magnetic field. For this modified instrument setup as described in 4.4.3, ensure that the sample chamber is filled with the suspension of particles. Establish a typical mobility experiment in the instrument using IKOVision software. In the 'new experiment' window change the following parameters as follows: 'number of sets=1' and 'number of seconds=1'. The image acquisition should be done without activating the values and vacuum pump. The captured images will be stored in the 'experiments' directory of the computer.

4.3.6.2 Image analysis for optical density method

The captured images were analyzed further to estimate grey value of the image using ImageJ^{TM} software. A long narrow horizontal scan rectangle was selected on the image (free from unwanted dark and bright spots); the traces were better when both flood and spotlight setting were employed in the LED light. Finally, the grey value of the region of interest was estimated by clicking 'Analyze', then 'Plot Profile' option of the ImageJ^{TM} software interface. The grey value represents the brightness of image pixels ranging from 0 to 255 (where 0 is black and 255 is white in ImageJ^{TM}). The grey values of the selected region are converted to arbitrary intensities by

dividing the measured grey value with its maximum value of 255, for better comparison with the absorbance (arbitrary) measured by spectrophotometer and find the clearing rate of the particles.

4.3.6.3 Experimental procedure for the chain velocity method

The typical mobility experiments have been conducted in the original velocimeter instrument dark-field setup (unmodified). The image analysis is done by Cytotest^{TM} software by using a standard intensity threshold setting of 35, and the size gating range of 2 to 300 squared pixels. In this method, three parameters of interest analyzed are 'tAvgElongation', 'tMobility' and 'tLength' from the 26-parameter list-mode of the "tracks.csv" spreadsheet. The parameter 'tAvgElongation' is the ratio of length to width of the captured image blob, which is proportional to the length of the formed nanoparticle chains. The parameter 'tLength' is the length of the particle track captured by the camera and 'tMobility' is the mobility of the individual tracked particle.

4.4 Results and Discussion

4.4.1 Optical Density Method- Optical density change in velocimeter

The idea of this approach was to measure the absorbance of nanoparticle concentration change with respect to time and characterize the clearing rate of particle concentration from the concentration versus time data to get the magnetophoretic mobility of the 100 nm magnetic nanoparticles. The velocimeter was subjected to modifications by changing the light illumination from dark field to bright field setup. A black food color solution was used to estimate the concentration range of particles required for the optical density experiments and to know the absorbance range of LED light used in the velocimeter.

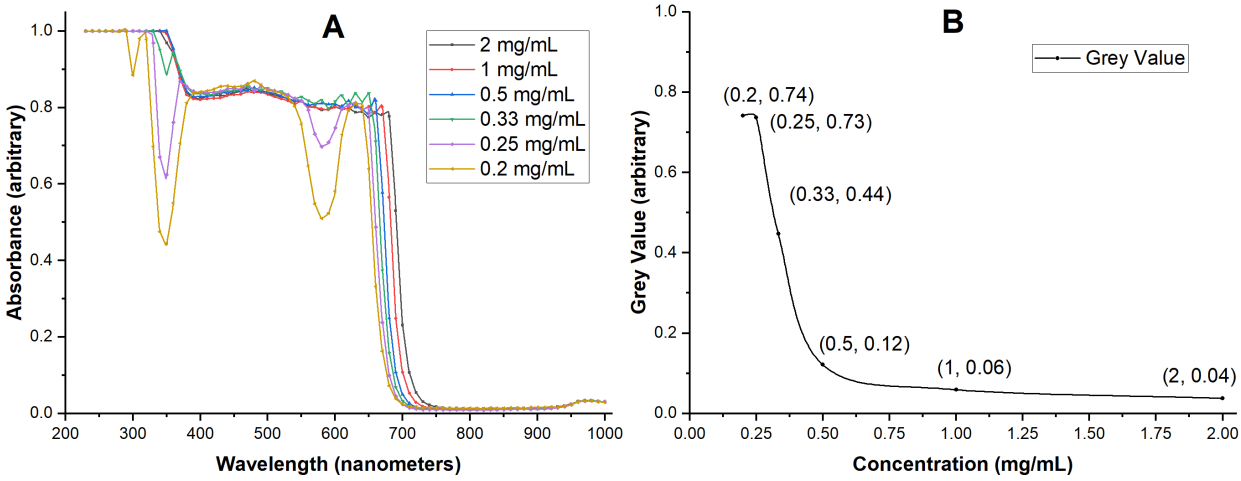

Figure 4.1 - **(A)** Absorbance versus wavelength spectrum of black food color measured by a spectrophotometer at different concentrations of 0.2, 0.25, 0.33, 0.5, 1, and 2 mg/mL and **(B)** Grey value of black food color measured by ImageJ at different concentrations of 0.2, 0.25, 0.33, 0.5, 1, and 2 mg/mL.

The calibration curve for the black food color solution is obtained from the greyscale data of captured images measured by image processing software ImageJ. The comparison of absorbance by spectrophotometer (Spectramax i3) and greyscale value (ImageJ) for the food color solution is shown in Figure 4.1. The grey value (0= black and 255= white) of the captured images decreased as the concentration increased. The data points of grey value do not trend downward below 0.2 and above 2.0 mg/mL. At low concentrations (below 0.2 mg/mL) the concentrations are below the error of the measurement method; at high concentrations (above 2.0 mg/mL), the measurement was too close to zero to be above the error of the measurement (Sannidhi et al., 2019).

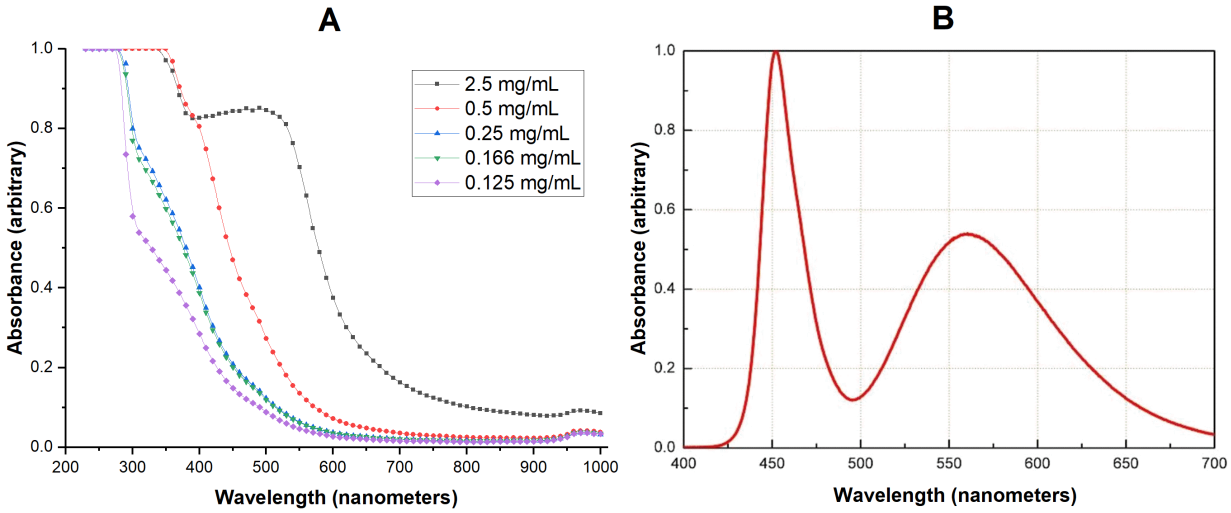

Figure 4.2 - (A) Particle absorption spectrum and **(B)** LED emission spectrum.

The greyscale data range/ bandwidth (0 to 0.8 approximately) of food color solution is reasonable as shown in Figure 4.1 (B) and helps in finding the concentration clearing rate which is evident from the comparison of absorbance measured by spectrophotometer given in Figure 4.1 (A). The emission spectrum of cool white LED light and the absorbance spectrum of magnetic particles are in the acceptable range to be able to conduct experiments in the velocimeter (Figure 4.2) (Digikey LED Lighting- https://www.digikey.com/en/products).

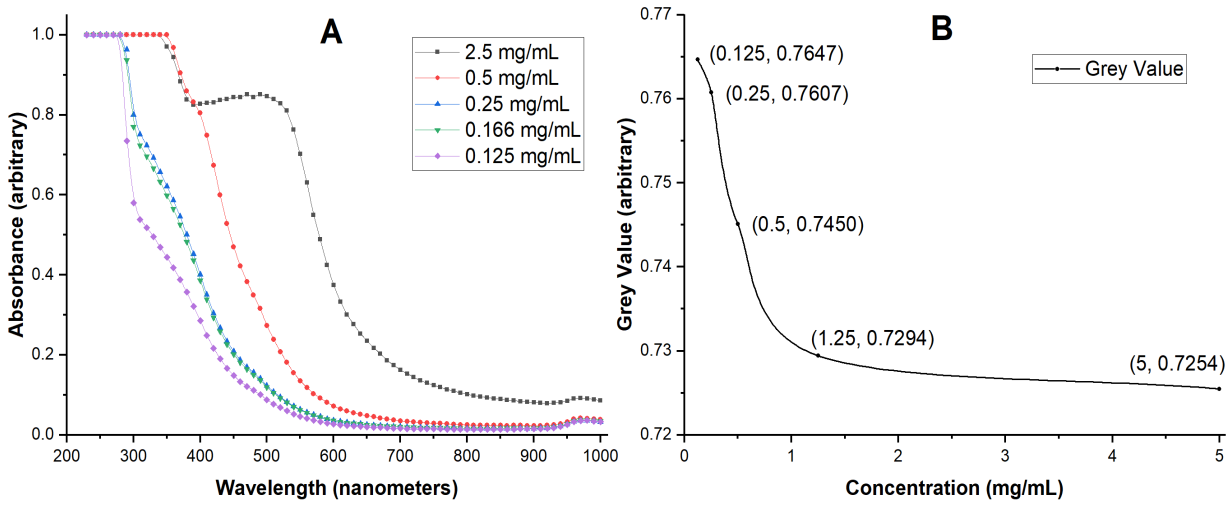

Figure 4.3 - (A) Absorbance vs Wavelength spectrum of 100nm magnetic beads measured by Spectrophotometer at different concentrations of 0.125, 0.166, 0.25, 0.5, and 2.5 mg/mL (repeated from 4.2(A) to indicate particle concentration range) and **(B)** Grey value of 100 nm magnetic beads measured by ImageJ at different concentrations of 0.125, 0.25, 0.5, 1.25 and 5 mg/mL.

The absorbance of nanoparticles at different concentrations was measured by using a spectrophotometer and the velocimeter as shown in Figure 4.3 (A) and (B) respectively. The absorbance bandwidth for the particle concentrations used in the velocimeter was low (0.72 to 0.77) and not sufficient to generate significant data points to estimate the mobility of nanoparticles. The use of light absorption to monitor particle concentration in the velocimeter was not possible owing to very small changes in grey value resulting from the thinness of the chamber. Even at

these high particle concentrations (up to 5 mg/mL) the volume fraction that absorbs light was too small to absorb appreciable intensity in the light path.

Effect of Pathlength- The pathlength of light in the velocimeter is 0.3 mm (thickness of sample channel cell) and that of the spectrophotometer is about 6.96 mm (diameter of a single well of 96-well plate). Thus, the pathlength of light using the velocimeter is reduced by more than 95%.

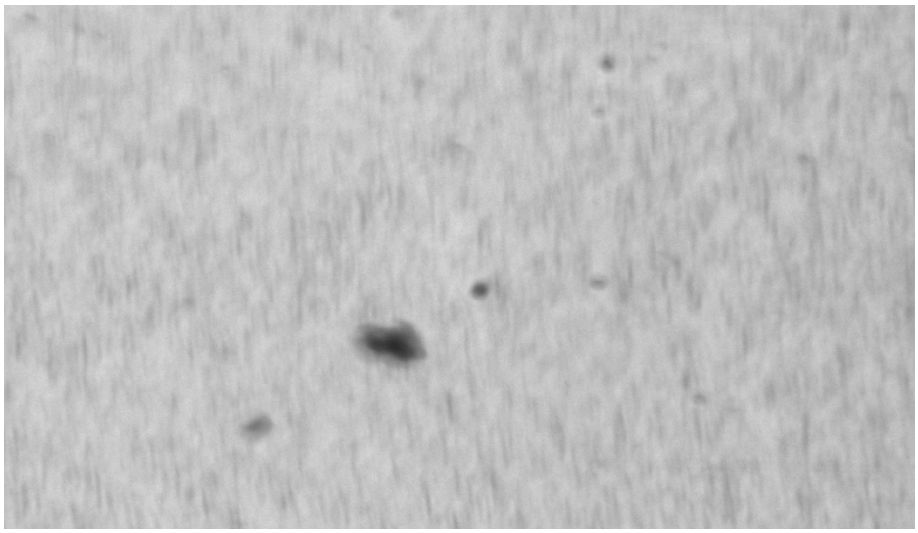

Figure 4.4 - The SPIONs chains formed in bright field illumination

Effect of volume fraction- The sufficiently large volume fraction is not achievable due to chain formation (Figure 4.4); therefore, taking advantage of chain formation as a means of making particles visible leads to a chain velocity method in dark field setup.

4.4.2 Optical Density Change in Microwell Plate

There are three approaches to deriving mobility from the work of (Yeh et al., 2020).

4.4.2.1 Using parameters from Yeh's theory

From the theoretical background of work done by Yeh et al., a non-linear curve fit was used for the optical density versus time data, given by equation 4-3. The magnetic attraction rate (β) values at different concentrations and sizes of SPIONs were estimated using this equation.

$$c = c_o e^{-\beta t} \tag{4-3}$$

where c is the final concentration, c_o is the initial concentration of magnetic particles and t is the time of attraction. The magnetic attraction rate was assumed to be the function of particle size (R_p), given by the following equation:

$$\beta = \frac{A'}{R_p} + B' R_p^2 \tag{4-4}$$

where the parameters A' and B' are given by,

$$A' = -\frac{kT}{6\pi\eta}\frac{\nabla^2 c}{c_o} \tag{4-5}$$

$$B' = \frac{2}{9\eta}\left(\nabla\left(\vec{M}.\vec{B}\right).\frac{\nabla c}{c_o} + \frac{c}{c_o}\nabla^2\left(\vec{M}.\vec{B}\right)\right) \tag{4-6}$$

The magnetophoretic mobility can be found from the above equations based on dimensional analysis of some of the variables used in the above equations. (Yeh et al., 2020)

Units of A' , B' and β assist in finding the mobility of SPIONs as follows:

$$Units\ of\ A' = \frac{m}{s}$$

$$Units\ of\ B' = \frac{1}{m^2.s}$$

The dimensions of magnetophoretic mobility are

$$\mathrm{U}_m = \frac{v}{\nabla\left(\frac{B_o^2}{2\mu_o}\right)} = \frac{m^3}{T.A.s}$$

Given that $1N = T.A.m$, the units of $\mathrm{U_m}$ are

$$\frac{m^3}{T.A.s} = \frac{m^4}{N.s}$$

Since the particle size is measured in nanoscale, the dimension 'meter' mentioned in the above equation will be replaced by 'nanometers'

$$Units\ of\ B' = \frac{1}{nm^2.s}$$

From equation 4-4, we get

$$Units\ of\ \beta = Units\ of\ \frac{A'}{R_p} = \frac{1}{s}$$

By using the above terms, along with the fluid viscosity, the dimensions are

$$\frac{\beta}{B'\eta} = \frac{nm^2.m^2}{N.s}$$

$$\frac{\beta}{B'\eta} * 10^{-18} = \frac{m^4}{N.s}$$

The dimensions of above equation agree with those of magnetophoretic mobility.

$$\frac{\beta}{B'\eta} * 10^{-18} = \mathrm{U}_m = \frac{m^4}{N.s} = Rm$$

The units of magnetophoretic mobility are expressed in Rembaum (*Rm)* equivalent to the SI units of $m^4.\ N^{-1}.\ s^{-1}$. Hence, magnetophoretic mobility could be calculated using the equations 4-7 or 4-8.

$$\mathrm{U}_m = \frac{\beta}{B'\eta} * 10^{-18} \qquad (4\text{-}7)$$

$$\mathrm{U}_m = \frac{A'}{R_p B' \eta} * 10^{-18} \qquad (4\text{-}8)$$

From the relationship between β and particle size R_p, the values of *A'* and *B'* were reported using the plots between different β values at different particle sizes. The mobility of nanoparticles was estimated by using equations 4-7 and 4-8 as given below.

From equation 4-7:

For starch coated particles with a particle size of about 100 nm

$$\mathrm{U}_m = \frac{\beta}{B' \eta} * 10^{-18} = \frac{20}{(7 * 10^{-3}) * (10^{-3})} * 10^{-18} \frac{m^4}{N.s}$$

$$\mathrm{U}_m = 2.8\, pRm$$

For aminated starch coated particles with particle size of about 100 nm

$$\mathrm{U}_m = \frac{\beta}{B' \eta} * 10^{-18} = \frac{21}{(6 * 10^{-3}) * (10^{-3})} * 10^{-18} \frac{m^4}{N.s}$$

$$\mathrm{U}_m = 3.5\, pRm$$

For pegylated starch coated particles with particle size of about 100 nm

$$\mathrm{U}_m = \frac{\beta}{B' \eta} * 10^{-18} = \frac{15}{(5 * 10^{-3}) * (10^{-3})} * 10^{-18} \frac{m^4}{N.s}$$

$$\mathrm{U}_m = 3.0\, pRm$$

From equation 4-8:

Using equation 4-8 the approximate values of A' reported by Yeh et al. by considering standard deviation and magnitude alone are 300, 1000, and 500 for starch, aminated starch, and pegylated beads respectively.

For starch coated particles with particle size of 100 nm

$$\mathrm{U}_m = \frac{A'}{R_p B' \eta} * 10^{-18} = \frac{300}{100 * (7 * 10^{-3}) * (10^{-3})} * 10^{-18} \frac{m^4}{N.s}$$

$$\mathrm{U}_m = 0.4\ pRm$$

For aminated starch coated particles with particle size of about 100 nm

$$\mathrm{U}_m = \frac{A'}{R_p B' \eta} * 10^{-18} = \frac{1000}{100 * (6 * 10^{-3}) * (10^{-3})} * 10^{-18} \frac{m^4}{N.s}$$

$$\mathrm{U}_m = 1.7\ pRm$$

For pegylated starch coated particles with particle size of about 100 nm

$$\mathrm{U}_m = \frac{A'}{R_p B' \eta} * 10^{-18} = \frac{500}{100 * (5 * 10^{-3}) * (10^{-3})} * 10^{-18} \frac{m^4}{N.s}$$

$$\mathrm{U}_m = 0.7\ pRm$$

4.4.2.2 Using Model Magnet-1

An arbitrarily chosen magnet typically used in the field with known magnetic parameters-magnetic field (B_o) and magnetic field gradient (dB/dx) was used to estimate magnetophoretic mobility of magnetic nanoparticles (100 nm). By estimating particle velocity from the work of Yeh et al., estimating geometry, using the model magnet parameters from (Cooper et al., 2004)

and the concept of clearing rate of particles from early research at the University of Colorado (Al-Mutairi, 1998; Davis & Hassen, 1988), the mobility is:

$$U_m = \frac{v_m}{S_m}$$

$$v_m = \frac{3\ mm}{500\ s} = 6 * 10^{-6} \frac{m}{s}$$

$$S_m = \frac{B.(dB/dx)}{\mu_o} = \frac{(100\ mT).(28\ mT/mm)}{4\pi * 10^{-7}\ T.m/A} * \frac{10^3\ mm}{m} * \frac{10^{-6}\ T^2}{mT^2} = 2.23 * 10^6\ \frac{T.A}{m^2}$$

$$U_m = \frac{v_m}{S_m} = \frac{6 * 10^{-6}\ m/s}{2.23 * 10^6\ T.A/m^2}$$

$$U_m = \ 2.7\ pRm$$

4.4.2.3 Using Model Magnet-2

Another magnet (model magnet-2) which was used by Cribb et al. was employed to estimate the mobility of nanoparticles (100 nm). Estimating minimum particle velocity from the dimensions of a single well of 96 well plate, using actual geometry

$$U_m = \frac{v_m}{S_m}$$

The distance traveled for the particles from the center of a single well of 96 well plate is (center to wall distance) is 3.4 mm. The total time of particle movement from the center to wall is 1600 seconds (Yeh et al., 2020).

$$v_m = \frac{3.4\ mm}{1600\ s} = 2.12 * 10^{-6} \frac{m}{s}$$

By using the model magnet from the work done by Cribb et al. with B_o = 0.35 T and adjusting to 0.25T, we get the following parameters.

At 5.9 mm, B_o = 0.022 T, and dB/dx = 7 T/m,

$$S_m = \frac{B.(dB/dx)}{\mu_o} = \frac{(0.022\ T).(7\ T/m)}{4\pi * 10^{-7}\ T.m/A} = 1.22 * 10^5\ \frac{T.A}{m^2}$$

$$U_m = \frac{v_m}{S_m} = \frac{2.12 * 10^{-6}\ m/s}{1.22 * 10^5\ T.A/m^2}$$

$$U_m = 17.37\ pRm$$

This value and the previous value are very high, most likely due to the underestimation of magnet parameters which had not been measured in the cited study. A more precise value of the magnet parameters would be useful. The long duration of exposure to the field is likely to result in the formation of chains, possibly very long chains, thereby contributing to increased mobility.

4.4.3 Calculation based on Volume Susceptibility

The size of the magnetite crystallite in these 100 nm beads is estimated at some 10 nm diameter (Wallyn et al., 2019). Calculating its volume susceptibility from its mass susceptibility of 11 x 10^{-4} m^3/kg and multiplying by the volume ratio to that of the 100 nm bead gives χ_p = 5.7 x 10^{-3}, which is close to the value of 4.9 x 10^{-3} used by (Zhou et al., 2018). Calculating from the equation of mobility of particle (U_p),

$$U_p = \frac{\chi_p d_p^2}{18\eta} \qquad (4\text{-}9)$$

$$U_p = \frac{(4.9 * 10^{-3}).(105 * 10^{-9}\ m)^2}{(18).(10^{-3}\ N.s/m^2)}$$

$$U_p = 0.003\ pRm$$

4.4.4 Chain Velocity Method

The chain formation of SPIONs at higher concentrations was the motivation to conduct the chain velocity method using velocimeter measurements. The dark-field mobility measurements were made to determine single-particle mobility by extrapolation. The normal volume fraction required for dark- field mobility experiments ranges from 10^{-8} to 10^{-6}. The high-volume fraction in this method includes a volume fraction of 10^{-3}. Above this volume fraction, there was insufficient space for the particles to move freely in the thin channel cell and webbing of particle tracks was observed.

The theoretical background required for the chain velocity method is as follows: the magnetic force acting on a single nanoparticle is given by

$$F_m = \Delta\chi V\nabla\left(\frac{B_o^2}{2\mu_o}\right) \tag{4-10}$$

The magnetic force acting on a chain of 'n' nanoparticles (Wise et al., 2015) is given by

$$F_m^* = nF_m \tag{4-11}$$

The drag force acting on a chain of nanoparticles when the magnetic field is perpendicular to the net force is given by

$$F_d = 8\pi\eta d_p v[\mathrm{N}] \tag{4-12}$$

where

$$[N] = \frac{n^2 - 1}{\left[\frac{2n^2 - 3}{\sqrt{n^2 - 1}}\right]\left[\ln\left(n + \sqrt{n^2 - 1}\right)\right] + n} \tag{4-13}$$

where d_p is the diameter of one nanoparticle, v is the terminal velocity, η is viscosity of solution, n is the number of nanoparticles per chain. [N] is the drag force proportionality constant (Kasper, 1985; Wise et al., 2015).

Equation 4-13 does not lend itself easily to extrapolation (to n = 1, for example, our goal). Using a second-order curve fit,

$N = -0.0006n^2 + 0.1164n + 0.3166$ and $R^2 = 0.9998$ with [N]=0.4324 at n=1.

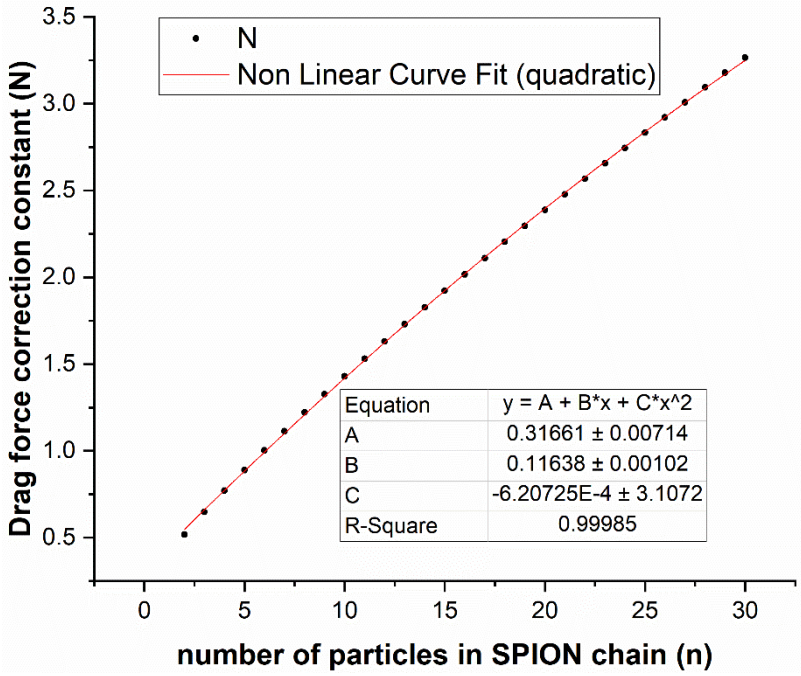

Figure 4.5 - The drag force correction factor [N] versus number of particles in SPION chain (n).

The chain length is given by the product of number of particles per chain (n) and diameter of the particle (d_p) as

$$Chain\ Length = n * d_p \tag{4-14}$$

Force balance gives the magnetophoretic mobility of nanoparticle chains denoted by U_m^* as

$$F_m^* - F_d = 0 \tag{4-15}$$

$$U_m^* = \frac{v}{\nabla\left(\frac{B_o^2}{2\mu_o}\right)} \tag{4-16}$$

Substituting,

$$U_m^* = \frac{n\Delta\chi V}{8\pi\eta \mathrm{d[N]}} \tag{4-17}$$

Substituting the volume of spherical nanoparticles into equation 4-17,

$$U_m^* = \frac{nd^2\Delta\chi}{48\eta[\mathrm{N}]} \tag{4-18}$$

As the magnetophoretic mobility is calculated by calculating the terminal velocity and the applied magnetic pressure using equation 4-1, the intrinsic properties of nanoparticles can be estimated as well.

Comparison of the mobility of microparticles and nanoparticle chains:

From the theory of velocimetry, magnetophoretic mobility is

$$U_m = \frac{d_p^2\Delta\chi}{18\eta} \tag{4-19}$$

Comparing the relationship between the mobility of chains estimated from Wise et al., and the mobility of particles estimated using velocimeter (U_m), the magnetophoretic mobility of nanoparticle chains (U_m^*) is given by the

$$U_m^* = \frac{3n}{8[\mathrm{N}]}U_m \tag{4-20}$$

The value of $\frac{3n}{8[N]}$ is 0.8672 for a single nanobead, knowing the value of $[N]$ as 0.4324 at n=1. Mobility of 105 nm starch coated beads chains using the equation 4-19 as reported in section 4.5.3, is 0.003 pRm (where 1 pRm= 10^{-12} m^3/T.A. s). Mobility of single bead using equation 4-18 or 4-20, where N= 0.4324 for n=1, and with the help of the above-mentioned data for 105 nm beads gives a value of U_m= 0.0026 pRm. The theoretical mobility versus chain length (Figure 4.6) was generated using the equation 4-20 given the initial value of 0.0026 pRm for single nanobead mobility. The theoretical curve fit for U_m versus chain length, at a chain length of 1, gives U_m = 0.0025 pRm as shown in Figure 4.6.

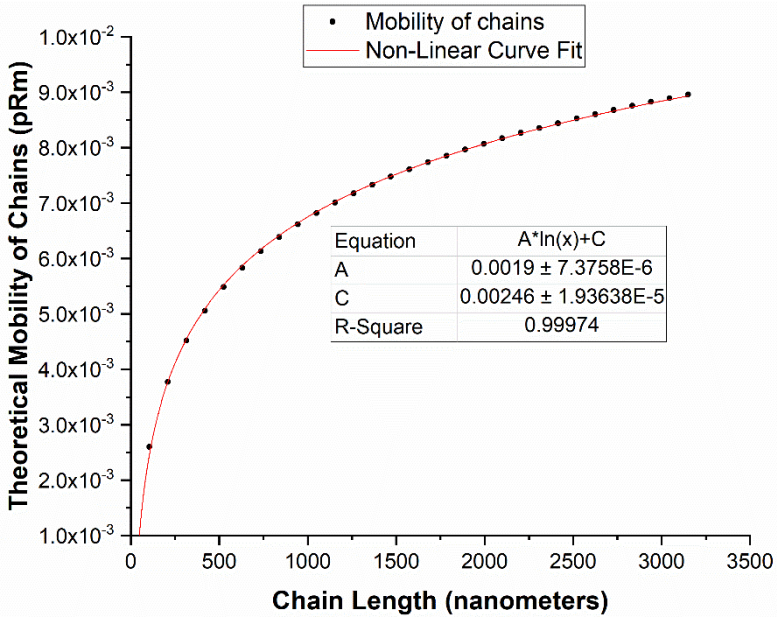

Figure 4.6 - Theoretical mobility versus chain length plots with a non-linear curve fit.

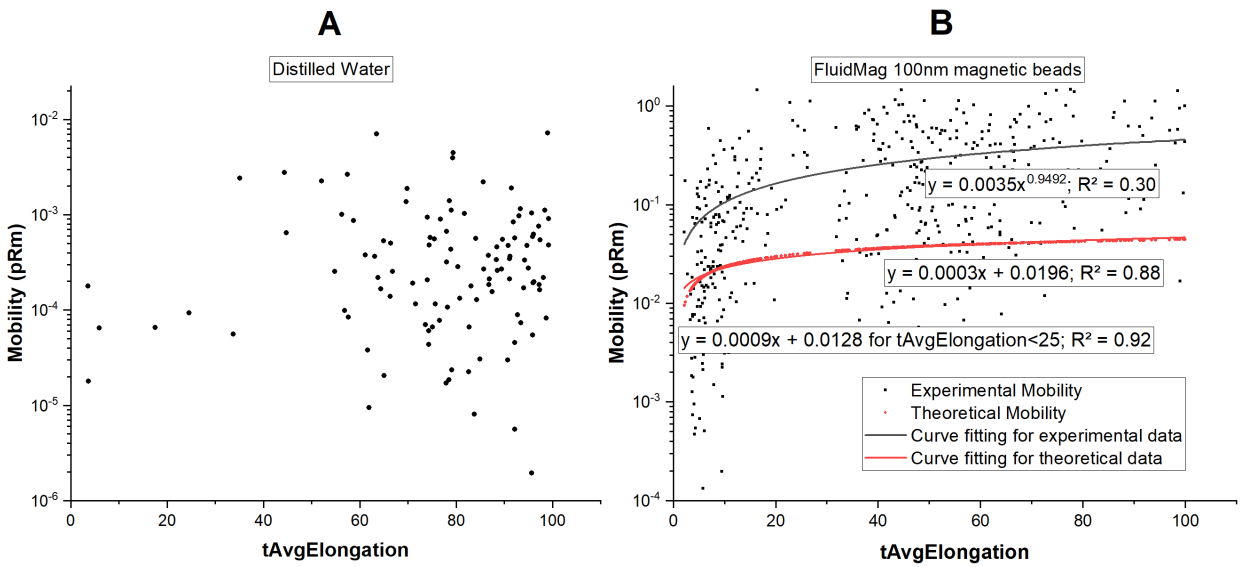

Figure 4.7 - Experimental mobility versus tAvgElongation for **(A)** the distilled water and **(B)** 100 nm magnetic beads

The experimental mobility estimated by the velocimeter instrument given by the tracks spreadsheet (tMobility) was plotted with tAvgElongation (Figure 4.7) upon filtering the data with the data filter tLength>5. This data filter sorted and selected the beads that moved through at least 5 video frames during the experimental image acquisition. The parameter tAvgElongation recorded for each particle by the velocimeter software was defined as the length-to-width ratio of the object averaged over all video frames in which the object was present. Mathematically this is the same as n. Figure 4.7 (A) is the filtered data of mobility versus tAvgElongation for a distilled water sample in the velocimeter. Nearly all points fall below 0.001 pRm and correspond to non-magnetic events.

Four curve-fitting exercises were applied to the (highly scattered) data set shown in Figure 4.7 (B). From the simple exponential (upper) curve fit of the experimental mobility as shown in Figure 4.7 (B), the mobility was estimated as 0.0035 pRm at n=1 upon extrapolation. This fits with low correlation coefficient. The mobility calculated from the experimental tAvgElongation

data using the theoretical fitting equation of y=0.0019ln(n)+0.00246, as predicted in Figure 4.6, is shown in the Figure 4.7 (B) as the red curve and corresponds to the data with $R^2 = 0.88$ giving a single-bead mobility of 0.00246 pRm as mentioned above. From the linear fitting equation of the full data set (curve not shown), the mobility $U_m = 0.02$ pRm at n=1 with $R^2 = 0.88$. The longer chains typically have $U_m = 0.2$ pRm, with minimum values of 0.001 pRm. Emphasizing the mobilities of shorter chains, the plot of tMobility vs. tAvgElongation with the filters of tLength> 5 and tAvgElongation < 25, shows a cluster around $U_m = 0.005$ pRm, and a linear curve fit gives a value of $U_m = 0.013$ pRm with $R^2 = 0.92$.

4.4.5 Mobility of Labeled Cells

The relationship used to calculate the number of beads per cell (n) in (Zhou et al., 2018) work is given by

$$n = \frac{18\eta U_c D_c}{\chi_p d_p^3} \tag{4-21}$$

where U_c is the mobility of cell, D_c is the diameter of the cell, χ_p is the susceptibility of the particle, and d_p is the diameter of the particle (p for particle, c for cell).

Substituting from equation 4-9,

$$U_p = \frac{\chi_p d_p^2}{18\eta}$$

so that

$$\chi_p d_p^3 = 18\eta U_p d_p$$

Solving for U_p:

$$U_p = \frac{U_c D_c}{n d_p} \tag{4-22}$$

where n = 6.7 x 10^5 estimated from Ferrozine assay, an independent measurement of the number of beads/cell (Zhou et al., 2018), giving

$$U_p = \frac{U_c D_c}{n d_p}$$

$$U_p = \frac{(13.3\ pRm).(16\ \mu m)}{(6.7 * 10^5).(105 * 10^{-3} \mu m\ )}$$

$$U_p = \ 0.003\ pRm$$

4.4.6 Calculation Based on Saturation Magnetization

For the starch coated 100 nm magnetic particles, a typical literature value of saturation magnetization is given as M_s = 50 emu/g (Dung et al., 2009). The resulting saturation magnetization (M_s) in SI units is 13.5 x 10^4 A/m (assuming a density of 2.7 g/cm^3 for the particle). This value is similar to the saturation magnetization for the smallest beads (700 nm) reported in Chapter-3 (Sannidhi et al., 2019). Mobility is calculated from its relationship between saturation magnetization given by,

$$U_m = \frac{M_s d^2 \mu_o}{18 \eta B_o} \tag{4-23}$$

$$U_m = \frac{(13.5 * 10^4\ \ A/m).(1 * 10^{-7}\ m)^2.\ \ (4\pi * 10^{-7}\ \ T.m/A)}{(18).(10^{-3}\ \ N.s/m^2).(0.56\ T)}$$

$$U_m = \ 0.168\ pRm$$

4.4.7 Summary and comparison of results

All the mobility values estimated using different approaches are tabulated in Table 4.1.

Table 4.1 - Magnetophoretic mobility of magnetic nanoparticles of 100 nm size estimated using different approaches.

Method number	Description	Magnetophoretic Mobility, pRm
1	OD Change in Microwell Plate, based on β	2.8
2	OD Change in Microwell Plate, based on A'/R_p	0.4
2	OD Change in Microwell Plate, magnet 1	2.7
3	OD Change in Microwell Plate, magnet 2	17.3
4	Chain Velocity Method in Velocimeter, exponential fit	0.003
5	Chain Velocity Method in Velocimeter, linear fit	0.02
6	Chain Velocity Method in Velocimeter, cluster	0.005
7	Chain Velocity Method in Velocimeter, linear fit (n<25)	0.013
8	Chain Velocity Method in Velocimeter, theory	0.0025
9	Mobility of Labeled Cells	0.003
10	Calculation Based on Volume Susceptibility	0.003
11	Calculation Based on Saturation Magnetization	0.17

4.5 Conclusions

The magnetophoretic mobilities of magnetic nanoparticles and single nanobeads have been estimated using different approaches. The optical density (OD) methods gave high values of mobility, due to lack of accurate magnetic force information and formation of longer chains by

exposure to the magnetic field for longer durations and at high particle concentrations. Methods using the velocimeter instrument (chain velocity method, mobility of labeled cells, intrinsic magnetic properties) gave reasonable values of magnetophoretic mobility of single nanobeads which are estimated by more robust methods. The most frequently encountered values are around 0.003 pRm and are based on the more robust approaches. There is a reasonable agreement between experimental and theoretical mobility values obtained by most of the methods used by velocimeter instrument.

Acknowledgments

Research support was provided by Auburn University Research Funding. Extensive guidance and data sharing were provided by Dr. Allan David and Dr. Barry Yeh.

References

Al-Mutairi, N. Z. (1998). Investigating the effect of settling time on DNP biodegradation in a sequencing batch reactor. *University of Colorado at Boulder Dissertations.*

Chertok, B., Moffat, B. A., David, A. E., Yu, F., Bergemann, C., Ross, B. D., & Yang, V. C. (2008). Iron oxide nanoparticles as a drug delivery vehicle for MRI monitored magnetic targeting of brain tumors. *Biomaterials*, *29*(4), 487–496.

Cooper, R. P., Doyle, J. F., Dunn, D. S., Vellinger, J. C., & Todd, P. (2004). Multistage Magnetic Particle Separator II. Classification of Ferromagnetic Particles. *Separation Science and Technology*, *39*(12), 2809–2825. https://doi.org/10.1081/SS-200028762.

Cribb, J. A., Meehan, T. D., Shah, S. M., Skinner, K., & Superfine, R. (2010). Cylinders vs. spheres: biofluid shear thinning in driven nanoparticle transport. *Annals of Biomedical Engineering*, *38*(11), 3311–3322.

Davis, R. H., & Hassen, M. A. (1988). Spreading of the interface at the top of a slightly

polydisperse sedimenting suspension. *Journal of Fluid Mechanics*, *196*, 107–134.

Digikey LED lighting. (n.d.). https://www.digikey.com/products/en/optoelectronics/led-lighting-white/124?FV=37%7C421162%2C-8%7C124&quantity=0&ColumnSort=-1614&page=19&pageSize=25.

Dung, T. T., Danh, T. M., Hoa, L. T. M., Chien, D. M., & Duc, N. H. (2009). Structural and magnetic properties of starch-coated magnetite nanoparticles. *Journal of Experimental Nanoscience*, *4*(3), 259–267. https://doi.org/10.1080/17458080802570609.

Eberbeck, D., Wiekhorst, F., Wagner, S., & Trahms, L. (2011). How the size distribution of magnetic nanoparticles determines their magnetic particle imaging performance. *Applied Physics Letters*, *98*(18), 1–4. https://doi.org/10.1063/1.3586776.

Grob, D. T., Wise, N., Oduwole, O., & Sheard, S. (2018). Magnetic susceptibility characterisation of superparamagnetic microspheres. *Journal of Magnetism and Magnetic Materials*, *452*, 134–140.

Gupta, A. K., & Gupta, M. (2005). Cytotoxicity suppression and cellular uptake enhancement of surface modified magnetic nanoparticles. *Biomaterials*, *26*(13), 1565–1573.

Hanot, C. C., Choi, Y. S., Anani, T. B., Soundarrajan, D., & David, A. E. (2015). Effects of iron-oxide nanoparticle surface chemistry on uptake kinetics and cytotoxicity in CHO-K1 cells. *International Journal of Molecular Sciences*, *17*(1), 1–15. https://doi.org/10.3390/ijms17010054.

Jie, G., Yang, L., & Jinghai, Y. (2010). Influence of Co-Doping on Synthesis, Structure and Magnetic Properties of Ni Nanoparticles. *Rare Metal Materials and Engineering*, *39*, 328.

Jing, Y., Mal, N., Williams, P. S., Mayorga, M., Penn, M. S., Chalmers, J. J., & Zborowski, M. (2008). Quantitative intracellular magnetic nanoparticle uptake measured by live cell

magnetophoresis. *The FASEB Journal*, *22*(12), 4239–4247.

Kasper, G. (1985). Measurements of Viscous Drag on Cylinders and chains of spheres with aspect ratios between 2 and 50. *Journal of aerosol science*, *16*(6), 535-556.

Mahmoudi, M., Sant, S., Wang, B., Laurent, S., & Sen, T. (2011). Superparamagnetic iron oxide nanoparticles (SPIONs): Development, surface modification and applications in chemotherapy. *Advanced Drug Delivery Reviews*, *63*(1), 24–46. https://doi.org/https://doi.org/10.1016/j.addr.2010.05.006.

Maldonado-Camargo, L., Unni, M., & Rinaldi, C. (2017). *Magnetic Characterization of Iron Oxide Nanoparticles for Biomedical Applications* (pp. 47–71). https://doi.org/10.1007/978-1-4939-6840-4.

Prijic, S., Scancar, J., Romih, R., Cemazar, M., Bregar, V. B., Znidarsic, A., & Sersa, G. (2010). Increased Cellular Uptake of Biocompatible Superparamagnetic Iron Oxide Nanoparticles into Malignant Cells by an External Magnetic Field. *The Journal of Membrane Biology*, *236*(1), 167–179. https://doi.org/10.1007/s00232-010-9271-4.

Sannidhi, A., Todd, P. W., & Hanley, T. R. (2019). Estimation of Intrinsic Magnetic Properties of Single Particles by Particle Tracking Velocimetry. *IEEE Magnetics Letters*, 1. https://doi.org/10.1109/LMAG.2019.2950298.

Sannidhi, A., Todd, P. W., & Hanley, T. R. (2019). Magnetic Nanoparticle Characterization By Dark-Field Imaging and Bright-Field Absorbance, *120c*. *AIChE Annual Meeting Proceedings 2019.* Avaiable at: https://www.aiche.org/conferences/aiche-annual-meeting/2019/proceeding/paper/120c-magnetic-nanoparticle-characterization-dark-field-imaging-and-bright-field-absorbance.

Wallyn, J., Anton, N., & Vandamme, T. F. (2019). Synthesis, Principles, and Properties of

Magnetite Nanoparticles for In Vivo Imaging Applications-A Review. *Pharmaceutics*, *11*(11), 601. https://doi.org/10.3390/pharmaceutics11110601.

Williams, P. S., Zborowski, M., & Chalmers, J. J. (1999). Flow rate optimization for the quadrupole magnetic cell sorter. *Analytical Chemistry*, *71*(17), 3799–3807. https://doi.org/10.1021/ac990284+.

Wise, N., Grob, D. T., Morten, K., Thompson, I., & Sheard, S. (2015). Magnetophoretic velocities of superparamagnetic particles, agglomerates and complexes. *Journal of Magnetism and Magnetic Materials*, *384*, 328–334. https://doi.org/10.1016/j.jmmm.2015.02.031.

Yeh, B. J., Anani, T., & David, A. E. (2020). Improving the Size Homogeneity of Multicore Superparamagnetic Iron Oxide Nanoparticles. *International Journal of Molecular Sciences*, *21*(10), 3476.

Yoffe, S., Leshuk, T., Everett, P., & Gu, F. (2013). Superparamagnetic iron oxide nanoparticles (SPIONs): synthesis and surface modification techniques for use with MRI and other biomedical applications. *Current Pharmaceutical Design*, *19*(3), 493–509.

Zborowski, M., & Chalmers, J. J. (2011). *Magnetic cell separation* (Vol. 32). Elsevier.

Zhou, C., Choi, Y. S., David, A. E., Todd, P. W., & Hanley, T. R. (2018). Nanomaterial endocytosis: Estimation of particles per cell by magnetic measurement. *IEEE Magnetics Letters*, *9*, 7–11. https://doi.org/10.1109/LMAG.2018.2830754.

Zhou, C., Qian, Z., Choi, Y. S., David, A. E., Todd, P., & Hanley, T. R. (2017). Application of magnetic carriers to two examples of quantitative cell analysis. *Journal of Magnetism and Magnetic Materials*, *427*(November 2016), 25–28. https://doi.org/10.1016/j.jmmm.2016.11.009.

Chapter 5 - Quantification of Magnetically Labeled CHO-K1 Cells to Infer Roles of Different Endocytosis Mechanisms

Abstract

The receptor-independent endocytosis is one of the common mechanisms of particles in the size range of 100 nm. The characterization of receptor-independent uptake mechanisms is important due to their major role in cell growth regulation and development. Magnetic nanoparticles (MNPs) of size 100 nm with varied surface modifications are extensively used in cell labeling, cell purification, cell physiology, endocytosis, biochemical micro assays, endosome research, cell separation, drug targeting, and in vivo diagnostics. Magnetic cytometry by velocimetry records the motion of labeled cells in an isodynamic magnetic field thereby estimating the key parameter, magnetophoretic mobility of labeled cells. Magnetophoretic mobility is proportional to the number of particles ingested per cell. The Hyperflux^{TM} velocimeter uses particle tracking velocimetry to measure magnetophoretic mobility, size and other morphological parameters of magnetic particles and labeled cells. The rapid estimation of magnetophoretic mobility by the instrument and collection of multiple thousand data points facilitates cellular uptake quantification and kinetic studies in less time than any other existing technique. The receptor-independent uptake by cultured CHO (Chinese Hamster Ovary) cells of 100 nm iron oxide nanoparticles with different surface coatings, namely starch, dextran sulfate (DXS), and amino groups, was studied to reveal the role of nanoparticle endocytosis mechanisms. Caveolae-mediated and clathrin-coated endocytosis are revealed by using specific mechanism-based inhibitors such as Genistein and Chlorpromazine Hydrochloride. Uptake inhibition has been investigated at different inhibitor concentrations during endocytosis by evaluating the cellular

survival rate, inhibitor toxicity, and uptake of nanoparticles with the different surface coatings, which also reveal the relevance of surface charge.

Keywords: magnetophoretic mobility, endocytosis mechanisms, surface modifications, mechanism-based inhibitors.

5.1 Introduction

Magnetic nanoparticles with the superparamagnetic nature of the inner iron oxide core and biocompatibility of the outer shell with different surface coatings are widely used in different therapeutic and biomedical applications such as drug delivery and targeting (Kim et al., 2012; Mahmoudi et al., 2011; Strojan et al., 2017; J. Zhou et al., 2013), cell separation (Williams et al., 1999; Zborowski & Chalmers, 2011), hyperthermia (Gazeau et al., 2008), magnetic resonance imaging (Chertok et al., 2008; Eberbeck et al., 2011; Yoffe et al., 2013; Yu et al., 2010), cellular phagocytosis/endocytosis studies (Gupta & Gupta, 2005; Hanot et al., 2015; Jie et al., 2010; Jing et al., 2008; Prijic et al., 2010; C. Zhou et al., 2017, 2018). Ongoing research for quantifying cellular uptake and different endocytosis mechanisms of magnetic nanoparticles and non-magnetic nanomaterials (such as gene vectors, liposomes, air contaminants and viruses) employs a variety of methods such as fluorescence spectroscopy (Knežević & Lin, 2013; Strojan et al., 2017), flow cytometry (Hathaway et al., 2011), magnetic bead enzyme-linked immunosorbent assay (ELISA) method (Chen et al., 2011; Kala et al., 1997; Liao et al., 2016), immunofluorescent microscopy (Kiselev et al., 1999; Lundkvist et al., 1993), inductively coupled plasma (ICP)-based spectroscopic techniques including -optical emission spectrometry (ICP-OES) (Nguyen et al., 2018), mass spectrometry (ICP-MS) (Jeong & Lim, 2018), focused ion beam scanning electron microscopy (FIB-SEM) (Ahlberg et al., 2014; Lee et al., 2007), transmission electron microscopy (TEM) (Strojan et al., 2017). Magnetophoretic mobility measurement of magnetically labeled

cells is a facile, cost-effective and more robust method for estimating superparamagnetic iron oxide nanoparticles (SPIONs) uptake. The cellular uptake of SPIONs by Chinese Hamster Ovary cell line (CHO-K1) with the velocimeter instrument has been investigated and optimum instrument threshold and size gating settings were determined previously (Zhou, 2017). The study of roles of endocytosis mechanisms of the magnetic beads with different surface coatings is focused in this research.

Cellular endocytosis is classified into two main categories: Phagocytosis (restricted to specialized cells only) and pinocytosis (occurs in almost all cell types). Pinocytosis is further classified into three different mechanisms, namely, clathrin dependent (Xu et al., 2013); clathrin independent and macro-pinocytosis (Dutta & Donaldson, 2012; Sahay et al., 2010). The clathrin independent mechanism is further subdivided into caveolae mediated (Kiss & Botos, 2009) and caveolae and clathrin independent mechanism (Damm et al., 2005). The most commonly used chemical inhibitors such as chlorpromazine, potassium depletion, genistein, methyl-β-cyclodextrin (M β CD) have heterogeneous effects in terms of cytotoxicity and inhibitor specificity and are cell line dependent (Vercauteren et al., 2010). Table 5.1 provides information of different chemical inhibitors used in the literature and their uses.

The adopted endocytosis and uptake mechanisms of nanoparticles depends on size, shape and intrinsic surface properties of individual particles and plays a major role in characterization and quantification of the labeled cells. The magnetic properties of individual nanoparticles such as magnetophoretic mobility and intrinsic magnetic properties are of much importance in assessing the particle quality and cellular uptake kinetics (Sannidhi et al., 2019; C. Zhou et al., 2016, 2018). In this study, caveolae mediated and clathrin mediated endocytosis mechanisms were inhibited by

using two different chemical inhibitors, genistein and chlorpromazine respectively at different concentrations.

Genistein is an isoflavone drug derived from soy products and used in the treatment of many chronic diseases, diabetes, tumors and menopausal symptoms (Akiyama & Ogawara, 1991; Hsiao et al., 2019). It is a tyrosine-kinase inhibitor and causes local disruption of the actin network at the site of endocytosis (Thangavel et al., 2019). It inhibits cancer cell invasion and metastasis at nanomolar to micromolar concentrations (Pavese et al., 2010). The cell growth and cell cycle progression of normal human lymphocytes and human leukemic MOLT-4 and HL-60 cells were effected by genistein, reported at different concentrations and incubation periods(Traganos et al., 1992).

Table 5.1 - Common chemical inhibitors used to inhibit different endocytosis mechanisms.

Inhibited Endocytosis Mechanism	**Chemical Inhibitors**	**Comments**	**References**
Caveolae Mediated Endocytosis	MβCD, methyl-beta-cyclodextrin	• Removes cholesterol out of the plasma membrane • Interferes fluid phase endocytosis and CME	(Dutta & Donaldson, 2012; Sahay et al., 2010; Vercauteren et al., 2010)
	Filipin	• Binds to cholesterol in the membrane • Toxic at higher concentration; inhibits CME	
	PP2 (4-amino-5-(4-chloro-phenyl)-7-(*t*-butyl) pyrazolo[3,4-*d*] pyrimidine)	• Inhibitor for Src- family kinases	
	Genistein	• Inhibition of the mammalian hexose transporter GLUT1, tyrosine kinases, cytosine methylation	

Clathrin Mediated Endocytosis	Hypertonic sucrose	• Traps clathrin in microcages • Nonspecific; interferes with fluid phase macropinocytosis	(Dutta & Donaldson, 2012; Sahay et al., 2010; Vercauteren et al., 2010)
	Cytochalasin D	• Depolymerizes F-actin • Affects most endocytic pathways	
	Latrunculin A	N/A	
	Chlorpromazine	• Translocates clathrin and AP2 from the cell surface to intracellular endosomes	
	Potassium Depletion	• Aggregates clathrin • Nonspecific; affects actin cytoskeleton	

Chlorpromazine, having cationic amphiphilic properties, induces inhibition of clathrin and AP2 transportation at the cell membrane. Chlorpromazine applications include treatment of chemoresistant glioma (Oliva et al., 2017), inhibition of histamine release from human lung fragments (Church & Young, 1983), cell-cell fusion, clathrin-mediated endocytosis (Liu et al., 2015), replication of West Nile virus (WNV), Middle east respiratory syndrome-coronavirus (MERS-CoV) (Momattin et al., 2019) and Severe Acute Respiratory Syndrome-coronavirus (SARS-CoV) (Dyall et al., 2014). Chlorpromazine at the concentration of 20 μM inhibited SARS-CoV (Inoue et al., 2007) and completely inhibited MERS-CoV infected cells at a concentration of 12 μM (De Wilde et al., 2014). The drug Chlorpromazine has antiviral activity, where the half maximal effective or inhibitory concentration (EC_{50} or IC_{50}) for Chlorpromazine towards different RNA-viruses ranges from 1 to 10 μM (Otręba et al., 2020).

The objective of this chapter is to determine how nanomaterials enter cells (endocytosis pathway mechanism) by characterizing and quantifying cellular uptake, cell toxicity/viability and roles of different endocytosis mechanisms of magnetically labeled mammalian cells by measuring magnetophoretic mobility using a velocimeter. In this study, the cellular uptake mainly depends on two independent parameters, namely zeta potential of the beads (electrostatic interaction between the particle and biological environment), and the inhibitor toxicity. The toxicity constant for the inhibitors were determined using the magnetophoretic mobility data. The major dominant mechanisms of endocytosis of magnetic beads with starch, aminated starch, dextransulfate (DXS) and aminated dextran sulfate coatings by CHO-KI cells were estimated.

5.2 Theory

Magnetophoretic mobility of the labeled cells is estimated by the ratio of terminal velocity (v_m) attained by the magnetically labeled cell to the applied magnetic pressure (S_m)

$$U_m = \frac{v_m}{S_m} \tag{5-1}$$

The applied magnetic pressure is given by

$$S_m = \frac{B_o(dB/dx)}{\mu_o} \tag{5-2}$$

Here, B_o represents the applied magnetic field intensity, (dB/dx) is the gradient of the magnetic field, and μ_o is the magnetic permeability constant.

5.3 Materials and Methods

5.3.1 Magnetic Nanoparticles

FluidMAG nanoparticles of size 100 nm with different surface coatings such as starch coating (fluidMAG-D) and dextran-sulfate coating (fluidMAG-DXS) were procured from Chemicell (Germany). Coating methods are described below.

5.3.2 Mammalian Cells

Chinese Hamster Ovary (CHO-K1) Cells (catalogue no: ATCC CCL-61) obtained from ATCC (Manassas, VA, USA) were used in this research.

5.3.3 Chemical Inhibitors

In this study, to focus on specific type of endocytosis mechanism, two different mechanism-based chemical inhibitors namely, Genistein (Catalogue No: TCG0272) and Chlorpromazine Hydrochloride (Catalogue No: TCC2481) procured from VWR (Radnor, PA, USA) were used.

5.3.4 Hyperflux™ velocimeter

The velocimeter instrument (described in section 3.3.2 of Chapter-3) is used to quantify the endocytosis mechanisms by estimating magnetophoretic mobility of labeled cells. The average mobilities of the labeled cells were determined by applying two data filters, tAvgIntensity >130 and tMobility >0 to the raw mobility data taken from tracks.csv spreadsheet generated by the instrument.

5.3.5 Dynamic Light Scattering (DLS)

Zetasizer Nano Series- Nano ZS (Malvern Panalytical Inc., MA, USA) was used to estimate hydrodynamic size (backscattering angle = 173°) and zeta potential (Smoluchowski model) of different magnetic nanoparticles by dynamic light scattering technique.

5.3.6 Spectrophotometer

The FlexStation 3 Multi-Mode Microplate Reader instrument (Molecular Devices, San Jose, CA) was used to measure the absorbance of labeled cells for cell viability studies.

5.3.7 Procedures

5.3.7.1 SPIONs surface modification

The unmodified SPIONs with starch and dextransulfate surface coatings were cross-linked and modified with aminosilane coating to yield aminated starch and aminated DXS beads (Figure 5.1) by following the protocols described in the literature (Anani, 2018; Cole et al., 2011).

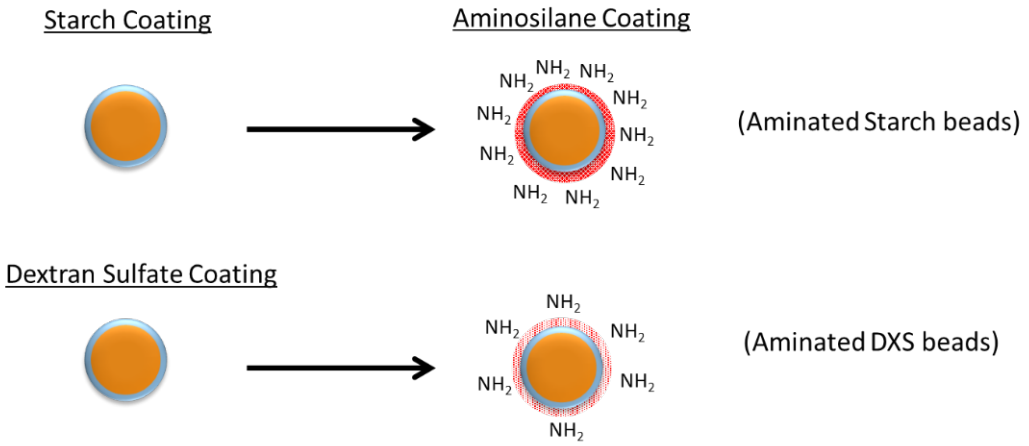

Figure 5.1 - SPIONs surface modifications - Aminosilane coating for starch and dextran-sulfate beads.

Ferrozine assay was used to measure iron concentration of magnetic beads. Briefly, unmodified SPIONs (starch and dextran-sulfate coated SPIONs) were mixed with NaOH solution. After 15

minutes of incubation at room temperature, epichlorohydrin is added and incubated for 24 hours to introduce amine reactive epoxy groups. These cross-linked SPIONs are then shaken with concentrated NH_4OH-producing aminated SPIONs. The amine quantification was done by quantitative fluorescamine assay and confirmed using the positive zeta potential values when compared to those of unmodified beads (Anani, 2018; C. Zhou, 2017).

5.3.7.2 Chinese Hamster Ovary (CHO-K1) cells subculture

CHO-K1 cell lines are maintained as a monolayer in a humidified incubator (95% air, 5% CO_2) in a six well plate with complete cell culture media. The complete cell culture medium consists of 10% (v/v) Fetal Bovine Serum (FBS) (VWR Life Science Seradigm), 89% (v/v) F-12K Nutrient Mixture (Kaighn's Mod.) with L-glutamine, Corning™ (VWR), and 1% (v/v) Antibiotic solution. The following steps were all conducted within an approved biosafety cabinet. Discard the cell culture medium from T-75 flask (surface area of 75 cm^2). Briefly rinse the cell monolayer with 10 mL Hanks' Balanced Salt Solution (HBSS) (VWR Life Science) and discard the HBSS. Add 1 mL TrypLE™ Express- dissociation reagent (Thermofisher Scientific) and transfer the flask to the incubator. Incubate for 5 minutes at 37°C in the incubator to detach the cells from the surface. Transfer the flask from incubator to biosafety cabinet and add 10 mL HBSS and transfer the cell suspension from flask to 50 mL centrifuge tube (VWR). Centrifuge at 1500 rpm for 5 minutes. Transfer the tube to the biosafety cabinet, then discard the supernatant. Add 5 mL new culture medium. Pipette to resuspend the cells. Collect some cell solution to a new flask with 14 mL culture medium (subcultivation ratio is about 1:8). Incubate the cells at 37 °C in the incubator. All the laboratory equipment and collected waste during and after the experiments was sterilized in an autoclave (Primus Sterilizer Co).

5.3.7.3 Cell labeling with SPIONs using inhibitors

CHO-K1 cells were counted using a hemacytometer by taking a few microliters of the cell suspension and viewing under VWR™ Trinocular inverted microscope to determine the count (number of cells per mL). CHO-K1 cell lines may be seeded/plated at about 1 x 10^6 cells into each well of a six-well plate, then add the culture medium up to 2 mL. Incubate at 37°C for 24 hours in the incubator. Next, change the culture media and add mechanism-based inhibitors (such as genistein (1 mg/ mL dissolved in dimethyl sulfoxide (DMSO)) at a concentration ranging from 0 - 300 μM (micro molar); and chlorpromazine (1 mg/ mL dissolved in DMSO) at a concentration of 0-10 μM. Then add SPIONs (superparamagnetic iron oxide nanoparticles) to cell solution to allow the magnetic particles to enter the cell membrane (iron concentration of 100 μg/mL). Incubate at 37°C for 24 hours in the incubator. Measurements of cell morphology and cell viability are then taken using standard microscopy or spectroscopy methods (trypan blue indicator cell counts by VWR™ Trinocular inverted microscope and MTT assay absorbance measurement by spectrophotometer).

5.3.7.4 Sample preparation for velocimeter analysis

Discard the culture media from the six well plate. Wash the cell monolayer using 2 mL HBSS and incubate for three minutes at 37°C. Repeat the above two steps five times and transfer the well plate to the biosafety cabinet. Add 0.5 mL TripLE Express and incubate 5 to 10 minutes in the incubator at 37°C. Collect the cell suspension into a 50 mL centrifuge tube. Centrifuge at 1500 rpm for 5 minutes, transfer the tube to the biosafety cabinet, discard supernatant and resuspend the cell with 4 mL 1X-PBS. Collect the cell suspension for later testing in the velocimeter instrument (C. Zhou, 2017).

5.3.7.5 Cellular Viability

MTT Assay- The MTT substrate (3-(4,5-dimethylthiazol-2-yl)-2,5-diphenyltetrazolium bromide) prepared in PBS solution was added to the CHO-K1 cells in culture with chemical inhibitors and SPIONs and incubated for 4 hours. Viable cells with active metabolism convert MTT (yellow color) into a formazan product (purple color). The formazan product of the MTT tetrazolium accumulates as an insoluble precipitate. After solubilization of formazan by dimethyl sulfoxide (DMSO), the quantity of formazan was measured by estimating the absorbance at 540 nm wavelength using a spectrophotometer. The dead cells lose the ability to convert MTT into formazan, thus color formation serves as a convenient marker of the viable cells. The ratio of treated and untreated cells gives the cellular viability at different inhibitor concentrations.

Trypan Blue Indicator- Live cells with intact cell membrane do not allow trypan blue stain to enter the cell cytoplasm and appear clear/ translucent, whereas the indicator enters the dead cells and they appear blue in color. Based on hemacytometer counts, the percentage of dead cells and live cells were calculated, thus giving the percentage of cell viability/toxicity.

5.4 Results and Discussion

5.4.1 Cellular Uptake with different inhibitors

Cellular uptake of different inhibitors at different concentrations and their effects on endocytosis were evaluated by measuring magnetophoretic mobilities of the SPION- labeled CHO-K1 cells. The magnetophoretic mobility of the labeled cells is directly proportional to the cellular uptake of SPIONs. Figure 5.2 shows the magnetophoretic mobility of CHO-K1 cells labeled with aminated starch beads and treated with genistein inhibitor at different concentrations. The mobility of untreated SPIONs is high depicting that the uptake is high for untreated beads and the mobility decreased with the increase in genistein concentration from 0 to 100 μM.

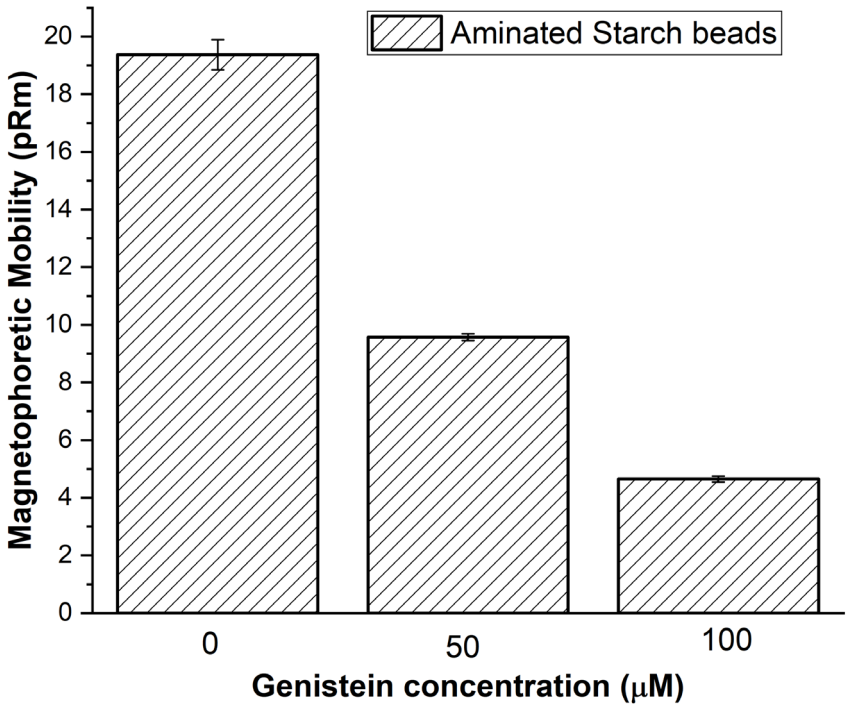

Figure 5.2 - Magnetophoretic mobility of labeled CHO-K1 cells (labeled with aminated starch beads) treated with genistein at different concentrations. The error bars represent standard error of the mobilities.

Table 5.2 - Average control magnetophoretic mobilities and their standard deviations of CHO-K1 cells labeled with 4 different surface functionalized magnetic nanoparticles.

Particle Type	Average control magnetophoretic mobility (pRm)	SD
Dextran Sulfate (DXS)	4.285	0.063
Aminated DXS	4.182	0.135
Starch	5.678	0.157
Aminated starch	19.372	2.173

Table 5.2 gives the average control magnetophoretic mobilities of CHO-K1 cells labeled with different functionalized nanoparticles along with their standard deviations. This data shows the reproducibility and accuracy of the method. The average mobilities were estimated by applying data filters as described in section 5.3.4. The average magnetophoretic mobility of cells labeled with aminated starch beads is high when compared to other magnetic beads, indicating the higher cellular uptake.

The normalized magnetophoretic mobility (expressed as per cent of mobility at zero inhibitor concentration and plotted as "Normal Mobility") of labeled cells with different SPIONs and inhibitors is shown in Figures 5.3 and 5.4. A Marquardt-Levenberg least-squares multiparameter fit was used to fit the non-linear exponential curve with the equation $y = A + ((1-A) \exp(-kx))$, where y is the total fraction of uninhibited endocytosis sites, k is the toxicity of the inhibitor and A is the uninhibited fraction of endocytosis events.

Genistein with a concentration range of 0 to 300 μM (Figure 5.3) and chlorpromazine with a concentration range of 0 to 10 μM (Figure 5.4) were used to inhibit endocytosis of different surface modified SPIONs. The normalized mobilities of cells taking up aminated DXS and starch coated beads and treated with genistein were fitted linearly, as the data did not reach the saturation plateau even beyond the lethal concentration range of 200 μM. The normalized mobilities of dextransulfate and aminated starch beads followed an exponentially decreasing function with the increase in the concentration of genistein. The curve fit parameters are given in Figure 5.3. The cellular uptake (normalized mobility) is decreased for all the beads as the concentration of genistein is increased.

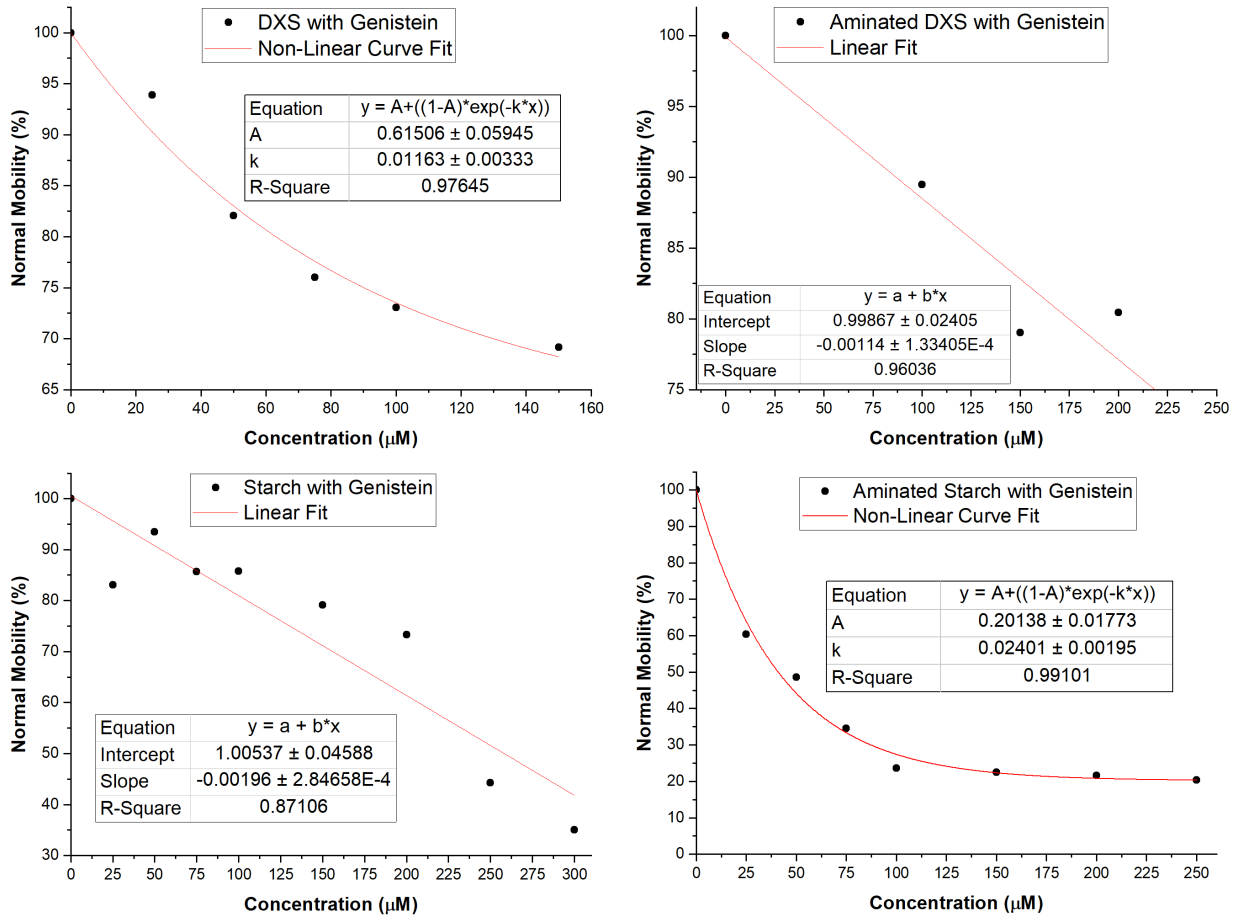

Figure 5.3 - Normalized mobility change of cells labeled with different SPIONs with respect to genistein concentration.

The normalized mobility (cellular uptake) of labeled cells for all the beads with chlorpromazine drug were exponentially decreasing with the increase in the concentration of chlorpromazine hydrochloride. The curve fit parameters are given in Figure 5.4, with $R^2 > 0.9$.

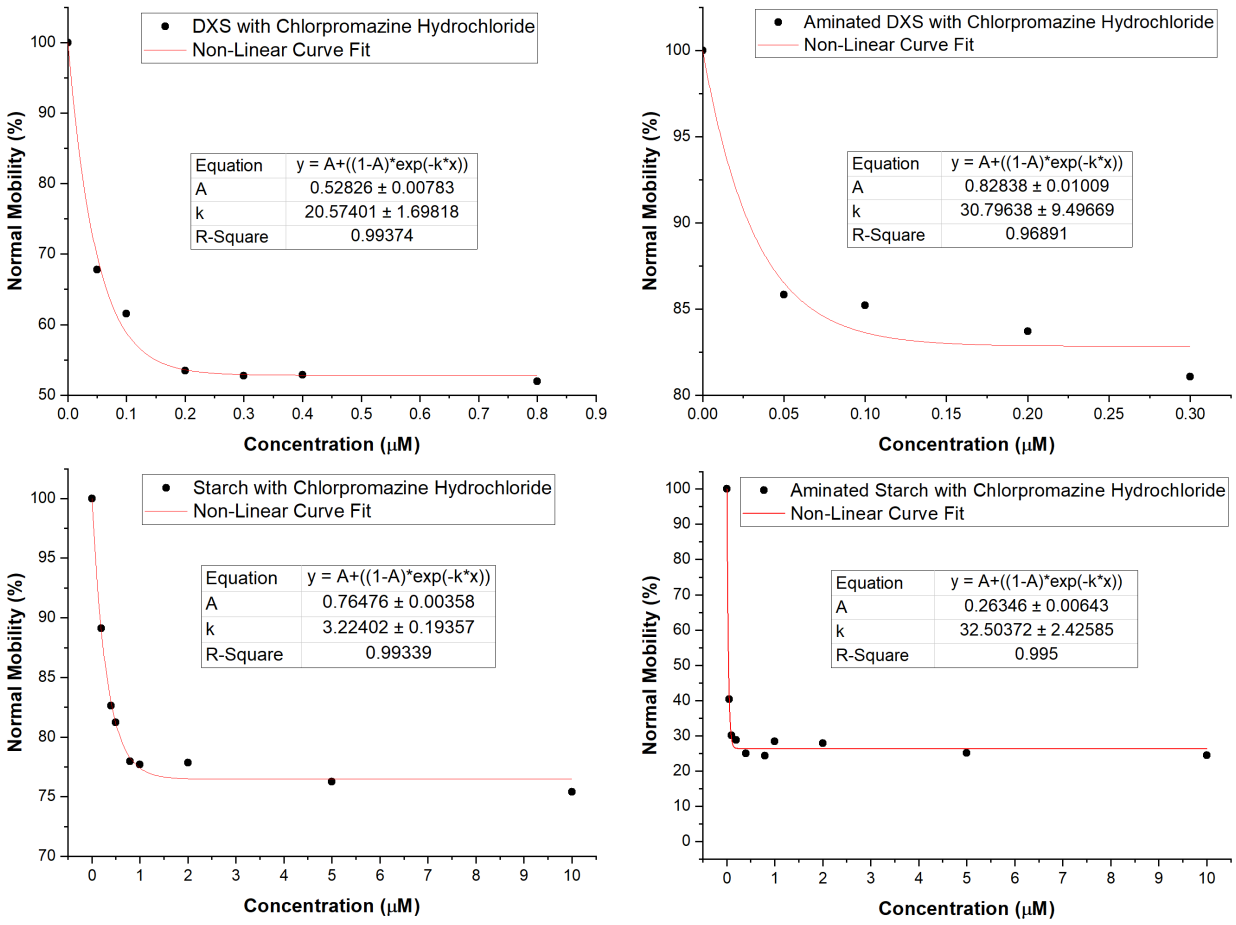

Figure 5.4 - Normalized mobility change of cells labeled with different SPIONs as a function of chlorpromazine hydrochloride concentration.

5.4.2 Inhibitor toxicity and Zeta Potential

The hydrodynamic size, zeta potential, and inhibitor parameters for different SPIONs are given in Table 5.3. The inhibitors toxicity was quantified by the toxicity constant (k) derived from the normalized mobility graphs (Figures 5.3 and 5.4) as shown in Table 5.3 and Figure 5.5. The difference in values of size and zeta potential measured in distilled water (dH_2O) and complete culture media (CM) are due to the presence of balanced salt solution, serum, serum proteins, cationic and anionic species in the cell culture media. The electrostatic interactions of nanoparticles and culture media plays a significant role in protein adsorption and cellular uptake

(Patil et al., 2007). The better cellular uptake and ligand adsorption can be achieved by proper tuning of surface properties of nanoparticles (Vincent et al., 2009).

Table 5.3 - Hydrodynamic size and zeta potential (ZP) measured in distilled water and complete cell culture media along with standard deviations, and inhibitor parameters for different SPIONs.

Particle Type	Size (nm) in dH_2O	Size (nm) in CM	ZP in dH_2O (mV)	ZP in CM (mV)	Inhibitors			
					Genistein		Chlorpromazine	
					k	A	k	A
Dextran Sulfate (DXS)	133.9 ± 1.3	166.5 ± 0.8	-52.93 ± 0.9	-0.975 ± 0.05	0.012	0.615	20.570	0.528
Aminated DXS	164.7 ± 0.6	148.2 ± 0.6	-33.43 ± 0.5	-0.337 ± 0.13	0.001	N/A	30.790	0.828
Starch	108.6 ± 1.4	151.1 ± 0.7	-8.99 ± 0.2	-3.78 ± 0.6	0.002	N/A	3.224	0.765
Aminated Starch	142.7 ± 1.1	128.5 ± 0.5	39.60 ± 0.8	-0.692 ± 0.2	0.024	0.201	32.504	0.264

The maximum inhibition by each inhibitor on each type of bead is estimated by considering (1-A) values in most cases which gives the quantified inhibited endocytosis sites. Table 5.4 shows the approximate maximum % inhibitions.

Table 5.4 - Maximum inhibitions observed (%) for each bead type with different inhibitors.

Bead Type	Genistein	Chlorpromazine	Remaining
DXS	40	48	12
Aminated DXS	22	18	60
Starch	70	24	6
Aminated Starch	80	74	0

For dextransulfate (DXS) beads, the inhibition percentage for genistein (40%) and chlorpromazine (48%) are almost equal. The aminated DXS beads show minimum percent inhibition with both inhibitors indicating that caveolae and clathrin independent and/or micropinocytosis mechanisms are dominant. For starch coated beads maximum inhibition is observed with genistein. For the aminated starch beads both the inhibitors exhibited maximum inhibition indicating that the aminated starch beads undergo both caveolae mediated (80%) and clathrin dependent (74%) endocytosis mechanisms.

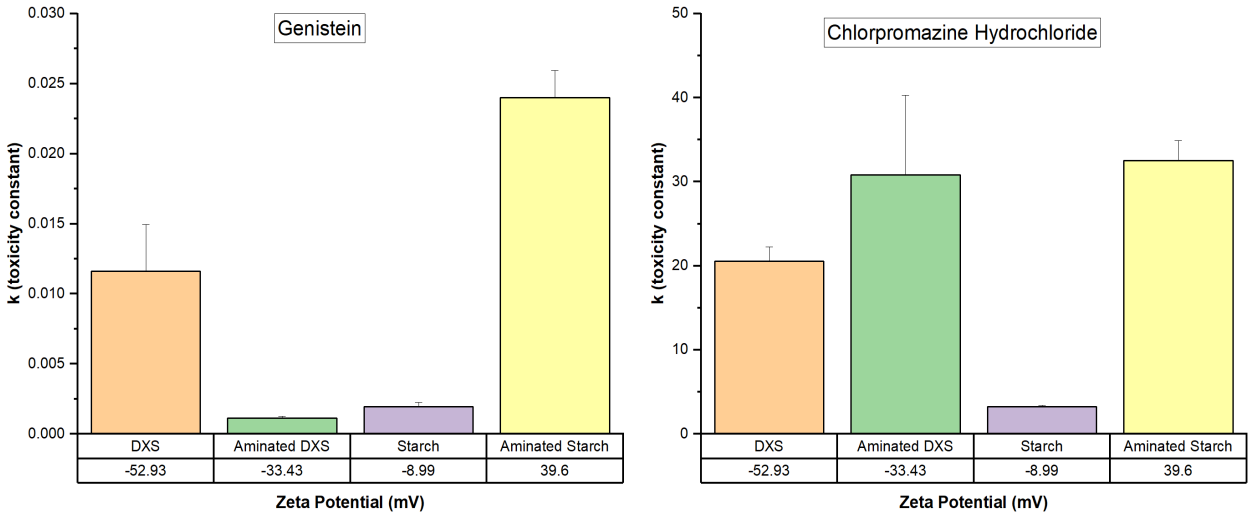

Figure 5.5 - Inhibitor toxicity constant (k) versus zeta potential (ZP in dH_2O) for different SPIONs.

Genistein showed a low toxicity constant (in the order of 0.01 per micromolar) indicating that high doses are required. Chlorpromazine exhibited higher inhibition toxicity (in the order of 10 per micromolar) and was sensitive to low dosages. For both inhibitors, the toxicity toward the uptake of aminated starch beads was high and that of starch beads was low.

5.4.3 Cell Viability with different inhibitors

The viabilities are high in the range of 70 to 90% for both the inhibitors and consistent between two methods- MTT assay and trypan blue indicator (Figures 5.6 and 5.7). However, the viabilities decreased monotonically with the increase in inhibitor concentration (Figure 5.6) agreeing with the literature where genistein with a concentration higher than 20 µM and incubation period of 24 hours, reduced cell viability of mouse embryonic fibroblast cell line (Rucinska et al., 2008).

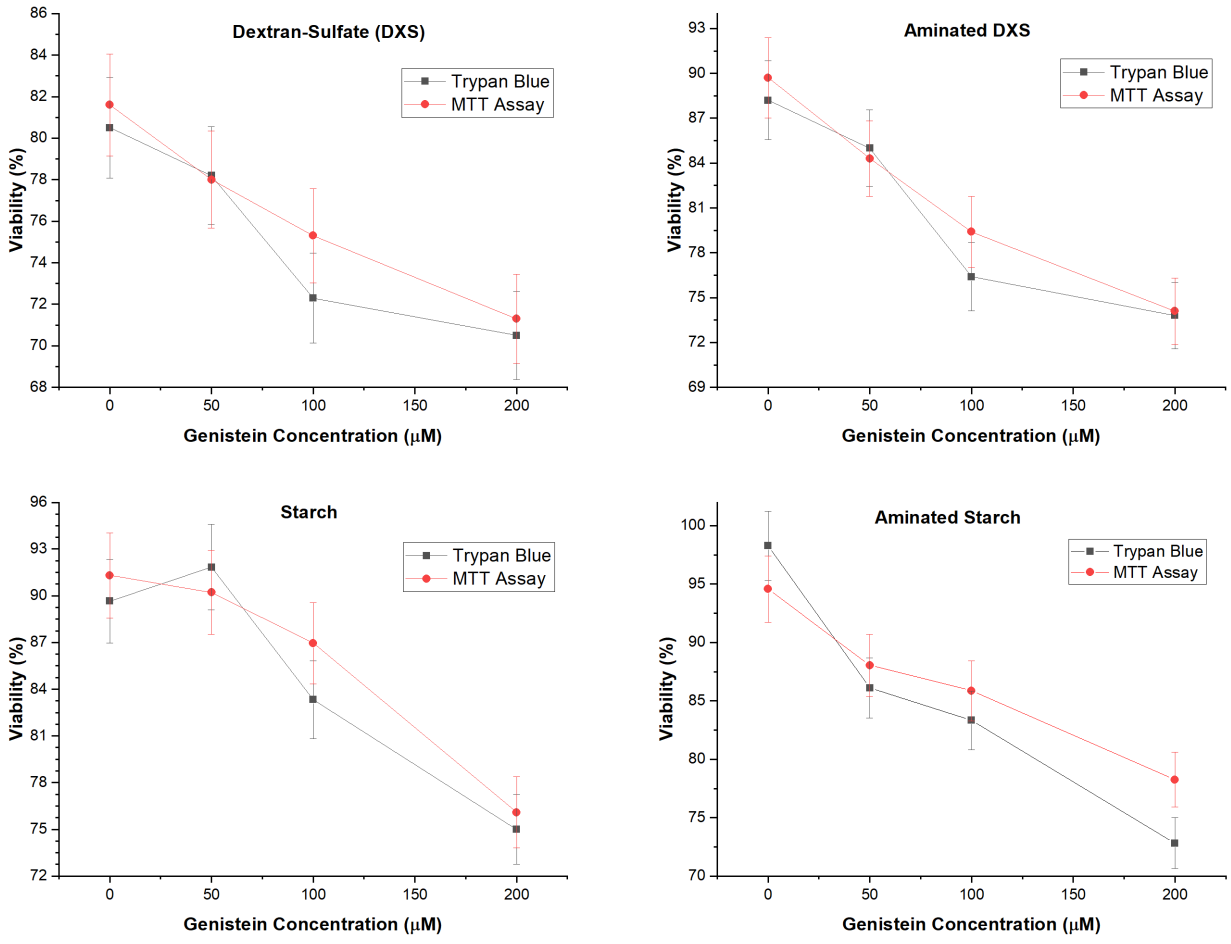

Figure 5.6 - Viability of labeled CHO-K1 cells with different types of SPIONs and genistein estimated by trypan blue indicator and MTT assay.

Genistein-8-C-glucoside (G8CG), at concentrations higher than 10 µM and incubation period of 1 hour significantly reduced cell viability, induced apoptosis and DNA damage in CHO cells. The concentrations higher than 50 µM genestein, has decreased the cell viability to less than 40% (Rucinska et al., 2007). Genistein inhibits glucose uptake, induces apoptosis and autophagocytosis in ovarian cancer cell lines A2780, CaOV3, and ES2 (Gossner et al., 2007).

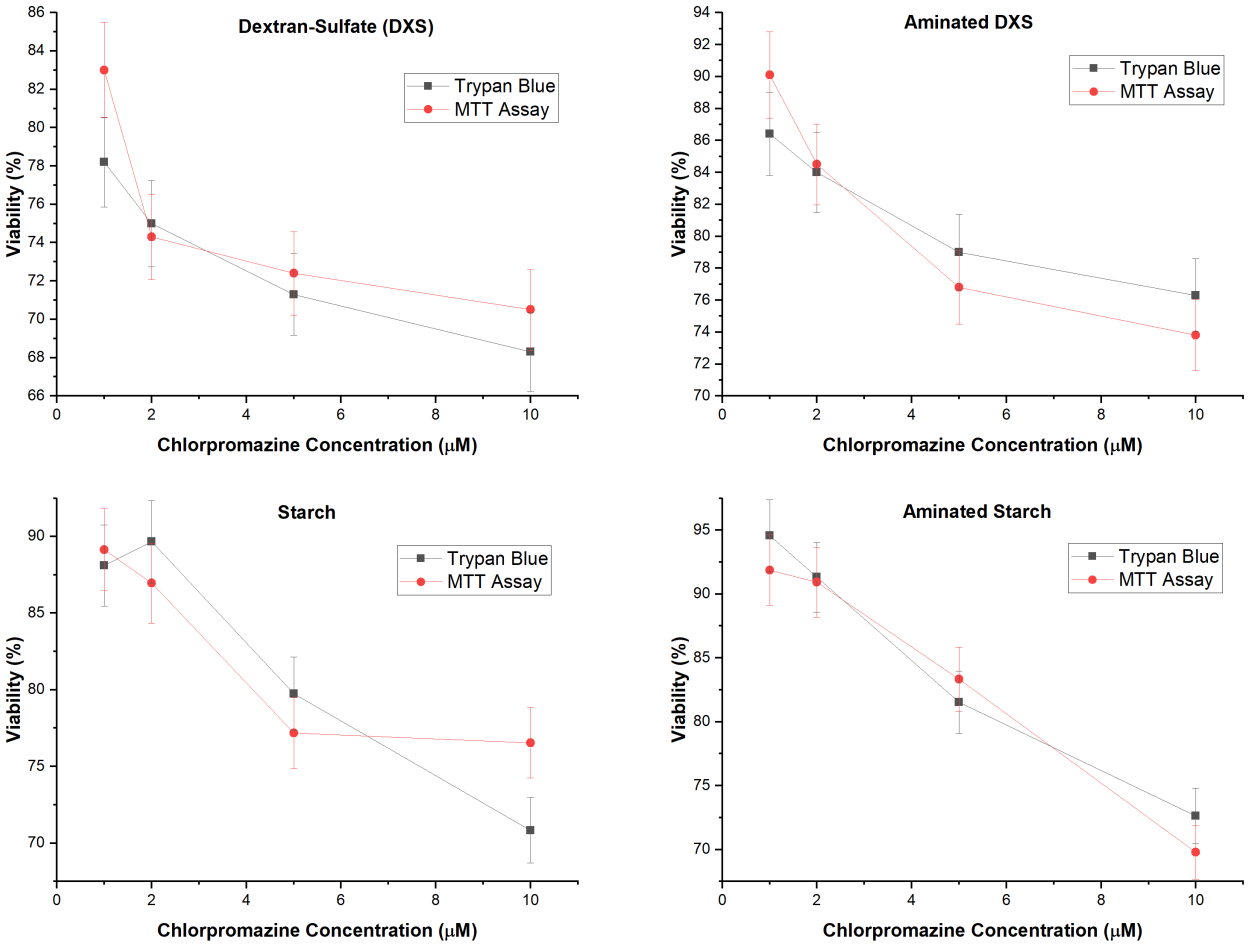

Figure 5.7 - Viability of labeled CHO-K1 cells with different types of SPIONs treated with chlorpromazine hydrochloride estimated by trypan blue indicator and MTT assay.

The percentage of viable cell density of different mammalian cells is decreased by increasing the concentration of genistein from 0.0625 mM to 1 mM (Tian et al., 2020). At high concentrations, 50 to 150 µM (3 hours of incubation period) genistein induced formation of

micronucleus, which indicates the chromosome breakage in Chinese hamster V79 cells (Snyder & Gillies, 2003). Increase in chlorpromazine concentration (>10 µM) decreased cell viability in human neuroblastoma cell line (Abe et al., 1986), and greater than 100 µM concentration is considered highly toxic (Suwalsky et al., 2008).

5.4.4 Effect of both inhibitors

The cellular uptake of cells labeled with aminated starch coated beads was quantified by magnetophoretic mobility measurement by treating the aminated starch labeled CHO-K1 cells with both the inhibitors to examine whether both the inhibitors are targeting same or different endocytosis mechanisms. The concentration of chlorpromazine was held constant at 0.3 µM and the genistein concentration was varied from 0 to 200 µM.

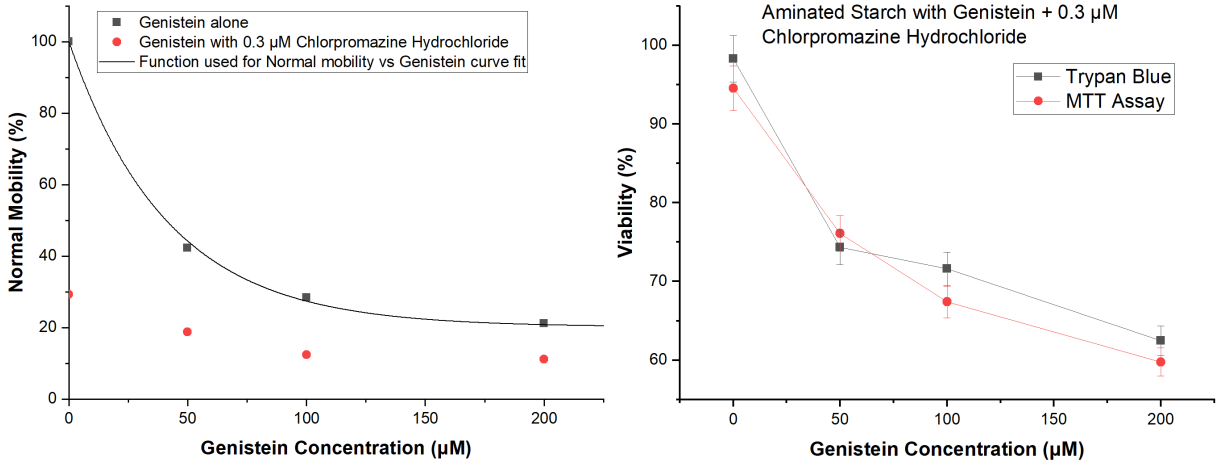

Figure 5.8 - Normalized mobility of CHO-K1 cells labeled with aminated starch beads and treated with genistein + 0.3 µM chlorpromazine hydrochloride and viability of CHO-K1 cells labeled with aminated starch beads and treated with genistein + 0.3 uM chlorpromazine hydrochloride.

The decrease in normal mobility values for the genistein and chlorpromazine experiment (red data points in the left panel of Figure 5.8) when compared to the genistein alone (black data points) experiment reveals that the two inhibitors target and inhibit different endocytosis pathways.

The viability data for these experiments shown in Figure 5.8 are consistent between methods and decrease with the increase in inhibitor concentrations.

5.5 - Mechanisms of Uptake

The magnetic beads with aminated starch and dextran-sulfate coatings exhibited clathrin and caveolae mediated endocytosis as dominant mechanisms. The starch coated beads showed caveolae mediated endocytosis as the major pathway to enter cell membrane. Based on literature, aminated-DXS beads follow a likely clathrin and caveolae independent mechanism as tabulated in Table 5.5.

Table 5.5 - Types of endocytosis mechanisms dominant for different SPIONs.

Particle Type	Endocytosis Mechanism	
	Major/ Dominant	**Minor/ Low to Moderate**
Dextran Sulfate (DXS)	Clathrin & Caveolae mediated	Clathrin & Caveolae independent
Aminated DXS	Clathrin & Caveolae independent	Clathrin dependent & Caveolae mediated
Starch	Caveolae mediated	Clathrin dependent, Clathrin & Caveolae independent
Aminated Starch	Clathrin & Caveolae mediated	Clathrin & Caveolae independent

5.5 Conclusions

SPIONs with different surface modifications were studied and utilized in this research to quantify the cellular uptake of magnetically labeled mammalian (CHO-K1) cells. The toxicity and inhibition rate of the mechanism-based inhibitors was quantified by magnetophoretic mobility

measurement of thousands of magnetically labeled CHO-K1 cells. The two independent parameters- inhibitor toxicity and zeta potential of magnetic beads accountable for the cellular uptake of SPIONs were estimated and discussed to find the types of endocytosis mechanisms dominant for different magnetic beads. The objective of determining how magnetic beads enter cellular cytoplasm was achieved as given in Table 5.5. Thus, characterization of labeled cells and magnetic particles by magnetic velocimetry facilitates the optimization of SPIONs coatings, a better understanding of cell labeling, and the evaluation of the role of different cellular endocytosis mechanisms.

Acknowledgments

Research support was provided by Auburn University Research Funding. We thank Dr. Allan E. David and his research group for providing cell culture training and lab facility.

References

Abe, K., Sekizawa, T., & Kogure, K. (1986). Biphasic effects of chlorpromazine on cell viability in a neuroblastoma cell line. *Neuroscience Letters*, *71*(3), 335–339. https://doi.org/https://doi.org/10.1016/0304-3940(86)90643-9.

Ahlberg, S., Antonopulos, A., Diendorf, J., Dringen, R., Epple, M., Flöck, R., Goedecke, W., Graf, C., Haberl, N., & Helmlinger, J. (2014). PVP-coated, negatively charged silver nanoparticles: A multi-center study of their physicochemical characteristics, cell culture and in vivo experiments. *Beilstein Journal of Nanotechnology*, *5*(1), 1944–1965.

Akiyama, T., & Ogawara, H. (1991). [30] Use and specificity of genistein as inhibitor of protein-tyrosine kinases. In *Methods in enzymology* (Vol. 201, pp. 362–370). Elsevier.

Anani, T. (2018). *Matrix Metalloproteinase-Responsive Superparamagnetic Iron Oxide Nanoparticles (SPIONs) to Distinguish Between Aggressive and Indolent Cancer*.

Chen, H., Abolmatty, A., & Faghri, M. (2011). Microfluidic inverse phase ELISA via manipulation of magnetic beads. *Microfluidics and Nanofluidics*, *10*(3), 593–605.

Chertok, B., Moffat, B. A., David, A. E., Yu, F., Bergemann, C., Ross, B. D., & Yang, V. C. (2008). Iron oxide nanoparticles as a drug delivery vehicle for MRI monitored magnetic targeting of brain tumors. *Biomaterials*, *29*(4), 487–496.

Church, M. K., & Young, K. D. (1983). The characteristics of inhibition of histamine release from human lung fragments by sodium cromoglycate, salbutamol and chlorpromazine. *British Journal of Pharmacology*, *78*(4), 671–679.

Cole, A. J., David, A. E., Wang, J., Galbán, C. J., Hill, H. L., & Yang, V. C. (2011). Polyethylene glycol modified, cross-linked starch-coated iron oxide nanoparticles for enhanced magnetic tumor targeting. *Biomaterials*, *32*(8), 2183–2193. https://doi.org/10.1016/j.biomaterials.2010.11.040.

Damm, E.-M., Pelkmans, L., Kartenbeck, J., Mezzacasa, A., Kurzchalia, T., & Helenius, A. (2005). Clathrin- and caveolin-1-independent endocytosis: entry of simian virus 40 into cells devoid of caveolae. *The Journal of Cell Biology*, *168*(3), 477–488. https://doi.org/10.1083/jcb.200407113.

De Wilde, A. H., Jochmans, D., Posthuma, C. C., Zevenhoven-Dobbe, J. C., Van Nieuwkoop, S., Bestebroer, T. M., Van Den Hoogen, B. G., Neyts, J., & Snijder, E. J. (2014). Screening of an FDA-approved compound library identifies four small-molecule inhibitors of Middle East respiratory syndrome coronavirus replication in cell culture. *Antimicrobial Agents and Chemotherapy*, *58*(8), 4875–4884.

Dutta, D., & Donaldson, J. G. (2012). *Intended specificity and unintended consequences*. *December*, 203–208.

Dyall, J., Coleman, C. M., Hart, B. J., Venkataraman, T., Holbrook, M. R., Kindrachuk, J., Johnson, R. F., Olinger, G. G., Jahrling, P. B., & Laidlaw, M. (2014). Repurposing of clinically developed drugs for treatment of Middle East respiratory syndrome coronavirus infection. *Antimicrobial Agents and Chemotherapy*, *58*(8), 4885–4893.

Eberbeck, D., Wiekhorst, F., Wagner, S., & Trahms, L. (2011). How the size distribution of magnetic nanoparticles determines their magnetic particle imaging performance. *Applied Physics Letters*, *98*(18), 1–4. https://doi.org/10.1063/1.3586776.

Gazeau, F., Lévy, M., & Wilhelm, C. (2008). Optimizing magnetic nanoparticle design for nanothermotherapy. *Nanomedicine*, *3*(6), 831–844. https://doi.org/10.2217/17435889.3.6.831.

Gossner, G., Choi, M., Tan, L., Fogoros, S., Griffith, K. A., Kuenker, M., & Liu, J. R. (2007). Genistein-induced apoptosis and autophagocytosis in ovarian cancer cells. *Gynecologic Oncology*, *105*(1), 23–30. https://doi.org/10.1016/j.ygyno.2006.11.009.

Gupta, A. K., & Gupta, M. (2005). Cytotoxicity suppression and cellular uptake enhancement of surface modified magnetic nanoparticles. *Biomaterials*, *26*(13), 1565–1573.

Hanot, C. C., Choi, Y. S., Anani, T. B., Soundarrajan, D., & David, A. E. (2015). Effects of iron-oxide nanoparticle surface chemistry on uptake kinetics and cytotoxicity in CHO-K1 cells. *International Journal of Molecular Sciences*, *17*(1), 1–15. https://doi.org/10.3390/ijms17010054.

Hathaway, H. J., Butler, K. S., Adolphi, N. L., Lovato, D. M., Belfon, R., Fegan, D., Monson, T. C., Trujillo, J. E., Tessier, T. E., & Bryant, H. C. (2011). Detection of breast cancer cells using targeted magnetic nanoparticles and ultra-sensitive magnetic field sensors. *Breast Cancer Research*, *13*(5), R108.

Hsiao, Y., Peng, S., Lai, K., Liao, C., Huang, Y., Lin, C., Lin, M., Liu, K., Tsai, C., & Ma, Y. (2019). Genistein induces apoptosis in vitro and has antitumor activity against human leukemia HL-60 cancer cell xenograft growth in vivo. *Environmental Toxicology*, *34*(4), 443–456.

Inoue, Y., Tanaka, N., Tanaka, Y., Inoue, S., Morita, K., Zhuang, M., Hattori, T., & Sugamura, K. (2007). Clathrin-dependent entry of severe acute respiratory syndrome coronavirus into target cells expressing ACE2 with the cytoplasmic tail deleted. *Journal of Virology*, *81*(16), 8722–8729.

Jeong, A., & Lim, H. B. (2018). Magnetophoretic separation ICP-MS immunoassay using Cs-doped multicore magnetic nanoparticles for the determination of salmonella typhimurium. *Talanta*, *178*, 916–921.

Jie, G., Yang, L., & Jinghai, Y. (2010). Influence of Co-Doping on Synthesis, Structure and Magnetic Properties of Ni Nanoparticles. *Rare Metal Materials and Engineering*, *39*, 328–331.

Jing, Y., Mal, N., Williams, P. S., Mayorga, M., Penn, M. S., Chalmers, J. J., & Zborowski, M. (2008). Quantitative intracellular magnetic nanoparticle uptake measured by live cell magnetophoresis. *The FASEB Journal*, *22*(12), 4239–4247.

Kala, M., Bajaj, K., & Sinha, S. (1997). Magnetic Bead Enzyme-Linked Immunosorbent Assay (ELISA) Detects Antigen-Specific Binding by Phage-Displayed scFv Antibodies That Are Not Detected with Conventional ELISA. *Analytical Biochemistry*, *254*(2), 263–266. https://doi.org/https://doi.org/10.1006/abio.1997.2378.

Kim, J.-E., Shin, J.-Y., & Cho, M.-H. (2012). Magnetic nanoparticles: an update of application for drug delivery and possible toxic effects. *Archives of Toxicology*, *86*(5), 685–700.

https://doi.org/10.1007/s00204-011-0773-3.

Kiselev, M. V, Gladilin, A. K., Melik-Nubarov, N. S., Sveshnikov, P. G., Miethe, P., & Levashov, A. V. (1999). Determination of cyclosporin A in 20% ethanol by a magnetic beads-based immunofluorescence assay. *Analytical Biochemistry*, *269*(2), 393–398.

Kiss, A. L., & Botos, E. (2009). Endocytosis via caveolae: Alternative pathway with distinct cellular compartments to avoid lysosomal degradation? *Journal of Cellular and Molecular Medicine*, *13*(7), 1228–1237. https://doi.org/10.1111/j.1582-4934.2009.00754.x.

Knežević, N. Ž., & Lin, V. S.-Y. (2013). A magnetic mesoporous silica nanoparticle-based drug delivery system for photosensitive cooperative treatment of cancer with a mesopore-capping agent and mesopore-loaded drug. *Nanoscale*, *5*(4), 1544–1551.

Lee, B., Yoo, J. S., Ogay, V., Kim, K. W., Dobberstein, H., Soh, K., & Chang, B. (2007). Electron microscopic study of novel threadlike structures on the surfaces of mammalian organs. *Microscopy Research and Technique*, *70*(1), 34–43.

Liao, T., Yuan, F., Yu, H., & Li, Z. (2016). An ultrasensitive ELISA method for the detection of procalcitonin based on magnetic beads and enzyme-antibody labeled gold nanoparticles. *Analytical Methods*, *8*(7), 1577–1585.

Liu, Q., Xia, S., Sun, Z., Wang, Q., Du, L., Lu, L., & Jiang, S. (2015). Testing of Middle East respiratory syndrome coronavirus replication inhibitors for the ability to block viral entry. *Antimicrobial Agents and Chemotherapy*, *59*(1), 742–744.

Lundkvist, Å., Hörling, J., Athlin, L., Rosén, A., & Niklasson, B. (1993). Neutralizing human monoclonal antibodies against Puumala virus, causative agent of nephropathia epidemica: a novel method using antigen-coated magnetic beads for specific B cell isolation. *Journal of General Virology*, *74*(7), 1303–1310.

Mahmoudi, M., Sant, S., Wang, B., Laurent, S., & Sen, T. (2011). Superparamagnetic iron oxide nanoparticles (SPIONs): Development, surface modification and applications in chemotherapy. *Advanced Drug Delivery Reviews*, *63*(1), 24–46. https://doi.org/https://doi.org/10.1016/j.addr.2010.05.006.

Momattin, H., Al-Ali, A. Y., & Al-Tawfiq, J. A. (2019). A Systematic Review of therapeutic agents for the treatment of the Middle East Respiratory Syndrome Coronavirus (MERS-CoV). *Travel Medicine and Infectious Disease*, *30*, 9–18. https://doi.org/https://doi.org/10.1016/j.tmaid.2019.06.012.

Nguyen, A. H., Abdelrasoul, G. N., Lin, D., Maadi, H., Tong, J., Chen, G., Wang, R., Anwar, A., Shoute, L., & Fang, Q. (2018). Polyethylenimine-coated iron oxide magnetic nanoparticles for high efficient gene delivery. *Applied Nanoscience*, *8*(4), 811–821.

Oliva, C. R., Zhang, W., Langford, C., Suto, M. J., & Griguer, C. E. (2017). Repositioning chlorpromazine for treating chemoresistant glioma through the inhibition of cytochrome c oxidase bearing the COX4-1 regulatory subunit. *Oncotarget*, *8*(23), 37568–37583. https://doi.org/10.18632/oncotarget.17247.

Otręba, M., Kośmider, L., & Rzepecka-Stojko, A. (2020). Antiviral activity of chlorpromazine, fluphenazine, perphenazine, prochlorperazine, and thioridazine towards RNA-viruses. A review. *European Journal of Pharmacology*, 173553.

Patil, S., Sandberg, A., Heckert, E., Self, W., & Seal, S. (2007). Protein adsorption and cellular uptake of cerium oxide nanoparticles as a function of zeta potential. *Biomaterials*, *28*(31), 4600–4607. https://doi.org/10.1016/j.biomaterials.2007.07.029.

Pavese, J. M., Farmer, R. L., & Bergan, R. C. (2010). Inhibition of cancer cell invasion and metastasis by genistein. *Cancer and Metastasis Reviews*, *29*(3), 465–482.

https://doi.org/10.1007/s10555-010-9238-z.

Prijic, S., Scancar, J., Romih, R., Cemazar, M., Bregar, V. B., Znidarsic, A., & Sersa, G. (2010). Increased Cellular Uptake of Biocompatible Superparamagnetic Iron Oxide Nanoparticles into Malignant Cells by an External Magnetic Field. *The Journal of Membrane Biology*, *236*(1), 167–179. https://doi.org/10.1007/s00232-010-9271-4.

Rucinska, A., Kirko, S., & Gabryelak, T. (2007). Effect of the phytoestrogen, genistein-8-C-glucoside, on Chinese hamster ovary cells in vitro. *Cell Biology International*, *31*(11), 1371–1378. https://doi.org/10.1016/j.cellbi.2007.05.012.

Rucinska, A., Roszczyk, M., & Gabryelak, T. (2008). Cytotoxicity of the isoflavone genistein in NIH 3T3 cells. *Cell Biology International*, *32*(8), 1019–1023. https://doi.org/10.1016/j.cellbi.2008.04.004.

Sahay, G., Alakhova, D. Y., & Kabanov, A. V. (2010). Endocytosis of nanomedicines. *Journal of Controlled Release*, *145*(3), 182–195.

Sannidhi, A., Todd, P. W., & Hanley, T. R. (2019). Estimation of Intrinsic Magnetic Properties of Single Particles by Particle Tracking Velocimetry. *IEEE Magnetics Letters*, 1. https://doi.org/10.1109/LMAG.2019.2950298.

Snyder, R. D., & Gillies, P. J. (2003). Reduction of genistein clastogenicity in Chinese hamster V79 cells by daidzein and other flavonoids. *Food and Chemical Toxicology*, *41*(10), 1291–1298.

Strojan, K., Lojk, J., Bregar, V. B., Veranič, P., & Pavlin, M. (2017). Glutathione reduces cytotoxicity of polyethyleneimine coated magnetic nanoparticles in CHO cells. *Toxicology in Vitro*, *41*, 12–20.

Suwalsky, M., Villena, F., Sotomayor, C. P., Bolognin, S., & Zatta, P. (2008). Human cells and

cell membrane molecular models are affected in vitro by chlorpromazine. *Biophysical Chemistry*, *135*(1), 7–13. https://doi.org/https://doi.org/10.1016/j.bpc.2008.02.014.

Thangavel, P., Puga-Olguín, A., Rodríguez-Landa, J. F., & Zepeda, R. C. (2019). Genistein as potential therapeutic candidate for menopausal symptoms and other related diseases. *Molecules*, *24*(21), 3892.

Tian, J., Xu, J., & He, Q. (2020). Compositions for cell culture and methods of using the same. *U.S. Patent No. 10,590,457*. Washington, DC: U.S. Patent and Trademark Office.

Traganos, F., Ardelt, B., Halko, N., Bruno, S., & Darzynkiewicz, Z. (1992). Effects of Genistein on the Growth and Cell Cycle Progression of Normal Human Lymphocytes and Human Leukemic MOLT-4 and HL-60 Cells. *Cancer Research*, *52*(22), 6200–6208.

Vercauteren, D., Vandenbroucke, R. E., Jones, A. T., Rejman, J., Demeester, J., De Smedt, S. C., Sanders, N. N., & Braeckmans, K. (2010). The use of inhibitors to study endocytic pathways of gene carriers: Optimization and pitfalls. *Molecular Therapy*, *18*(3), 561–569. https://doi.org/10.1038/mt.2009.281.

Vincent, A., Babu, S., Heckert, E., Dowding, J., Hirst, S. M., Inerbaev, T. M., Self, W. T., Reilly, C. M., Masunov, A. E., Rahman, T. S., & Seal, S. (2009). Protonated Nanoparticle Surface Governing Ligand Tethering and Cellular Targeting. *ACS Nano*, *3*(5), 1203–1211. https://doi.org/10.1021/nn9000148.

Williams, P. S., Zborowski, M., & Chalmers, J. J. (1999). Flow rate optimization for the quadrupole magnetic cell sorter. *Analytical Chemistry*, *71*(17), 3799–3807. https://doi.org/10.1021/ac990284+.

Xu, S., Olenyuk, B. Z., Okamoto, C. T., & Hamm-Alvarez, S. F. (2013). Targeting receptor-mediated endocytotic pathways with nanoparticles: rationale and advances. *Advanced Drug*

Delivery Reviews, *65*(1), 121–138. https://doi.org/10.1016/j.addr.2012.09.041.

Yoffe, S., Leshuk, T., Everett, P., & Gu, F. (2013). Superparamagnetic iron oxide nanoparticles (SPIONs): synthesis and surface modification techniques for use with MRI and other biomedical applications. *Current Pharmaceutical Design*, *19*(3), 493–509.

Yu, F., Zhang, L., Huang, Y., Sun, K., David, A. E., & Yang, V. C. (2010). The magnetophoretic mobility and superparamagnetism of core-shell iron oxide nanoparticles with dual targeting and imaging functionality. *Biomaterials*, *31*(22), 5842–5848.

Zborowski, M., & Chalmers, J. J. (2011). *Magnetic cell separation* (Vol. 32). Elsevier.

Zhou, C. (2017). Characterization and Quantification of Magnetic Particles and Magnetically Labeled Cells by Magnetic Cytometry. *Auburn University Dissertations.*

Zhou, C., Boland, E. D., Todd, P. W., & Hanley, T. R. (2016). Magnetic particle characterization—magnetophoretic mobility and particle size. *Cytometry Part A*, *89*(6), 585–593. https://doi.org/10.1002/cyto.a.22866.

Zhou, C., Choi, Y. S., David, A. E., Todd, P. W., & Hanley, T. R. (2018). Nanomaterial endocytosis: Estimation of particles per cell by magnetic measurement. *IEEE Magnetics Letters*, *9*, 7–11. https://doi.org/10.1109/LMAG.2018.2830754.

Zhou, C., Qian, Z., Choi, Y. S., David, A. E., Todd, P., & Hanley, T. R. (2017). Application of magnetic carriers to two examples of quantitative cell analysis. *Journal of Magnetism and Magnetic Materials*, *427*(November 2016), 25–28. https://doi.org/10.1016/j.jmmm.2016.11.009.

Zhou, J., Zhang, J., David, A. E., & Yang, V. C. (2013). Magnetic tumor targeting of β-glucosidase immobilized iron oxide nanoparticles. *Nanotechnology*, *24*(37), 375102. https://doi.org/10.1088/0957-4484/24/37/375102.

Chapter 6 - Summary

Magnetic characterization is of much importance in the fields of cell labeling, cell purification, cell physiology, endocytosis, biochemical micro assays, endosome research, cell separation, drug targeting and in vivo diagnostics. A particle tracking velocimeter is utilized to measure magnetophoretic mobility, size and other morphological parameters of magnetic particles and magnetically labeled cells.

The calibration capability of the instrument has been extended by generating linear calibration curves in order to estimate the actual particle size and thereby estimate the intrinsic magnetic properties of several commercially available magnetic beads on a particle-by-particle basis. The quality of the magnetic beads can be assessed using the regression coefficient (R^2) values of the two-parameter curves between diameter and apparent magnetic susceptibility or saturation magnetization distributions (Sannidhi et al., 2019). Different approaches were explored, such as optical density methods and chain velocity methods, to estimate the magnetophoretic mobility of a single nanoparticle in a chain. The rapid estimation of magnetophoretic mobility by the instrument and collection of multiple thousands of data points facilitates cellular uptake quantification and kinetic studies in less time than any other existing technique (Zhou, 2017).

Magnetic cytometry by velocimetry records the motion of labeled cells in an isodynamic magnetic field thereby estimating a key parameter, magnetophoretic mobility of labeled cells. The receptor-independent uptake by cultured Chinese Hamster Ovary (CHO-K1) cells of 100 nm iron oxide nanoparticles with different surface coatings, namely starch, dextran-sulfate and amino groups was studied to reveal the role of nanoparticle endocytosis mechanisms. Caveolae-mediated, clathrin-dependent and independent endocytosis mechanisms were revealed by using specific mechanism-based inhibitors- genistein and chlorpromazine hydrochloride respectively.

The surface charge of the particle and inhibitors of specific uptake mechanisms are the important factors that impact the process of cellular endocytosis. The cellular survival rate/viability, inhibitor toxicity and uptake of different nanoparticles have been investigated. This research facilitates the rapid estimation of intrinsic magnetic properties, the optimization of SPIONs surface coatings and a better understanding of cell internal labeling and different cellular endocytosis mechanisms.

Magnetic cytometry by particle tracking velocimetry provides new opportunities for the application of magnetic carriers to safe and efficient cell therapeutics. The optimization of cell labeling systems can be achieved for a specific application by controlling the magnetic particle size, surface functionalization, rate of cellular uptake, phagocytosis kinetics and roles of endocytosis mechanisms by a time-efficient and cost-effective method.

References

Sannidhi, A., Todd, P. W., & Hanley, T. R. (2019). Estimation of Intrinsic Magnetic Properties of Single Particles by Particle Tracking Velocimetry. *IEEE Magnetics Letters*, 1. https://doi.org/10.1109/LMAG.2019.2950298

Zhou, C. (2017). Characterization and Quantification of Magnetic Particles and Magnetically Labeled Cells by Magnetic Cytometry. Auburn University Dissertations.

APPENDIX A - Temperature Dependency of Magnetic Particle Characterization by Particle Tracking Velocimetry

Isothermal conditions are required for the correct operation of the velocimeter because thermal gradients can cause non-magnetic flows to set in. Non-magnetic particles have significant (high) mobility when injected as a hot sample (some 40 to 60^{o}C above ambient temperature). It should be noted that the original sample observation channel cell is not thermostated.

The magnetophoretic mobility of non-magnetic beads (Estapor beads, 5 μm in size) has been analyzed at different sample temperature conditions: hot, ambient and cold. The mobility of non-magnetic beads is almost zero, but the instrument reported high mobility at hot and cold temperature conditions. We tested the hypothesis that the differences in the temperature of bead suspensions and glass channel cell resulted in Marangoni flow, or thermo-capillary convection, which is driven by an interfacial-tension gradient. To study the effect of the hot-sample temperature condition, we conducted three bead experiments: (1) sample and channel cell at room temperature, (2) sample at 98^{o}C and channel cell at 50^{o}C, (3) sample and channel cell at 50^{o}C. Only under condition (2) did the non-magnetic beads show mobility.

When the sample cell was thermostated at 50^{o}C and a sample that was heated to 98^{o}C was immediately subjected to mobility analysis, the mobility histogram as shown in Figure A-1(A) was obtained indicating mobility around 25 pRm, which corresponds to highly magnetic beads, but when both sample and cell were thermostated at 50^{o}C (isothermal conditions) a typical mobility histogram for non-magnetic beads was produced. Thus, increased temperature *per se* does not induce anomalous motion; a temperature *gradient* is required. Two explanations for this temperature-gradient-induced result were explored: thermocapillary flow and thermal contraction during heat loss.

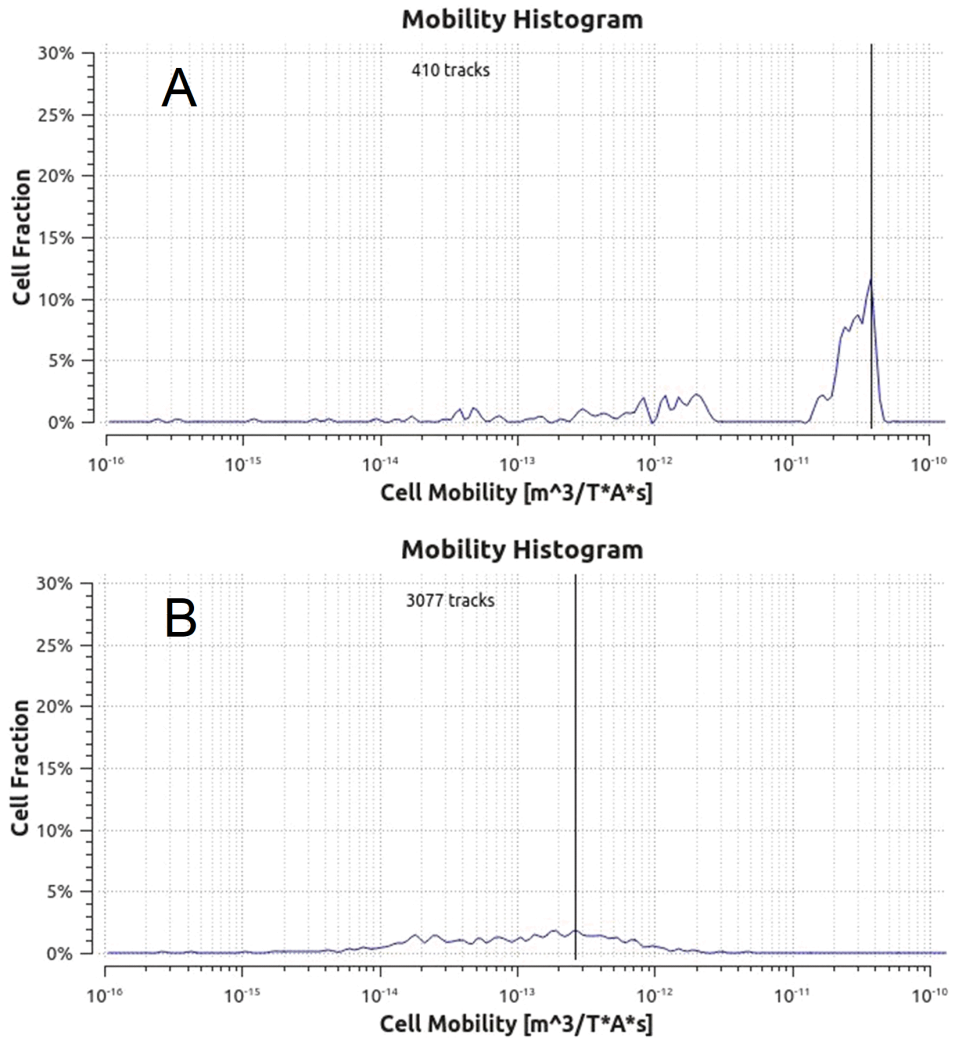

Figure A-1 - Magnetophoretic mobility histogram for Estapor 5 µm non-magnetic beads **(A)** injected as a sample in the water at 98°C into a thermostated cell at 50°C and **(B)** injected as a sample in the water at 50°C into a thermostated cell at 50°C.

Hypothesis 1:

First, we investigated the explanation of such motion by thermocapillary (Marangoni) flow. After several steps of derivation, the velocity equation for our geometry looks like

$$v_{xmax} = \frac{1}{\eta} \cdot \frac{d\sigma}{dT} \cdot \frac{\Delta T}{l} \cdot h \qquad \text{(A-1)}$$

Substituting variables in CGS units

$\eta = 0.01\ \frac{dyn\ .\ s}{cm^2}$, the viscosity of water

$\frac{d\sigma}{dT} = 0.11\ \frac{dyn}{cm\ .\ ℃}$, the temperature dependence of water-glass interfacial tension, which was calculated from published thermo-physical data

$\Delta T = 20℃$, a rough estimate for injecting 98ºC water into 50ºC sample cell with a little cooling time

$l = 3\ cm$, length of the channel cell

$h = 0.03\ cm$, the thickness of the channel cell

This combination gives $\boldsymbol{v_{xmax} = 2\ \frac{cm}{s}}$

Several problems exist with this hypothesis. The above equation A-1 applies to a free "upper" surface – an air-water interface. Even by substituting interfacial tension for surface tension the velocity still applies only to a free surface. The glass surface will not move or deform. In our closed system, if there were thermocapillary crawl along the front and back walls of the cell mass conservation would require a return flow in the reverse direction, but we observed particle movement from left to right only. Furthermore, 2 cm/sec is much faster than can be observed in the velocimeter. One research group successfully performed this same experiment with the open-ended flow and particle tracking by providing a film of air or oil between the water and solid surface and obtaining a flow of 1 mm/sec with a 1.75ºC/cm gradient in 0.4 mm microfluidic channels (Amador et al., 2018). Others conducted similar experiments but the upper surface was in contact with air (Song et al., 2018) and used poly(dimethylsiloxane) (Mondal et al., 2015).

As the observed particle velocity was not consistent with the predictions of thermo-capillary flow, so a contractile-flow hypothesis was tested as explained below.

Hypothesis 2

An alternative explanation is the thermal contraction of the incoming sample as it is being cooled. As a sample of 98ºC water enters into 50ºC water from the right end of the cell it displaces the cool water and loses heat to the walls of the cell as it flows in, leaving, reasonably, a higher temperature on the right end, where the walls experienced more pre-heating by the inflow. Where there is more heat there is expanded volume, but cooling is still occurring during the 2-sec "set" recording, so there is more thermal contraction on the right than on the left. We are making observations at the center of the cell, so the volume of water to the right will be half the cell volume. A linear velocity of contraction can be estimated from

$$v_{xcon} = \frac{C_E \Delta T}{\tau} \frac{L}{2} \qquad \text{(A-2)}$$

where $C_E = 6 * 10^{-4}\ ℃^{-1}$, coefficient of volumetric expansion of water at 80ºC

$\Delta T = 20℃$, estimated temperature drop while the sample is in the cell for measurement

$\tau = 2\ s$, the period during which a sample is in the channel cell for measurement

$L = 3.0\ cm$, length of sample channel cell

This combination (based on estimates) gives $\boldsymbol{v_{xcon} \approx 90\ \mu m/s.}$

We compare these velocities with a particle apparent magnetic velocity derived from Figure A-1(A), using

$$v_{mag} = \frac{U_m S_m}{\mu_o} \quad \text{(A-3)}$$

where U_m = 2.5 x 10^{-11} m^3/T.A. s (25 pRm), magnetophoretic mobility calculated by velocimeter

S_m = 8.6 T^2/m, velocimeter magnet gradient force

μ_o = 4π x 10^{-7} T m/A, magnetic permeability of free space

This combination gives $\boldsymbol{v_{mag}}$ **= 170 µm/s.**

The observed velocity is much closer to the estimated thermal-contraction velocity (Hypothesis 2, 90 µm/s) than it is to the calculated thermocapillary velocity (Hypothesis 1, 2 cm/s). Thus, so far, the best explanation for the observed unexpected mobility of non-magnetic particles is the thermal contraction of the hot water as it cools upon entering the right end of the sample cell.

Finally, to find whether this explanation is feasible in terms of the required cooling rate, the sensible heat lost at ΔT = 20 ºC in a time of Δt =2 s is determined from

$$\Delta H = mc_p \Delta T \quad \text{(A-4)}$$

for m = 0.024 g water, c_p = 4.16 J/gºC, ΔT = 20 ºC,

so ΔH = *2.0* J, and $\Delta H/\Delta t$ = 1.0 J/s

To find whether this heat transfer rate be matched by thermal conductivity through 0.04 mm thickness of the glass, the heat transfer rate is estimated, given by

$$\frac{\Delta H}{\Delta t} = qA = kA\left(\frac{\Delta T}{\Delta X}\right) \quad \text{(A-5)}$$

For $k = 0.01\ \frac{J}{cm\,.\,s.\,℃}$, the thermal conductivity of glass,

$A = 0.6\ cm^2$, transfer area of the half channel cell,

$\Delta T = 20℃$ between inner and outer glass surfaces,

$\Delta x = 0.04\ cm$, glass wall thickness.

This gives $\Delta H/\Delta t$ = 3.0 J/s, more than enough heat transfer rate to account for the required sensible heat loss.

The observed particle velocity, about 100 μm/s was found consistent with the predicted rate of water-cooling during contraction and the calculated heat-transfer rate. This resulted in the entire particle suspension movement, and therefore significant mobility is being recorded by the instrument.

This data indicates the importance of isothermal conditions for measuring magnetophoretic mobility by particle tracking velocimetry. The sample and cell must both be at ambient or thermostated to a single temperature before injecting the sample into the cell. It was originally thought that thermostating a magnetophoresis cell would be unnecessary since the particles and the field do not generate sensible heat. Electrophoresis cells are always thermostated because the application of an electric field to an electrolyte solution produces thermal gradients that distort electrophoretic velocities.

Conclusions

In conclusion, this study indicates the importance of isothermal conditions for measuring magnetophoretic mobility by particle tracking velocimetry. The sample and channel cell must both be at ambient temperature or thermostated to a single temperature before injecting the sample into the channel cell to achieve optimal results which specify the particle quality accurately. For the hypothesis of thermal contraction of hot water, we found the velocity, cooling rate and heat transfer calculations to be consistent.

Acknowledgments

We are grateful to Mitchell Weigand of The Ohio State Univerisity for calling this subject to our attention.

References

Amador, G. J., Tabak, A. F., Ren, Z., Alapan, Y., Yasa, O., & Sitti, M. (2018). Thermocapillary-driven fluid flow within microchannels. *ArXiv Preprint ArXiv:1802.00475*.

Mondal, S., Phukan, M., & Ghatak, A. (2015). Estimation of solid–liquid interfacial tension using curved surface of a soft solid. *Proceedings of the National Academy of Sciences*, *112*(41), 12563–12568.

Song, D., Song, B., Hu, H., Du, X., Du, P., Choi, C.-H., & Rothstein, J. P. (2018). Effect of a surface tension gradient on the slip flow along a superhydrophobic air-water interface. *Physical Review Fluids*, *3*(3), 33303.

APPENDIX B – Velocimeter Operation

The operation of the velocimeter is user-friendly and straightforward. For best output results, the following precautionary measures need to be considered while operating the instrument.

- **Underflow:** At least two reasons exist for the high percent underflow - a condition occurring when a mathematical operation results in a mobility number that is too small to store in the device but is recorded, counted and displayed at the minimum value on a histogram. Firstly, with the lower bead concentration, there will be a high percentage of signals from non-beads (debris). Secondly, as the cell gets accumulated with removable dirt, the absolute number of underflow signals increases. Achieving a minimum percentage of underflow reflects the better quality of the data unless the sample is a known mixture of magnetic and non-magnetic objects.
- **Changing samples:** When making major switches of the sample perform a blank run with water only, checking the magnetophoretic mobility histogram to determine whether magnetic particles are still present in the channel cell system.
- **Downstream bubbles:** Downstream bubbles and vapor gaps could be due to a leak. Make sure the outlet tubing is fully wetted when starting each measurement. Otherwise, you may get anomalously long tracks due to pressure-driven flow.
- **External vibrations:** During image acquisition of the tracks vibrations near the instrument should be minimized. The presence of external vibrations moves the particles in a zigzag manner resulting in anomalous tracks and results.
- **Cleaning channel cell:** The following procedure was employed to clean the channel cell which removed the debris to some extent. Fill a syringe with a 1% cleaning solution (Ex:

Microclean) load some of this into the cell, allow to sit overnight, then flush the cell with at least 5 mL distilled water followed by 5 mL of 70% ethanol or 91% isopropanol, then flush with 5 mL distilled water. If the outside of the cell is dirty, try to clean it as follows. Twist a sheet of microscope lens paper to form a stick; soak this stick in alcohol; use the stick to wipe the outer surfaces of the cell without applying finger pressure (pressure on the paper could scratch the glass).

- **Buffer and waste chamber:** The buffer solution chamber needs to be filled and cleaned, checking to make sure no dirt particles accumulated, and the connected tubes are immersed completely in the liquid to avoid air bubble formation. The waste liquid collection chamber needs to be emptied without creating a disturbance to the vacuum pump to generate a required vacuum which facilitates the flow from the sample chamber and buffer chamber. The liquid trap (filter) connected between the waste chamber and vacuum pump should be cleaned/ or replaced regularly as some waste that accumulates in the filter blocks the pump and disturbs the generation of vacuum.
- **Sample channel cell assembly/ replacement:** The sample channel cell needs to be replaced if there is evidence of excessive debris accumulation. The area with the debris is excluded from particle tracking by the software and only a few particles will be tracked. Make sure to assemble the clean channel cell and run a sample of calibration beads to get appropriate mobility results before conducting other experiments.